Spring 1-1-2019

Complex Dynamics of High Frequency Atmospheric Gravity Wave and Fine Structure Interactions

Tyler S. Mixa
University of Colorado at Boulder, tyler.mixa@gmail.com

Complex Dynamics of High Frequency Atmospheric Gravity Wave and Fine Structure Interactions

by

T. S. Mixa

B.A., Carleton College, 2012

M.S., University of Colorado at Boulder, 2014

A thesis submitted to the

Faculty of the Graduate School of the

University of Colorado in partial fulfillment

of the requirements for the degree of

Doctor of Philosophy

Department of Aerospace Engineering Sciences

2018

This thesis entitled:
Complex Dynamics of High Frequency Atmospheric Gravity Wave and Fine Structure Interactions
written by T. S. Mixa
has been approved for the Department of Aerospace Engineering Sciences

_____

Prof. Lakshmi Kantha

_____

Dr. David Fritts

Date _____

The final copy of this thesis has been examined by the signatories, and we find that both the content and the form meet acceptable presentation standards of scholarly work in the above mentioned discipline.

Mixa, T. S. (Ph.D., Aerospace Engineering)

Complex Dynamics of High Frequency Atmospheric Gravity Wave and Fine Structure Interactions

Thesis directed by Prof. Lakshmi Kantha and Dr. David Fritts

Gravity waves are a dominant source of energy transport and coupling throughout the atmosphere. Transient gravity wave propagation effects and locally induced dissipation make significant contributions to the variability of temperature and wind evolutions over a broad range of spatial and temporal scales. Gravity wave impacts are particularly important to the mesosphere and lower thermosphere, where high wave amplitudes promote a range of complex, nonlinear interactions with the background environment at scales that are difficult to model and observe. An improved understanding of small-scale, temporally and spatially intermittent gravity wave interactions with variable local and large-scale environments is essential to improving how gravity wave dynamics are parameterized in mesoscale and global scale models.

This dissertation presents a comprehensive overview and analysis of the complex dynamics of high frequency atmospheric gravity wave and fine structure interactions in the mesosphere and lower thermosphere. Simulation studies are carried out to identify the fundamental dynamics of gravity wave-fine structure interactions in an idealized environment, evaluate the behavior of transient gravity wave propagation in an evolving background where linear assumptions break down, and determine the limitations of modeling gravity wave-fine structure interactions with the constraints of current mesoscale models. These studies utilize high resolution numerical simulations and improve the current understanding of gravity wave dynamics and their impact on the atmosphere.

Findings in these studies indicate that gravity wave-fine structure interactions have predictable dynamics that can be traced to the underlying vorticity characteristics set by

the background environment. Gravity wave interactions with fine-structure background variations below gravity wave scales determine the formation of instability and induced wind characteristics, while gravity wave interactions with time evolving fine-structure variations larger than gravity wave scales account for intermittent forcing characteristics observed in the mesosphere and lower thermosphere. The dominant gradient characteristics of these interactions break down with insufficient spatial resolution, and the time dependent characteristics break down when under-resolved models apply viscous damping to constrain small scale motions. With proper consideration of the expected dynamics in a given environment, one can estimate the extent to which gravity wave-fine structure interactions contribute to the variability in under-resolved model simulations, identifying environments for which improved characterization would be beneficial.

Acknowledgements

I gratefully acknowledge the support of my two advisors, Professor Lakshmi Kantha and Dr. David Fritts. Without you, this dissertation would not have been possible. Your incredible guidance and unlimited patience have helped me to develop as a scientist and lay the foundations for a career with my head in the clouds. You've given me the opportunity to pursue fieldwork and research collaborations on four continents and to present my research in just as many, opening up a world of opportunity. You have my deepest gratitude.

I wish to thank my colleagues at GATS, especially Katrina Bossert and the late Brian Laughman, for your tireless guidance on how to survive in the world of academic research and for the warm environment you created. To Katrina Bossert and Abhiram Doddi, your friendship helped me survive our isolated months abroad in the Japanese mountains, the Utah desert, and the NZ suburbs, and your prodding kept me from falling asleep in front of my terminal on many a night flight. To my colleagues at DLR, Utah State University, Kyoto University, Yale University, and NCAR, thank you for providing a sense of home away from home and for tolerating my occasional piano playing. To Tom Lund, thank you for sitting through many lengthy discussions of the anelastic code architecture and my simulation results; you provided a needed sanity check to keep my research grounded in reality. My thanks also goes out to Dale Lawrence for teaching me how to survive in the field, build makeshift slingshots, and rescue UAVs from treetops and flooded rice fields with reckless abandon.

To my dear friends who have made this journey a destination, I never could have gotten this far without you. Jordan Holquist, Jake Mashburn, Ann Dietrich, Trey Laurence,

and Collin Bezrouk, it has been a privilege to soar through this adventure with you from the beginning. To my valued orchestra companions, Trubee Davison, Noah Williams, Maya Fabrikant, Monica Carroll, Betsy Noecker, Jen Kiskin, and Kyle Shaw, we've made so much more than music together - every note truly was emotion. To my Japanese classmates Saya Karkare and Emma Ainge, our bonds transcend words - 頑張りましょう!!! To the inimitable Valeria Serrano and Bryan Costanza, I cannot imagine where I would be without our time together.

And finally, to my ever-loving parents, Marlene and Scott Mixa. Your unwavering support has meant more than you will ever know. This is entirely your fault.

Thank you all for keeping me interesting.

Contents

Chapter

1 Introduction: Gravity Wave-Fine Structure (GW-FS) Interactions **1**

1.1 Research Synopsis 3

1.2 Chapter Organization 8

2 Gravity Waves in the Atmosphere **10**

2.1 Gravity Wave Propagation Dynamics 10

2.2 Complexities Enabled by Nonlinear Interactions 13

2.3 Gravity Wave Breaking and Instability Evolution 17

2.3.1 Characteristic Instability Structures 20

2.4 Summary 24

3 Motivations for This Study **25**

3.1 Wave Evolution Complexities Caused by Environmental Influences 25

3.2 Influence on Large Scale Atmospheric Dynamics 25

3.3 Limitations in Observable Dynamics 27

3.4 Unresolved Dynamics Driving Observable Mesoscale Phenomena 27

3.5 Known Deficiencies of Global and Mesoscale Models in the Mesosphere and Lower Thermosphere (MLT) 28

3.5.1 Resolution Restrictions 28

3.5.2 Wave Parameterization Problems 29

3.6 Summary 31

4 Observational Techniques for Studying the MLT **32**

4.1 Airglow-based Observations 32

4.1.1 Sodium Lidar 32

4.1.2 AMTM and ANI 34

4.2 Mesospheric Cloud Imagers 35

4.2.1 Ground-based Photography 35

4.2.2 Satellite Imagers 36

4.3 Summary 37

5 Gravity Wave-Fine Structure (GW-FS) Studies to Date **38**

5.1 Idealized Modeling of Gravity Wave Interactions in MLT-like Environments . 38

5.2 Observational Studies of Gravity Wave-induced Instabilities in the MLT . . . 40

5.3 Summary 44

6 Numerical Model Simulation Architecture Employed in This Research **46**

6.1 Finite Volume Anelastic Code-Equations 46

6.2 Code Capabilities 48

6.3 Background Profile Generation for FS Studies 49

6.4 Parameter Definitions 50

6.5 Vertical Mesh Configurations 51

6.6 Initial Testing and Validation 52

6.7 Summary 53

7 Gravity Wave Propagation through Isolated Fine Structures in the MLT **54**

7.1 Parameter Definitions 55

7.2 Case 1: Nonlinear GW Propagation through a Uniform Background 57

7.3 Cases 2 to 6: Nonlinear GW Propagation through Shear and Stability 60

7.3.1 Cases 2 to 4: Initial Instability Evolution 60
7.3.2 Cases 5 and 6: Initial Instability Evolution 65
7.3.3 Turbulence Evolution and Large-Scale Influences 70
7.4 Expanding on Previous Findings 77
7.5 Summary 79

8 Gravity Wave Propagation through an Evolving Inertial Wave in the MLT 81
8.1 Event Characteristics Determined from Observations 82
8.1.1 AMTM 83
8.1.2 Lidar 84
8.2 Event Characteristics Determined From Simulations 89
8.2.1 Methodology 90
8.2.2 Event Overview 91
8.2.3 19 to 20 UT: Filtering 94
8.2.4 21 UT: Propagation 94
8.2.5 22 to 23 UT: Instabilities 96
8.2.6 24 to 25 UT: Propagation 98
8.3 Summary 99

9 Gravity Wave-Fine Structure (GW-FS) Interactions Modeled with Resolution Constraints 102
9.1 Parameter Definitions 103
9.2 Cases 1 to 5: Instability Evolution and Vortical Deterioration 105
9.3 Parameter Amplitude Retention 108
9.3.1 GW-Determined Parameter Amplitudes 109
9.3.2 Gradient-Determined Parameter Amplitudes 109
9.4 Induced Wind and Resolution Relationships 111
9.5 Summary 114

10 Conclusions and Future Work **118**

10.1 Research Study 1 118

10.2 Research Study 2 120

10.3 Research Study 3 122

10.4 Suggestions for Future Work 123

10.4.1 Research Focus 1 Additional Studies 123

10.4.2 Research Focus 2 Additional Studies 124

10.4.3 Research Focus 3 Additional Studies 124

10.4.4 GW-FS Interactions in the Lower Atmosphere 125

10.5 Summary 126

Bibliography **127**

Terms and Abbreviations **137**

Symbols and Notation **139**

Appendix

A Chapter 8 Supporting Study **141**

A.1 Wave Amplitude Influences on GW and Background Flow Evolution 141

Tables

Table

7.1 Study 1 Simulation Parameters 55

9.1 Study 3 Simulation Parameters 104

Figures

Figure

2.1 Forces in Stratified Fluids 10
2.2 Oragraphic GW 11
2.3 Linear GW Dispersion Relation Limits 13
2.4 Modulationally Unstable Wave Packet 17
2.5 Self-Accelerated Wave Packet 18
2.6 MLT Wave Breaking in PMC Images 18
2.7 KHI Vortical Structure 19
2.8 Gravity Wave Baroclinic Source Generation 21
2.9 Vortex Rings in Gravity Wave Breaking 21
2.10 Sheet and Layer Structures 22
2.11 KHI vs. Re & Ri 23

3.1 Gravity Wave-Mean Wind Interaction 26

4.1 Na Lidar Wind and Temperature Measurements 33
4.2 Gravity Wave Lidar Measurement 34
4.3 Gravity Wave AMTM Measurement 35
4.4 Ground-based PMC Image Schematic 36
4.5 PMC Ice Ring Evolution from CIPS 37

5.1 Simulating PMC Observations Beyond Resolution Limits 42

5.2 Vortex Source Identification in Multiscale Environment 43
5.3 Reproducing PMC Vortex Evolution with DNS 44

6.1 Power-Law Stretched Vertical Grid 51
6.2 Study 3 Vertical Grid 52
6.3 Wave-Induced KHI Train in FV Simulation 53

7.1 Background Shear and Stability Profiles 56
7.2 Case 1 u' and w' Fields 58
7.3 Case 1 Fluxes 58
7.4 Case 1 $\Delta\overline{U}$ Evolution 59
7.5 Cases 1 to 4 ζ_y Evolution 61
7.6 Cases 1 to 4 $\frac{1}{\rho^2}\left(\nabla\rho\times\nabla P\right)_y$ Evolution 62
7.7 Case 2 Initial Instability Evolution 64
7.8 Case 3 Initial Instability Evolution 65
7.9 Case 4 Initial Instability Evolution 66
7.10 Case 2 Initial Instability ζ_x and ζ_y Slices 67
7.11 Case 3 Initial Instability ζ_x and ζ_y Slices 68
7.12 Case 4 Initial Instability ζ_x and ζ_y Slices 68
7.13 Case 5 and Case 6 ζ_y Evolution 69
7.14 Case 5 and Case 6 $\frac{1}{\rho^2}\left(\nabla\rho\times\nabla P\right)_y$ Evolution 69
7.15 Case 5 Initial Instability Evolution 70
7.16 Case 6 Initial Instability Evolution 71
7.17 Case 5 Initial Instability ζ_x and ζ_y Slices 72
7.18 Case 6 Initial Instability ζ_x and ζ_y Slices 72
7.19 Cases 2 to 6 ζ_y and $\Delta\overline{U}$ Profile Evolution 73
7.20 PSD of u' Horizontal Wavenumber Spectra 74
7.21 $\Delta\overline{U}/\overline{U}_0$ Evolutions for Cases 1 to 6 76

8.1 AMTM Event Overview 83
8.2 GW Parameters from AMTM 84
8.3 Lidar Wind and Temperature Profiles 85
8.4 Lidar Temperatures at Low and High Frequencies 86
8.5 ω and N Event Profiles 87
8.6 Lidar Temperature Field for HFGW 88
8.7 Ri from Lidar 89
8.8 ω and N Profiles at 22 UT and 23 UT 90
8.9 Simulated $\theta'/\overline{\theta}$ Fields for $\omega_0 = 0.008s^{-1}$ 92
8.10 Simulated $\theta'/\overline{\theta}$ Fields for $\omega_0 = 0.016s^{-1}$ 93
8.11 Simulated $\theta'/\overline{\theta}$ Fields for all ω_0 at 21 UT 93
8.12 Simulations and Observations at 19 UT 94
8.13 Simulations and Observations at 20 UT 95
8.14 Simulations and Observations at 21 UT 96
8.15 GW Momentum Flux for Low and High ω_0 96
8.16 Simulations and Observations at 22 UT 97
8.17 Simulations and Observations at 23 UT 98
8.18 Simulations and Observations at 24 UT 99
8.19 Simulations and Observations at 25 UT 100

9.1 ζ_y Early Instability Evolution for Cases 1 to 5 106
9.2 $\frac{1}{\rho^2}\left(\nabla\rho \times \nabla P\right)_y$ Early Instability Evolution for Cases 1 to 5 106
9.3 ζ_y Instability Evolution for Cases 1 to 5 at 1 Minute Increments 108
9.4 u' and w' Amplitude Evolution 110
9.5 $\frac{1}{2}\left(u'^2 + w'^2\right)$ and $u'w'$ Amplitude Evolution 110
9.6 ζ_y and $\frac{1}{\rho^2}\left(\nabla\rho \times \nabla P\right)_y$ Amplitude Evolution 112
9.7 $\overline{U}_z$ and N^2 Amplitude Evolution 112

9.8 $\Delta\overline{U}_z$ Amplitude Evolution 113
9.9 $\Delta\overline{U}_z$ at $T = 10T_B$ 114
9.10 Amplitude Retention vs. Resolution Ratio ($\Delta x/\eta$) for Cases 2, 4, and 6 . . . 115
9.11 Amplitude Retention vs. Resolution Ratio ($\Delta x/\eta$) for Cases 3, 5, and 7 . . . 115

A.1 u' Centerline Profiles vs. Amplitude 142
A.2 $u'w'$ Centerline Profiles vs. Amplitude 142
A.3 $\overline{U}$ vs. Amplitude 143
A.4 $\Delta\overline{U}$ at $T = 10T_B$ 144
A.5 Domain-Averaged KE vs. Amplitude 144
A.6 KE % Above and Below FS vs. Amplitude 145

Chapter 1

Introduction: Gravity Wave-Fine Structure (GW-FS) Interactions

Gravity wave (hereafter GW) propagation through stratified shear environments is a subject of renewed interest in the atmospheric science community. The ubiquity of layered structures in the atmosphere (e.g., Sato and Woodman, 1982; Woodman and Rastogi, 1984; Reid, 1990) has triggered a call to probe the behavior of GW propagation in these environments, particularly in the Mesosphere and Lower Thermosphere (hereafter MLT), where GW amplitudes become large enough to influence the background flow (Tsuda, 2014) and turbulence dynamics can be observed with ground-based instruments. The complex interplay of GW-induced and shear-induced layering dynamics (see e.g., Fritts and Alexander, 2003), coupled with the high degree of non-linearity attainable in these environments (Lund and Fritts, 2012), necessitates the use of modeling to contextualize our understanding of GW propagation through stratified environments beyond the limitations of existing measurement capabilities.

GWs are responsible for a significant amount of the momentum and energy transport that occurs in the atmosphere. In the MLT, GWs drive both large scale interactions, including the reversal of the polar mesospheric jet and planetary wave modulation, and small scale interactions, where the dominant GW influences are nonlinear and cannot be characterized by linear theory or linear models. When passing through regions of elevated stratification and/or shear, GWs excite and modulate the evolution of small scale instabilities that drastically change the layer structure in these regions. Such layers in turn alter GW propagation in

numerous ways, including but not limited to: filtering the outgoing GW spectra, promoting ducting or reflection, hastening the onset of self-acceleration (SA) dynamics, and encouraging the exchange of heat, energy, and momentum via turbulent transport and mixing mechanisms. These small-scale dynamics directly influence the behavior of the atmosphere at larger scales, necessitating the ability to quantify gravity wave-fine structure (GW-FS) interactions over the full range of active spatial scales to understand the induced mesoscale dynamics.

High-frequency GWs produce a significant portion of the energy exchange in the MLT, yet prevailing global models cannot resolve dynamics on the spatial scales of high frequency waves or fine layered structures known to be present throughout the atmosphere. A lack of consensus on how to parameterize the large scale impacts of GW-FS interactions has led to significant discrepancies in model predictions of the MLT, limiting the accuracy of medium range forecasting and severe weather prediction (Pedatella et al., 2014; Liu, 2016, and citations therein). A better understanding of small-scale, temporally and spatially intermittent GW interactions with variable local and large-scale environments is critical to improving GW parameterizations in the next generation of mesoscale and global scale models, providing significant improvements to long-term weather, climate, and circulation models which address critical societal needs. High-resolution simulations using state-of-the-art models appear to be the most beneficial path to this end.

The principal objective of this research is to **investigate high frequency atmospheric gravity wave and fine structure interactions**. Here *high-frequency* refers to GWs with an intrinsic frequency ω much closer to the Brunt-Vaisala frequency (N), the frequency of buoyant oscillations in the atmosphere, than to the inertial frequency (f), determined by the Earth's rotation. Due to the need for an improved understanding of GW dynamics in the MLT, the unique ability of ground-based instruments to resolve spatial scales of interest to turbulence at these altitudes, and the computational benefits of the low Reynolds Number (Re), this research targets GW-FS interactions at MLT altitudes. The

dynamics characterized in the MLT can be generalized to represent GW-FS interactions in the entirety of the atmosphere with the inclusion of the appropriate altitude-localized dynamics (ex. the convective boundary layer) and suitable changes to the local Re, Richardson number (Ri), and state variables.

1.1 Research Synopsis: Guiding Research Question and Science Foci

The research herein seeks to answer the overarching question: **How does fine structure influence high-frequency gravity wave propagation and transport of energy and momentum?** To answer this question, several principal research foci have been identified:

(1) **How do isolated shear and stability fine structures influence high-frequency gravity wave propagation in the MLT?**

(2) **How do complex stratification environments influence high-frequency gravity wave coherence and fluxes of momentum and heat in the MLT?**

(3) **What are the impacts of GW-FS interaction mechanisms for transport and diffusion?**

These objectives are described in detail in the remainder of the text, including their motivation, methodologies, and outcomes.

GW influences and interactions in the atmosphere take many forms. GW superpositions at small amplitudes lead to systematic wave-wave interactions, spectral energy transfers, and altered GW propagation and transmission (e.g., Yeh and Liu, 1981; Klostermeyer, 1991; Vanneste, 1995; Sonmor and Klaassen, 1997; Heale and Snively, 2015). At larger amplitudes, GWs exhibit local instabilities having shear and/or buoyancy energy sources, (e.g., Kelvin-Helmholtz instabilities (KHI) and GW breaking) (e.g., Andreassen et al., 1998; Lelong and Dunkerton, 1998a,b; Fritts et al., 1998, 2009b,c). GW-mean flow interactions also enable modulational instabilities and SA dynamics leading to GW deformations and secondary GW generation (e.g., Grimshaw, 1977; Sutherland, 2001, 2006; Dosser and Sutherland, 2011a; Fritts et al., 2015). More recent studies further demonstrate the importance of accounting for small GW scales (Watanabe et al., 2015; Ngan and Eperon, 2012; Siskind, 2014; Koshyk et al., 1999; Sato et al., 1999), local instability dynamics (Fritts et al., 2014a,c; Hecht et al., 2014; Werne, 2016), and sheet and layer structures comprising enhanced shears and stability at small vertical scales that occur throughout the atmosphere (e.g., Sato and Woodman, 1982; Woodman and Rastogi, 1984; Reid, 1990, and others). Recent radar, lidar, and ground-based imager studies demonstrate GW's critical role in the evolution of sheet and layer structures in the MLT (Lehmacher et al., 2007; Baumgarten and Fritts, 2014; Bossert et al., 2016; Fritts et al., 2017; Hecht et al., 2018), identifying persistent layers less than 0.5 km deep that show signs of propagating GWs, trapped GWs, and breaking GWs which give rise to instabilities and secondary GW generation.

The first study presented in this dissertation, titled **Numerical Simulations of High Frequency Gravity Wave Propagation through Isolated Fine Structures in the Mesosphere and Lower Thermosphere**, addresses Principle Research Focus 1, establishing a basic understanding of the impacts of individual FS attributes in an idealized, isolated layer with otherwise uniform stratification. An anelastic numerical model is used to study the influences of FS in the wind and stability profiles on GW propagation in the MLT. Large amplitude GWs interacting with thin regions of wind shear and/or potential temperature

gradients are found to evolve very differently, depending on the precise source and sink terms for small-scale motions. The resulting small-scale dynamics promote local instabilities, dissipation, and momentum deposition at different altitudes and lower GW amplitudes than would occur in the absence of FS layering. Given the significant amplitudes and ubiquitous occurrence of FS throughout the atmosphere, the importance and diversity of these flow evolutions suggest that such influences have broad implications. One major implication is significantly altered GW momentum transport and deposition relative to environments having no FS layers. The results of this study are found in Chapter 7.

With a basic understanding of how individual layer parameters can affect the evolution of the background environment and a GW propagating through the layer, it is imperative to understand how these effects are compounded in the true conditions of the atmosphere, featuring numerous layers of various depths and amplitudes rather than a single structure. Multiscale GW interactions occur frequently in the upper atmosphere, where high frequency gravity waves (HFGWs) with short periods/wavelengths and high momentum flux pass through larger inertial gravity waves (IGWs) that vary on much slower timescales. Such multiscale wave environments undergo a range of complex, nonlinear interactions which have been observed in numerous studies, including the recent DEEPWAVE campaign observations in Fritts et al. (2015), and Bossert et al. (2015). Large scale models often oversimplify such interactions by approximating the background as a steady state, spatially periodic horizontal wind field, or in more extreme cases, neglecting nonlinear dynamics or ignoring the small-scale interactions entirely. More guidance is needed on the behavior of small scale GW interactions with variable local and large-scale environments in order to improve parameterizations of transient GW dynamics in mesoscale models.

Ground-based instruments have enabled a broad understanding of the large-scale dynamics occurring in the MLT. Lidar-based observational studies have long been used for climatologies of regional GW dynamics (Chanin and Hauchecorne, 1981), using GW potential energy density and GW amplitude to determine wave attenuation in a given altitude

range (see e.g., Tsuda et al., 2000). Seasonal variations in wave attenuation, as well as variations in measurements between adjacent research stations, can be used to identify likely sources of heightened GW activity and regions of critical level filtering (e.g., Chen et al., 2013; Yamashita et al., 2009; Kaifler et al., 2015; Whiteway et al., 1997). Critical levels for orographic GWs can also be identified by wind directions rotated more than 90 degrees from ground level forcing (Yamashita et al., 2009). The phase slope of a GW is often used to identify stationary (orographic), upward, and downward propagating GWs. However, without knowing both the local background wind and horizontal wavenumber, the GW intrinsic frequency and propagation direction are easily misdiagnosed from the ground (Fritts and Chou, 1987; Dörnbrack et al., 2017).

Recent advances in Rayleigh lidar measurement techniques provide guidance on the types of MLT dynamics that are poorly understood, enabling characterization of fine vertical layered structures over a 10-20 km vertical extent at MLT altitudes. Sodium density measurements from Bossert et al. (2016) indicate the near-ubiquitous presence of finely-layered structures when the lidar samples at a high cadence with increased fidelity. The observations are notable in that 1) temperature and density layers less than 0.5 km deep are observed continuously by stations in Utah and Norway, with individual layer structures having durations over 1 hour; 2) density layers are accompanied by sharp temperature and wind gradients, producing significant stability enhancements over twice the background value and critical Ri sufficient to produce overturning; and 3) oscillations in the fine layered structures indicate significant GW influences, showing signs of transient aberrations that depart from the systemic impacts of GW dynamics documented in previous observations.

Multi-instrument studies incorporating lidar data have further explored dynamics of GW breaking and ducting (Bossert et al., 2014; Smith et al., 2005). The inclusion of numerical simulations supplementing the use of multiple, coordinated instruments adds further utility by assessing the behavior of environmental characteristics that are outside the observable domain and/or at scales below what ground-based instruments can resolve (Cao et al.,

2016; Hecht et al., 2014, 2018; Heale et al., 2017). To diagnose complicated GW events, simulation studies are needed in conjunction with multi-instrument observations to more comprehensively describe the underlying dynamics and ultimately characterize the evolution of a 3D volume with time.

The second study presented in this dissertation, titled **High Frequency Gravity Wave Propagation through an Evolving Inertial Wave in the MLT**, addresses Principle Research Focus 2 by probing the dynamics of transient GW-FS interactions in the MLT, expanding on the findings of idealized studies with guidance from observational data. A case study is carried out on a set of ground-based observations collected on 21 January 2015, in which a sodium resonance lidar and advanced mesospheric temperature mapper (AMTM) observed intermittent propagation of a HFGW through an IGW over the Arctic Lidar Observatory for Middle Atmosphere Research (ALOMAR) in Norway. The evolving IGW promotes critical layers, reflection, evanescence, and tunneling as the HFGW propagates through alternating IGW phases. A series of simulations using the high resolution anelastic numerical model characterize the HFGW propagating through the IGW and account for the temporal variability in the observational data. The study diagnoses the dynamics contributing to observational discrepancies, and it provides a broader understanding of the types of transient dynamics driving mesoscale transport phenomena which are not addressed in current mesoscale models. The results of this study are found in Chapter 8.

The large domains of mesoscale weather models necessitate the use of reduced grid resolution relative to fine scale studies such as those described in Studies 1 and 2. GW parameterizations imposed by under-resolved models are known to reduce the accuracy of predicted wind and temperature fields at large scales (Pedatella et al., 2014). Numerous MLT studies have shown the capacity for considerable improvement when resolution is increased to $\mathcal{O}(10\ km)$ or better (Liu, 2016, and citations therein), but even the most well-resolved mesoscale models top out at a resolution limit of $\mathcal{O}(1\ km)$ often in a small nested region of a given simulation. While these studies emphasize qualitative improvements, no study to date

quantifies the accuracy of GW energy characteristics as a function of the imposed resolved scale limits relative to the expected energy-containing scales in a given environment. Having the unique capacity to run fully resolved simulations of GW-FS interactions in the MLT, one can establish a set of metrics to approximate how well an under-resolved simulation characterizes the true, large-scale dynamics at play. Understanding this tradeoff can provide a metric for the accuracy of GW characterization anywhere in the atmosphere and have broad applicability to the larger atmospheric community.

The third and final study presented in this dissertation, titled **Evaluating the Accuracy of Gravity Wave Simulations in the Mesosphere and Lower Thermosphere with Artificially-Constrained Resolution**, addresses Principle Research Focus 3, examining large scale transport consequences of under-resolved GW-FS interactions when characterized in the manner used by predominant mesoscale models. Using a simulation case from Chapter 7 as a baseline for comparison, the same environment is simulated with the maximum grid resolutions of 15 m, 45 m, 200 m, and 2 km grid spacing. This study follows the example of Bölöni et al. (2016) by identifying the parameters affected by reduced fidelity. The project ultimately evaluates the selectivity with which different fields lose accuracy, both in terms of decreasing resolution and Re, in order to determine the needed resolution for a given environment that provides confidence in the dynamics that project up to large scales and to enable comparisons to other datasets without loss of generality.

1.2 Chapter Organization

Chapter 2 provides a basic overview of GW propagation dynamics, including recent progress in the understanding of nonlinear interactions driving instability development and energy exchange, and a basic morphology of the evolution of GW breaking. Chapter 3 describes the recent advances in observation and modeling of GW instability dynamics in the MLT, emphasizing the limitations of our current understanding of GW-FS interactions in the MLT and motivating the research objectives of this thesis. An overview of current MLT

observation techniques is presented in Chapter 4, and highlights from recent GW-FS studies are presented in Chapter 5. Chapter 6 presents the simulation architecture used for the studies herein, highlighting the capabilities of the code and describing the initial validation studies. The outcomes of Research Studies 1, 2, and 3 are then presented in Chapters 7, 8, and 9, respectively, with conclusions and final remarks, including recommendations for future work, presented in Chapter 10.

Chapter 2

Gravity Waves in the Atmosphere

2.1 Gravity Wave Propagation Dynamics

GWs occur in a stratified fluid when a parcel is raised or lowered from its equilibrium level by external interactions (e.g., convective plumes, large storm cells, airflow over mountains, turbulent updrafts, etc.). The restoring force of buoyancy causes the parcel to oscillate about its equilibrium level (see Figure 2.1). A sample figure of an orographic GW generated by airflow over a mountain is shown in Figure 2.2.

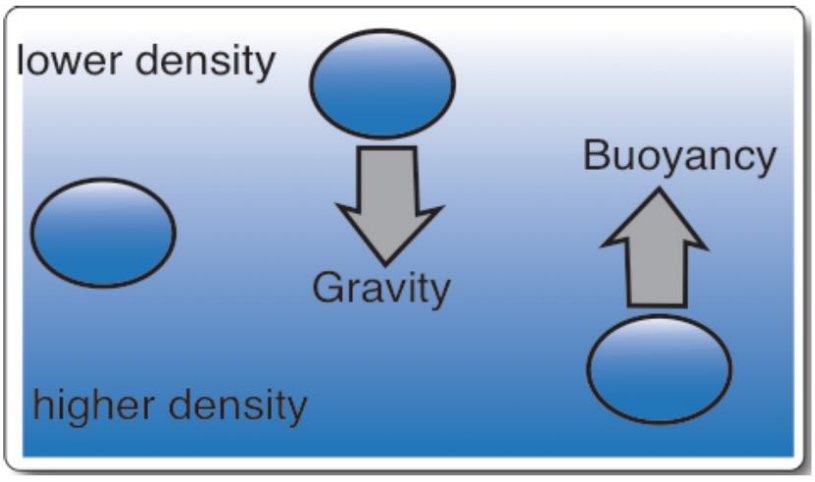

Figure 2.1: Simple schematic of the dominant forces on stratified fluids, taken from *Heale (2014)*.

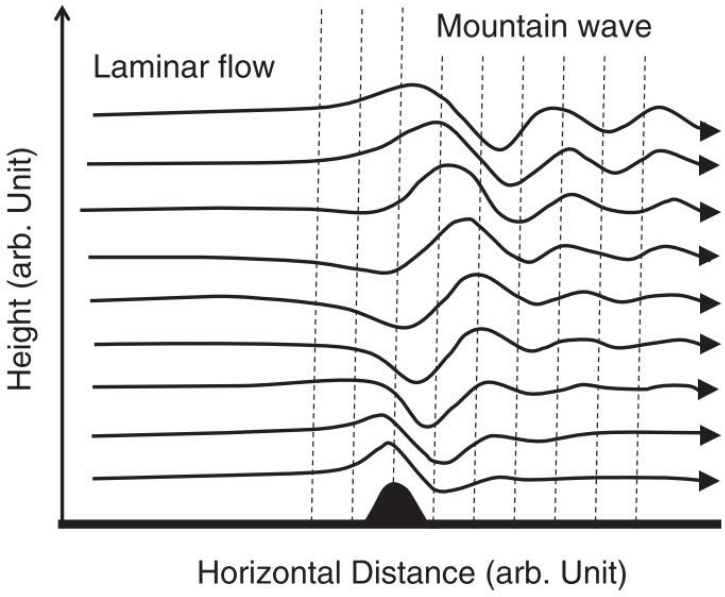

Figure 2.2: Orographic GW generation by airflow over topography. Taken from *Tsuda (2014)*.

The GW intrinsic frequency, given by

$$\omega = k(c - U) \quad , \tag{2.1}$$

is the GW frequency measured relative to the mean horizontal windspeed U, where k is the horizontal wavenumber and c is the observed horizontal phase speed, the speed of horizontal motion of a point of constant GW phase measured by a stationary observer on the ground. The intrinsic frequency (ω) varies with the background U, but the ground-relative GW frequency, $\omega_o = kc$, remains constant in linear propagation.

Vertical GW propagation occurs when ω is between the inertial frequency,

$$f = 2\Omega Sin\ \phi \tag{2.2}$$

where Ω is the earth's rotation rate and ϕ is the latitude, and the buoyancy frequency,

$$N = \sqrt{\frac{g}{\theta}\frac{\partial\theta}{\partial z}} \tag{2.3}$$

where θ is the potential temperature and g is the gravitational acceleration. The angle

between lines of constant GW phase and the vertical axis is given by

$$Cos[\Phi] = \frac{\omega}{N} \tag{2.4}$$

such that the GW perturbations become vertical buoyant oscillations in the limiting condition $\omega \to N$.

A GW's frequency is related to its horizontal and vertical wavenumbers, k and m, by the linear dispersion relation, given here in 2D anelastic form (see e.g., Fritts and Alexander, 2003; Nappo, 2012):

$$m^2 = \frac{k^2(N^2 - \omega^2)}{\omega^2 - f^2} - \frac{1}{4H^2} \tag{2.5}$$

where H is the scale height, the height over which density decreases by a factor of $1/e$. The linear dispersion relation can be expressed in many forms depending on the type of GW and the constraints of a given environment. For HFGWs ($\omega \gg f$ and $m^2 \gg \frac{1}{4H^2}$), Equation 2.5 simplifies to

$$m^2 = k^2 \left(\frac{N^2}{\omega^2} - 1 \right) \tag{2.6}$$

and can be equivalently expressed as

$$m^2 = k^2 \left(\frac{N^2}{k^2 \left(c - U \right)^2} - 1 \right) \tag{2.7}$$

by substituting from Equation 2.1.

As GWs propagate linearly, vertical gradients of U and N produce corresponding changes to ω and m while k and c (and hence, ω_o) remain constant. Equation 2.5 predicts that GW vertical propagation breaks down when the vertical wavenumber (m) goes to infinity or becomes imaginary (i.e., when ω approaches its propagation bounds of f or N). The conditions causing $m \to \infty$ and $m^2 < 0$ are shown in Figure 2.3, with the corresponding phase structure indicated for GWs A through G in scenarios (i) and (ii). A turning layer (Figure 2.3i) occurs when $\omega \to N$ (Bretherton, 1969). For an approaching GW (A), the vertical phase speed is reversed as the GW fully reflects (C) at the turning layer. Within the layer where $\omega > N$, the GW is evanescent ($m^2 < 0$) and can only propagate horizontally,

having vertically-oriented phase lines (B) and amplitude that decreases exponentially with altitude. Turning layers occur in the atmosphere in regions of decreasing N and/or increasing U, and ducting occurs when a GW is trapped between two turning layers. A critical level (Figure 2.3ii) occurs when $U \rightarrow c$ and therefore $m \rightarrow \infty$ (Booker and Bretherton, 1967). For an approaching GW (F), the vertical phase speed goes to 0 and the GW (G) refracts to smaller scales and dissipates. True critical levels occur when $\omega \rightarrow f$, and they exist in the atmosphere in regions of decreasing U.

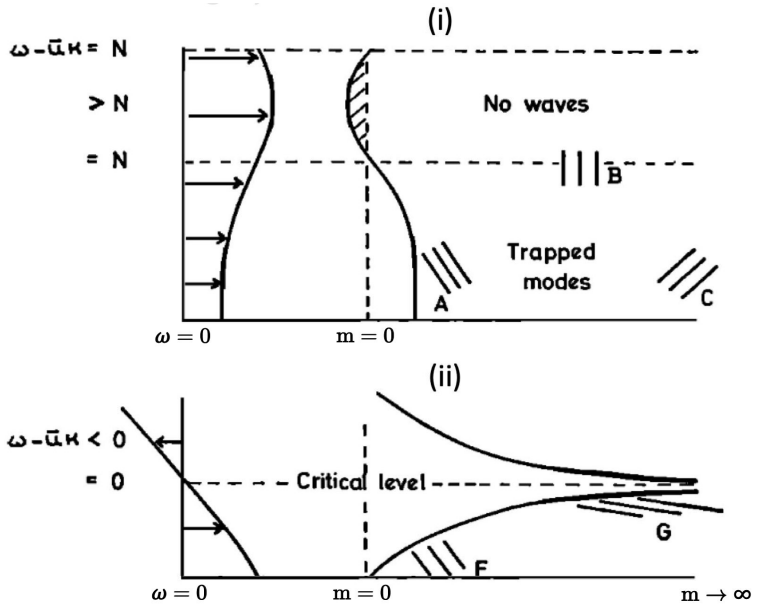

Figure 2.3: Linear GW propagation behavior predicted at (i) a turning layer and (ii) a critical level, two environments where the linear dispersion relation breaks down. The solid line vertical profiles in each plot show the intrinsic frequency ($\omega = \omega_{observed} - kU$, left) and the vertical wavenumber squared (m^2, right). Predicted GW responses are shown in the phase structures labeled A through G. At a turning level (i), $\omega > N$ and $m^2 < 0$ as N^2 decreases. Linear dynamics indicate full GW reflection at a turning layer (GWs labeled A and C). At a critical level (ii), $\omega \rightarrow 0$ and $m \rightarrow \infty$ as $c \rightarrow U$. Linear dynamics indicate full GW absorption at a critical level (GWs labeled F and G). Modified from *Bretherton (1969)*.

2.2 Complexities Enabled by Nonlinear Interactions

Linear or quasi-linear GW dynamics refer to interactions of small-amplitude GWs with the mean flow, and they form the basis of our understanding of the large scale GW behavior

and parameter relationships defined in the previous section. Nonlinear GW dynamics refer to GW interactions with temporally or spatially variable components of the flow. Nonlinearity introduces a high degree of complication into the propagation environment due to the multi-directionality of flow interactions. Whereas quasi-linear interactions are understood to be one-way, with the GW influencing the evolution of the mean flow, nonlinear interactions have been shown to significantly alter the character of the GW, producing changes in GW amplitude, modulating the GW frequency, and dictating the instability morphology as the flow evolves.

The fully nonlinear, non-Boussinesq equations for a two-dimensional internal GW in a non-rotating fluid are given by Dosser and Sutherland (2011a):

$$\overline{\rho}\frac{DU_{Tot}}{Dt} = -\nabla p - g\rho z \tag{2.8}$$

$$\nabla \cdot U_{Tot} = 0 \tag{2.9}$$

$$\frac{D\rho_{Tot}}{Dt} = 0 \tag{2.10}$$

where U_{tot} is the total velocity (u,v,w), ρ_{Tot} is the total density, p is the pressure, and the material derivative $D/Dt = \partial_t + u\partial_x + v\partial_y + w\partial_z$. These differ from the linearized conservation equations

$$\overline{\rho}\frac{\partial U_{Tot}}{\partial t} = -\nabla p - g\rho z \tag{2.11}$$

$$\nabla \cdot U_{Tot} = 0 \tag{2.12}$$

$$\frac{\partial \rho}{\partial t} = -w\frac{\partial \overline{\rho}}{\partial z} \tag{2.13}$$

by ignoring nonlinear advection terms and having the nonzero right hand side in the internal energy conservation equation. The Boussinesq form of these equations is given by replacing

$\overline{\rho}$ with ρ_0 in Equation 2.8.

While linear theory considers GW breaking to be the main mechanism of GW contributions to the mean flow, the background flow also has a nonlinear GW-induced component from the GW momentum flux being transported upward by the vertical group velocity (c_{gz}). Dosser and Sutherland (2011b) derive this expression,

$$\Delta\overline{U}_{induced} = \frac{\langle uw \rangle}{c_{gz}} = -\int \left[\frac{1}{\rho} \frac{\partial}{\partial z} \frac{\rho \langle uw \rangle}{\partial z} \right] dt \tag{2.14}$$

from wave action conservation (Boussinesq fluid) and momentum conservation (non-Boussinesq, nonlinear fluid), where $\langle\rangle$ indicates horizontal averaging.

Taking the curl of Equation 2.8 and using Equation 2.9, the coupled nonlinear equations for the total streamfunction and fluctuation density are

$$\frac{D}{Dt}\nabla^2\psi_{Tot} = -\frac{g}{\overline{\rho}}\frac{\partial \rho}{\partial x} - \frac{1}{\overline{\rho}}\frac{\partial \overline{\rho}}{\partial z}\frac{D}{Dt}\partial_z\psi_{Tot} \tag{2.15}$$

$$\frac{Dp}{Dt} = \frac{d\overline{\rho}}{dz}\frac{\partial \psi_{Tot}}{\partial x} \tag{2.16}$$

where the vertical displacement of the GWs is given by

$$\xi = -H\ ln\left[1 - \frac{\rho}{\bar{\rho}}\right] \approx H\ \frac{\rho}{\bar{\rho}} \quad when \quad \left|\frac{\rho}{\bar{\rho}}\right| << 1 \tag{2.17}$$

and the scale height H is

$$H = -\left(\frac{1}{\bar{\rho}}\frac{d\overline{\rho}}{dz}\right)^{-1} \quad . \tag{2.18}$$

The amplitude of the vertical GW perturbations, A_ξ, then takes the form of the weakly nonlinear Schrödinger equation

$$\partial_t A_\xi + c_{gz}\partial_z A_\xi = l\frac{1}{2}\omega_{mm}\partial_{zz}A_\xi + \frac{1}{6}\omega_{mmm}\partial_{zzz}A_\xi - lkUA_\xi + \frac{1}{2}\frac{\omega^2}{N^2k}\left(m + \frac{l}{H}\right)(\partial_z U)A_\xi \tag{2.19}$$

where t, z, and m subscripts indicate derivatives. The six terms in the Equation 2.19 represent

(1) Time evolution of A_ξ

(2) Advective derivative describing the translation of the GW packet (a group of GW wavelets spread over a narrow spectrum of frequencies) at the group velocity

(3) Leading order linear dispersion

(4) Linear dispersion of GWs moving close to the fastest vertical group velocity

(5) Nonlinear Doppler-shifting of the GWs by the wave-induced mean flow

(6) Nonlinear dispersion resulting from the shear associated with the wave-induced mean flow

From this equation, modulational instability is identified by the necessary condition

$$\omega_{mm}\omega^2 < 0 \quad \rightarrow \quad |m| < \sqrt{\frac{k^2 + \frac{1}{4H^2}}{2}} \quad . \tag{2.20}$$

The transition between modulational stability and instability occurs for GWs with fixed k moving at the fastest vertical group velocity. Modulational instabilities narrow the vertical depth of a GW packet, sharpening the amplitude and making its distribution asymmetrical (see Figure 2.4). Such nonlinear dynamics result in significant departures from the breaking altitudes predicted by linear theory, with lower breaking altitudes for non-hydrostatic GWs and higher breaking altitudes for hydrostatic GWs (Dosser and Sutherland (2011b)).

The Doppler-shifting of the GW c due to its own induced mean flow is known as self-acceleration (SA), a term coined by Fritts and Dunkerton (1984). SA is an *Re*-independent phenomenon that occurs when $u' \geq \overline{u}$ (Dosser and Sutherland (2011b)). Recent modeling studies by Fritts et al. (2015) demonstrate that SA effects result in highly-accelerated vertical phase speed (c_{gz}) at the top of the packet and significantly reduced c_{gz} as the bottom of the packet passes through the already-decelerated flow, stalling propagation at the top of the packet and creating a kink in the phase lines that encourages overturning (see Figure 2.5).

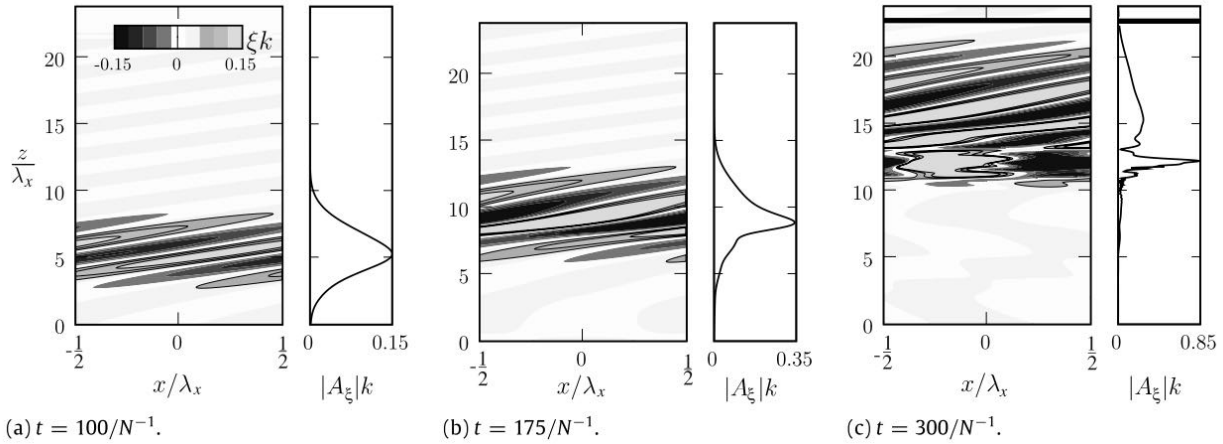

Figure 2.4: A non-hydrostatic GW packet exhibiting modulational instability, shown in the normalized vertical displacement field and the corresponding amplitude envelopes before (a), during (b), and after (c) onset. The black line in Panel (c) shows the expected breaking altitude from linear theory. Taken from *Dosser and Sutherland (2011b)*.

The bottom of the packet is vertically compressed, sharpening the gradients and increasing the local Ri to encourage instability.

2.3 Gravity Wave Breaking and Instability Evolution

Linear theory approximates the tendency for GW breaking where the wave amplitude, given by

$$A = \frac{(-\partial\theta'_{GW}/\partial z)_{max}}{\partial\overline{\theta}/\partial z} \quad , \tag{2.21}$$

approaches 1 as $N^2 \to 0$ (Hodges, 1967). This is known as the convective instability condition, where the vertical gradient of the temperature becomes smaller than the adiabatic lapse rate and unstable stratification leads to overturning. The convective instability condition can be equivalently expressed in terms of the GW horizontal wind perturbation threshold

$$u' > |c - U| \quad , \tag{2.22}$$

at which point the GW amplitude is suppressed to $u' = N/|m|$, a condition known as GW saturation. The ratio of the vertical gradients of U and N is given by the Richardson number,

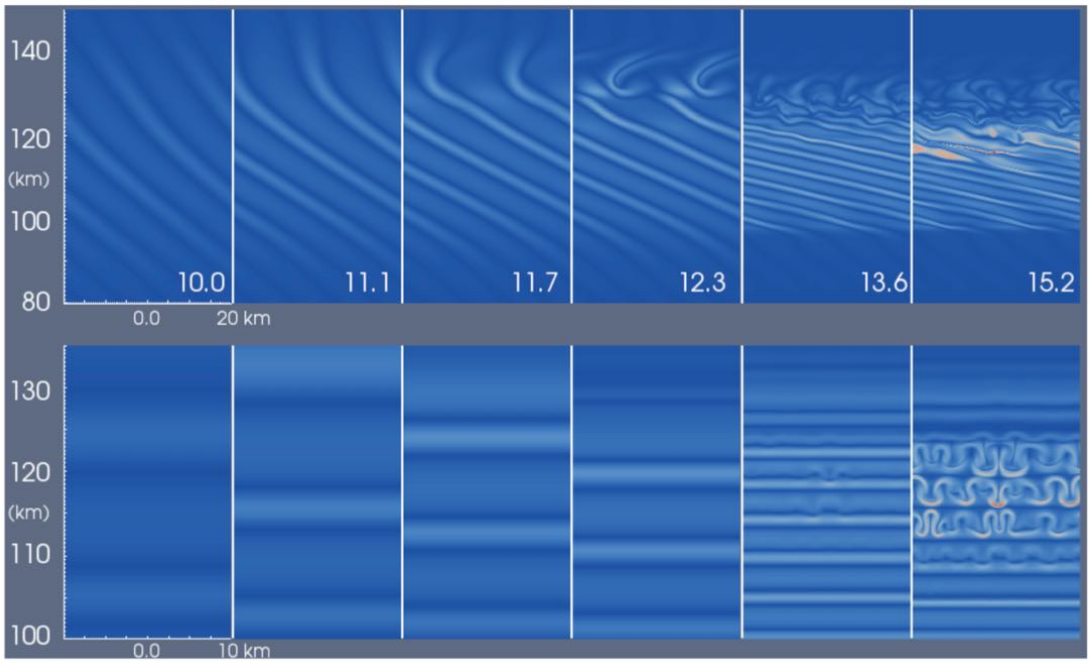

Figure 2.5: A GW packet undergoing SA, shown in the streamwise (top) and spanwise (bottom) components of the vorticity magnitude. Taken from *Fritts et al. (2015)*.

$$Ri = \frac{N^2}{\left(\frac{\partial U}{\partial z}\right)^2} \quad , \tag{2.23}$$

which indicates convective instability conditions when $Ri < 0$. Shear instability is predicted and seen to occur when $0 < Ri < 0.25$, a condition met in regions of high vertical shear that generally leads to the formation of a Kelvin-Helmholtz instability (KHI).

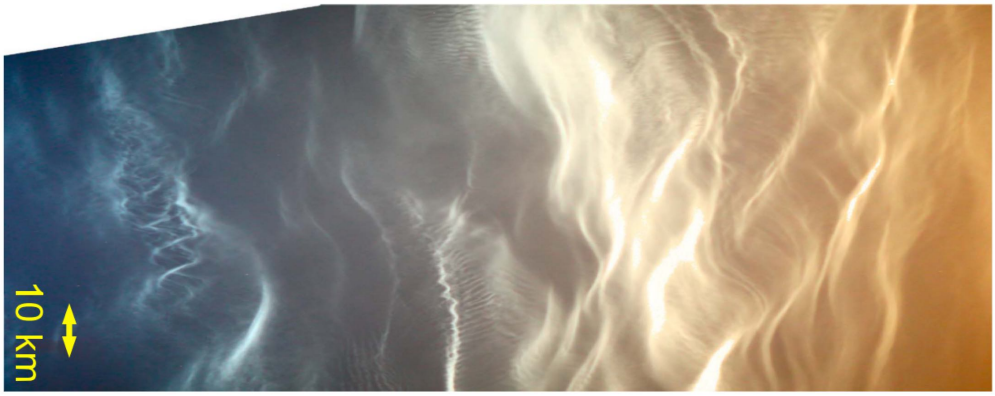

Figure 2.6: Complex instabilities and GW breaking dynamics observed from ground based polar mesospheric cloud (PMC) images. Taken from *Baumgarten and Fritts (2014)*.

The vortical evolution of a flow reveals the physical mechanisms that produce rotational tendencies leading to instability formation. Vorticity is defined as the curl of the velocity field,

$$\zeta = \nabla \times U = \left(\frac{\partial w}{\partial y} - \frac{\partial v}{\partial z}, \frac{\partial u}{\partial z} - \frac{\partial w}{\partial x}, \frac{\partial v}{\partial x} - \frac{\partial u}{\partial y} \right) \tag{2.24}$$

where $U = (u, v, w)$ are the velocity components in the streamwise (x), spanwise (y), and vertical (z) directions, respectively. Using this convention, the spanwise component of vorticity, $\zeta_y = \frac{\partial u}{\partial z} - \frac{\partial w}{\partial x}$, is the rotational tendency of a flow in the streamwise-vertical (x-z) plane. Positive (negative) ζ_y denotes (counter)clockwise rotational tendencies or strong positive (negative) shear in the presence of small $\frac{\partial w}{\partial x}$, such that regions of strong vertical shear in the background wind have corresponding ζ_y rotational tendencies. Because a rotating region of positive $\frac{\partial u}{\partial z}$ transforms to negative $\frac{\partial w}{\partial x}$, shear layers undergoing advective rotation retain their initial ζ_y sign and magnitude. Streamwise-aligned vortices also evolve spanwise-vertical (y-z) ζ_x components as they become 3D. As with ζ_y, $\zeta_x = \frac{\partial w}{\partial y} - \frac{\partial v}{\partial z}$ is the streamwise vorticity component which describes clockwise (positive) and counterclockwise (negative) rotational tendencies in the spanwise-vertical (y-z) plane. A sample schematic of the streamwise and spanwise vortical structure in a KHI is shown in Figure 2.7.

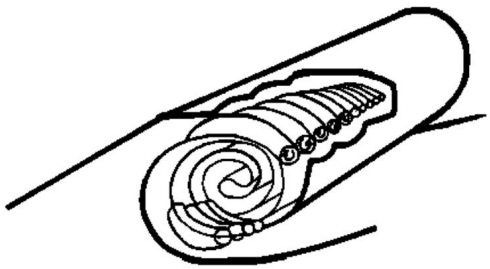

Figure 2.7: Schematic drawing of the vortical structure in KHI billow. Using the axes conventions above, the dominant billow structure in the streamwise (left to right) direction is comprised of ζ_y vorticity, while the counter-rotating rolls forming in the spanwise direction (into the page) correspond to ζ_x vorticity. Taken from *Thorpe (1987)*.

Baroclinic sources and sinks are important ζ_y sources that occur as misaligned local

pressure and density gradients generate corresponding rotational tendencies. The baroclinic term of the vorticity equation is given by

$$\left(\frac{\partial \zeta_y}{\partial t}\right)_{baroclinic} = \frac{1}{\rho^2}\left(\nabla\rho \times \nabla P\right)_y = \frac{1}{\rho^2}\left[\left(\frac{\partial \rho}{\partial z}\right)\left(\frac{\partial P}{\partial x}\right) - \left(\frac{\partial \rho}{\partial x}\right)\left(\frac{\partial P}{\partial z}\right)\right] \quad . \tag{2.25}$$

For instability evolutions that remain largely 2D in their early stages, dissipation and spanwise gradients remain relatively small, making

$$\frac{\partial \zeta_y}{\partial t} \sim \frac{1}{\rho^2}\left(\nabla\rho \times \nabla P\right)_y \tag{2.26}$$

a reasonable approximation. Baroclinic sources and sinks are most active in regions containing strong horizontal temperature gradients, noting that Equation 2.25 can be approximated as

$$\frac{1}{\rho^2}\left(\nabla\rho \times \nabla P\right)_y \approx -g\frac{\partial}{\partial x}\left(\frac{\theta'}{\overline{\theta}}\right) \tag{2.27}$$

for an isothermal atmosphere, given that

$$\left(\frac{\rho'}{\overline{\rho}}, \frac{P'}{\overline{P}}\right) << 1 \quad and \quad \frac{\partial}{\partial x, \partial z}\left(\frac{\rho'}{\overline{\rho}}, \frac{P'}{\overline{P}}\right) << 1/H \quad . \tag{2.28}$$

Strong baroclinic sources can develop in regions of locally high N^2 (i.e., regions exhibiting a large vertical temperature gradient) as a GW passes through. A sample observation of GW-induced layer rotation is shown in Figure 2.8, where a noctilucent cloud image shows instabilities forming in a thin, rotating layer. The GW's high amplitude produces large vertical velocities, which advect the layer up and down locally in the phase with the GW. Between the regions of upward and downward displacement, the initially-vertical temperature gradient in the layer rotates and develops a significant horizontal component, generating a baroclinic vorticity source. Such regions produce local vorticity enhancements that accelerate the evolution of instabilities.

2.3.1 Characteristic Instability Structures

When GWs break, they have several characteristic instability structures through the evolution of turbulence. Initial instabilities take the form of counter-rotating vortex rolls

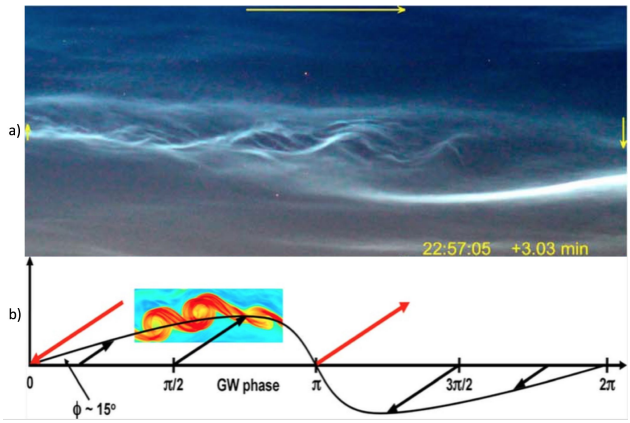

Figure 2.8: (a). High resolution noctilucent cloud image showing upward and downward layer displacement induced by alternate phases of a GW. Reorientation of sharp vertical temperature gradients can generate baroclinic sources and sinks as the dominant temperature gradients develop a significant horizontal component. In this case, KHI and secondary instabilities form in the rotated region of the layer between GW phases, where baroclinic sources are likely enhancing the local vorticity. (b). Schematic of KHI formation on a GW crest as it passes through a region of high stratification, where the black line indicates constant potential temperature and the red and black arrows indicate GW velocities and air parcel displacements, respectively. Taken from Baumgarten and Fritts (2014).

occurring in the spanwise-vertical plane (ζ_x streamwise vorticity), with intensified sheets of vorticity above and below. When the vortex rolls extend down to the coldest phase of the GW, they stretch and intensify the spanwise vortex sheets to produce a series of vortex rings (see Figure 2.9). These rings grow with time and advect upward, producing a downward plunging motion in the direction of GW propagation and creating a link between successive wavefronts that organizes transitional instability structures (Fritts et al. (2017)).

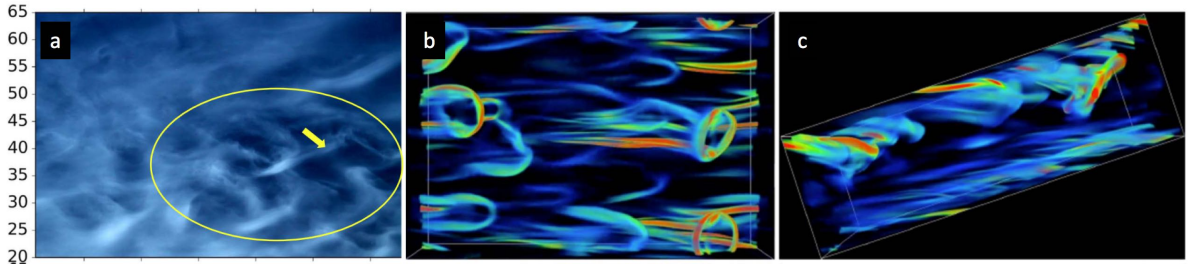

Figure 2.9: Vortex ring formation shown in ground observations of polar mesospheric clouds (left) and GW breaking simulations (middle and right). The simulation panels are the bottom (left) and side (right) views of the negative eigenvalue λ_2 of $\boldsymbol{L} = \boldsymbol{\Omega}^2 + \boldsymbol{S}^2$, where $\boldsymbol{\Omega}$ and $\boldsymbol{S}$ are the rotation and strain tensors. Taken from *Fritts et al. (2017)*.

Adjacent vortices then develop so-called *twist waves* through axial vortex stretching, radial vortex displacements, and vortex flattening caused by divergent radial advection (Andreassen et al., 1998; Fritts et al., 1998). The complex evolution of twist wave vortical structures determines the character of the turbulence evolution and the energy cascade to smaller spatial scales. Turbulence is responsible for the reduction in GW amplitude and the majority of the potential temperature and velocity variance in GW breaking (Fritts et al., 2009c).

GW dissipation, energy deposition, and momentum deposition systemically involve *sheet and layer* structures, which are comprised of thin, sharply stratified shear sheets interspersed among thicker layers with weaker stratification and shear (see Figure 2.10). High resolution modeling indicates that sheet and layer structures form naturally when GWs interact with spatially and temporally localized variations in background wind. Numerous observations (see Fritts et al., 2017, and citations therein) show a near-ubiquitous distribution of atmospheric sheet and layer structures from the surface to 100 km, and these multiscale interactions produce highly localized instabilities and GW enhancements.

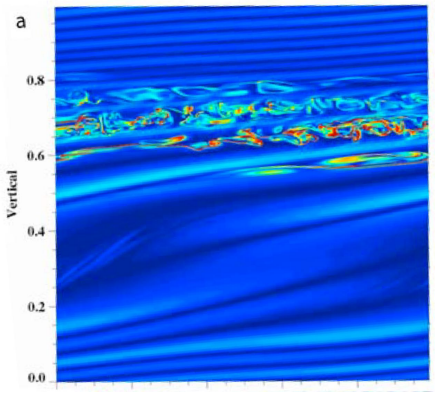

Figure 2.10: Sheet and layer structures, with alternating thin "sheets" of high shear/stratification and thicker "layers" of lower shear/stratification, forming as GW breaking produces local enhancements to the mean wind and stability. Vorticity magnitude from multiscale DNS taken from *Fritts et al. (2009a)*.

KHI frequently accompany GW breaking when sharpened vertical gradients in shear sheets drive Ri below 1/4. Low-Ri KHI are identifiable by a rounder (rather than oval)

shape, and high-*Re* KHI have sharp braids and develop initial turbulent structures in the braid rather than the core (Patnaik et al. (1976)). The transition to turbulence is identified by counter-rotating spanwise vortex pairs having initial scales and locations determined by *Re* (see Figure 2.11), with the coherent 2D structure of the billow retained well into the evolution of turbulence (Brown and Roshko (1974)).

GW breaking dynamics are highly localized, transient, and dependent on their environment, and their evolution and associated instabilities ultimately determine the GW impact on the background flow. Turbulence variances show localized instability evolution within the GW phase structure, with differing orientations significantly altering the final state (Fritts et al. (2009b)). The complex interplay between persistent 2D structures and 3D turbulence dynamics produces unique energy/momentum deposition characteristics that are difficult to predict, and they require further study to improve their understanding and characterization.

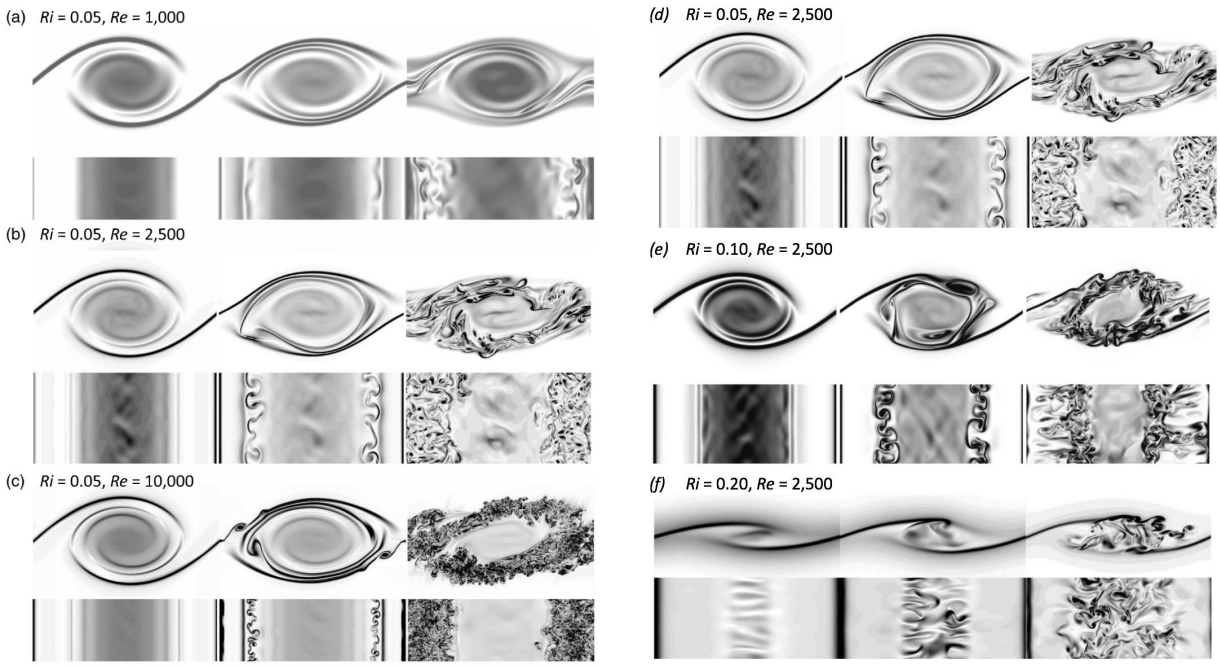

Figure 2.11: DNS showing KHI character and secondary instability structure through turbulence onset for increasing *Re* (a-c) and increasing *Ri* (d-f). Each panel includes vertical-streamwise (top) and horizontal spanwise (bottom) views at times before, during, and after the initial turbulence onset. Taken from *Fritts et al. (2014c)*.

2.4 Summary

GWs propagate vertically throughout the atmosphere, coupling the dynamics of different atmospheric layers as they transport energy and momentum over large altitude ranges. Linear propagation dynamics of GWs are well documented in theory and observation, and GW breaking dynamics have been shown to follow several characteristic morphologies despite the high degree of variability when the flow becomes nonlinear. While the fundamental dynamics of GW propagation are well understood, many of the complexities of localized, nonlinear GW interactions and environmental influences still remain unknown, motivating further studies to diagnose these dynamics.

Chapter 3

Motivations for This Study

3.1 Wave Evolution Complexities Caused by Environmental Influences

GWs evolve through a complex series of interactions as they propagate vertically through the atmosphere. Density drop-off with altitude increases wave amplitudes and encourages overturning instabilities. GWs have varying degrees of attenuation and transmission as they propagate through successive environments that promote different instabilities, with surviving waves having reduced amplitude and altered ω as a consequence of partial breaking below. Wind shears from large scale influences (mean wind, planetary waves, or larger GWs) and small scale influences (localized instability and continuous sheet and layer structures) expand or contract λ_z, and the associated N^2 variations promote shear instabilities at N^2 maxima and convective instabilities where $N^2 \rightarrow 0$ (Fritts et al. (2017)).

3.2 Influence on Large Scale Atmospheric Dynamics

Atmospheric GWs transport significant amounts of energy and momentum as they propagate, with HFGWs having the largest momentum fluxes ($\rho\overline{u'w'}$) and hence the dominant influence on momentum transport. Energy and momentum fluxes become more significant at higher altitudes due to lower densities, with GWs causing the majority of wind shear variance in the MLT (Fritts et al. (2017)). Though only $\sim 0.1\%$ of GW energy from the troposphere reaches the MLT, GW velocity variances are 2 decades larger near the mesopause than near the tropopause (Balsley and Garello (1985)), and mechanical energy dissipation

rates are 2 decades higher than in the stable troposphere and stratosphere (Lawrence and Balsley (2013)).

These heightened energetics enable GW propagation to cause significant seasonal variations in the MLT. Radiative heating predicts strong zonal winds up to the mesopause (100 km), yet observed winds at these altitudes show a significant decrease in amplitude above 50 km, even reversing directions at times. This discrepancy was studied intensively in the 1970s and eventually attributed to local flow decelerations caused by GWs depositing momentum when they attenuate or break (Tsuda (2014), see Figure 3.1).

Considering the complex dynamics of GW evolution in the MLT revealed by observations and simulations, and noting the demonstrated utility of simulations supporting observational data, a number of critical needs can be identified for which more advanced characterization of GW-FS dynamics in the MLT can make significant contributions.

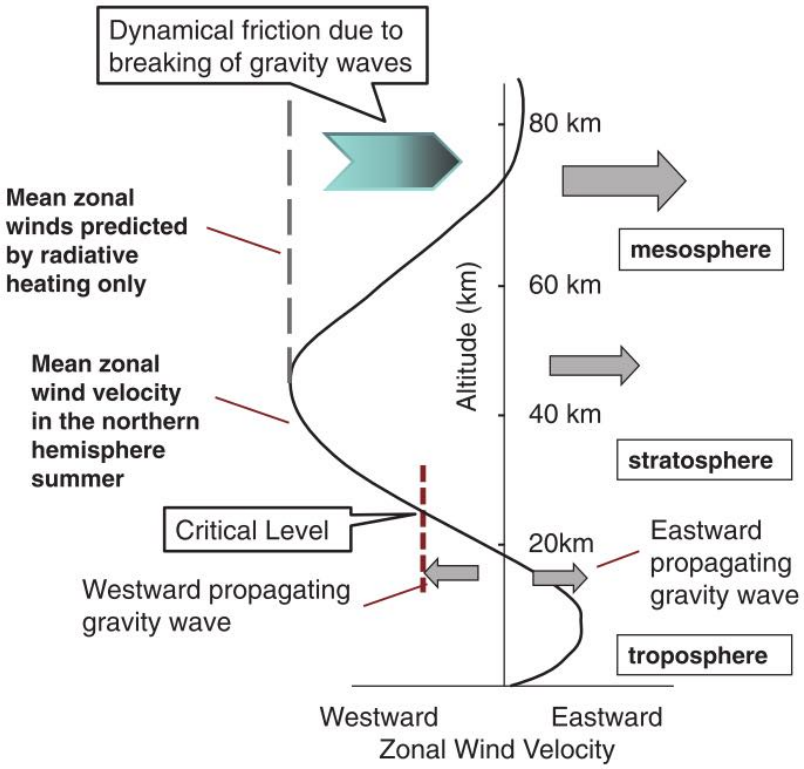

Figure 3.1: GW-mean wind interactions in the atmosphere from linear theory, taken from *Tsuda (2014)*.

3.3 Limitations in Observable Dynamics

Observations of GW influences in the MLT cover multiple decades of spatial and temporal scales, but no individual instrument or methodology completely resolves any one dynamical phenomenon, and even synergistic campaigns combining data from multiple sources have significant scale gaps. Single site observations, such as ground-based lidar and radar, provide high time resolution but often lack horizontal coverage, though networked observations can improve on this. Networked airglow imagers and satellite measurements provide wide spatial coverage but are constrained both in horizontal resolution and vertical extent, averaging over the vertical depth of the airglow layer ($\approx 7\ km$) and smearing out small-scale variations as a consequence. Several recent campaigns, including the Deeply Propagating Gravity Wave experiment in New Zealand (DEEPWAVE), combined multiple instruments and modeling for simultaneous characterization of GW influences from the stratosphere to the lower thermosphere. Early results (see Fritts et al. (2016)) show a promising range of GW propagation characteristics influencing large scale dynamics at scales far below what can be resolved by weather models, yet such detailed coverage for data assimilation into models is prohibitively expensive and impractical.

3.4 Unresolved Dynamics Driving Observable Mesoscale Phenomena

A number of mesoscale dynamics in the MLT are significantly influenced by HFGW propagation and energy/momentum transport at scales below those resolved by mesoscale and global circulation models and measurements (Liu (2016)). Traveling planetary waves, equatorial waves, and atmospheric tides all experience amplitude and phase modulation caused by changes in background winds in their propagation environments. HFGWs are a significant source of variability since their transports and deposition of energy and momentum can be highly variable, yet most planetary wave studies fail to resolve the scales at which GW interactions occur. Tidal variability also contributes significantly to thermospheric and

ionospheric weather patterns, linking GW influences to a range of large scale features over a broad expanse of the atmosphere. The Cloud Imaging and Particle Size (CIPS) instrument on the ISS has also identified a number of unexplained polar mesospheric cloud (PMC) morphologies (so-called ice voids, ice rings, and mesospheric fronts/walls; see Thurairajah et al. (2013)) that are structurally similar to known or suspected GW influences seen in the MLT and in clouds at lower altitudes. However, the sources of these dynamics are too small to be resolved by CIPS.

3.5 Known Deficiencies of Global and Mesoscale Models in the MLT

3.5.1 Resolution Restrictions

Global models used in weather prediction fail to resolve the spatial scales necessary to characterize GW influences. The MLT has comparable temporal scales, but larger spatial scales and amplitudes than the lower atmosphere, and numerous studies have shown the capacity for considerable improvement when resolution is increased to $\mathcal{O}(10km)$ or better (Liu (2016)). Sato et al. (1999) found that 1 km or below vertical resolution was sufficient to produce stratospheric IGWs that matched observations. Ngan and Eperon (2012) found that reducing the time step in the UK MET weather model improves the characterization of small scale GW influences in the middle atmosphere, thus improving predictability. The JAGUAR model, which extends the GCM up to 150 km, found that 1.1^o resolution revealed significant GW influences in the thermosphere as well as GW susceptibility to tidal modulation (Miyoshi et al. (2014)). Liu et al. (2014) found that WACCM-resolved momentum fluxes agreed with satellite observations when the horizontal resolution was increased to 25 km, and Siskind (2014) found significant increases in momentum fluxes with corresponding increases in resolution of the NOGAPS-ALPHA model.

Mesoscale-resolving simulation results characterize much larger dynamical ranges than the coarser version of these simulations used in weather prediction. The larger momentum

fluxes, energies, and GW perturbations in more resolved simulations indicate a high degree of GW influence below the resolution limits of global models, a point further supported by the coarse models' inability to replicate observations. While these studies show promise, computational limitations necessarily constrain the resolution of current forecasting models and hence require parameterizations for high-frequency GW influences.

3.5.2 Wave Parameterization Problems

Geller et al. (2013) completed the first comprehensive comparison of mesoscale model GW parameterizations and observational data. The most significant difference between model and satellite data is the falloff of GW momentum fluxes with altitude, which occurs at a faster rate in satellite data than in most models. This could be an attribute of the coarse horizontal resolution of satellite measurements or a consequence of missing physical processes in the models.

While forecast models include an explicit parameterization for orographic GWs, they differ in their parameterization of GWs triggered by more variable sources. Models produce good agreement up to the stratosphere, but the differing GW parameterizations lead to significant variations in the MLT. Wave parameterizations in models also notably lack any characterization of secondary GW generation and 3D instability evolution due to GW breaking. It is critical to study the complexities of GW interactions in the MLT to enable their parameterization in global models that can approximate these dynamical effects (Liu (2016)).

Weather prediction models are further hampered by their inability to characterize nonlinear GW interactions and time-evolving background flow at small scales. Mesoscale models calculate momentum and energy transport for propagating GWs using Ray Theory (Bretherton, 1969), an Eulerian methodology that employs the steady-state Wentzel-Kramers-Brillouin (WKB) model (Lighthill, 1978) to trace GW propagation along distinct "rays". Ray Theory predicts GW adherence to the linear dispersion relation, indicating GW

reflection where $\omega = N$ and critical level absorption where $\omega = 0$ as discussed in Section 2.1. However, for thin regions of low or negative stability, turning layers play a more complicated role:

> "Generally it is not well understood how internal waves transmit and reflect from the mesosphere when the vertical scale of the waves is comparable to the scale of the background variations." - Nault and Sutherland (2007)

The application of Ray Theory in both atmospheric (Lindzen, 1981; Broutman et al., 2004) and oceanic models (Henyey and Pomphrey, 1983; Henyey et al., 1986) further assumes that GWs approaching a critical level imposed by time-evolving shear (i.e. an IGW) behave in the same manner as GWs approaching a stationary critical level, fully dissipating at small λ_z as m becomes large. The underlying Ray Theory assumptions that 1) GW amplitudes remain small, 2) GW propagation can be treated as instantaneous, and 3) background wind and temperature variations are gradual and evolve slowly all break down in the MLT, necessitating a better understanding of these dynamics to improve their reproduction in mesoscale models.

The steady-state assumption used in these models also does not account for transient GW contributions to the background wind, and it restricts changes to GW phase speed as the GW propagates. Bölöni et al. (2016) simulated GW propagation using the WKB model in its steady state formulation, transient formulation, and the transient model with GW breaking parameterization, comparing the results to a full large eddy simulation (LES). They found that adding transience to the WKB model restores the most significant dynamics of full LES, indicating that the impact of GW breaking and its associated turbulence is secondary to the influence of transient GW-mean flow contributions. This is a significant departure from the synoptic understanding of GW influence on the atmosphere, demonstrating the critical importance of including nonlinear wave-mean flow interactions in GW simulations.

Alexander and Barnet (2007) comment on this critical shortfall of GW parameterizations in mesoscale models:

> "The intermittent nature of gravity wave sources and gravity wave occurrence...means that time-averaged measures of their amplitudes and other properties will average large-amplitude wave events with weak events and noise and do not provide the constraints needed for gravity wave parameterizations used in global models. New analysis methods are needed to separately identify the properties of the wave events and their intermittency."

3.6 Summary

A range of complex nonlinear dynamics involving GW-FS interactions has been demonstrated in modeling studies and observations of the MLT. However, both observation and modeling of large scale, MLT phenomena suffer from limited resolution and an inability to characterize the complex small-scale dynamics known to influence the larger-scale flows and structure at these altitudes. There is thus a demonstrated need for an understanding of small-scale, temporally and spatially intermittent GW interactions with variable local and large-scale environments in the MLT to improve GW parameterizations in mesoscale and global scale models. High resolution simulation studies appear to be the most practical approach to addressing this goal.

Chapter 4

Observational Techniques for Studying the MLT

Observations of the MLT guide and motivate the simulation studies undertaken in this research. This chapter provides a brief overview of current state-of-the-art MLT observation techniques and the data provided by each instrument.

4.1 Airglow-based Observations

The airglow layer refers to the altitude range above 80 km in which energized atoms and molecules emit light. The light signatures from these molecules act as a passive tracer of the fluid dynamics moving the energized particles, and they can be observed by ground, airborne, and satellite instruments to measure temperature, wind, and density variations where the particles emit light. Different energetic particles occupy distinct altitude ranges that dictate where the MLT can be characterized by a given sensor.

4.1.1 Sodium Lidar

Light Detection and Ranging (lidar) instruments employ pulsed laser beams to determine the distance from the instrument to light emitting atoms. Laser pulses are sent out at a discrete frequency tuned to trigger resonant absorption and re-emission by specific species (see Figure 4.1a). A receiver detects the return signal and calculates the distance to the atoms from the time it takes the pulse to return. The integrated photon return data produces a vertical profile of particle densities that shows the vertical layering structure and

perturbations as particles are advected through the lidar beam.

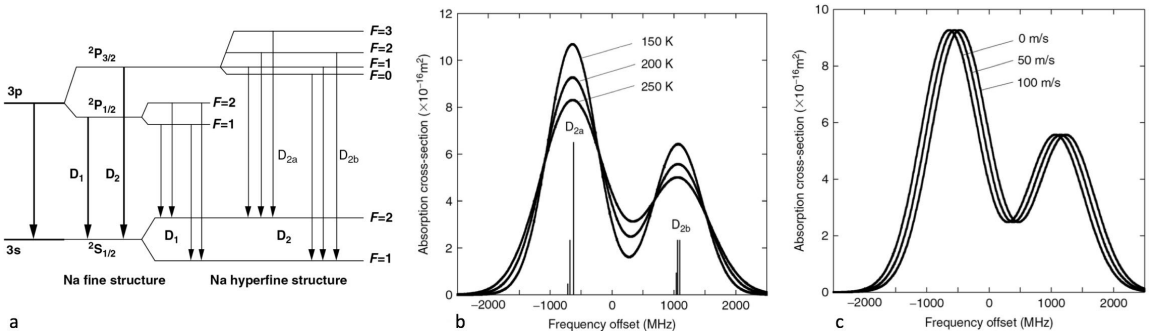

Figure 4.1: Na lidar wind and temperature measurement techniques. Electron energy transitions produce discrete emission spectra (a), and the spectral width of the return peaks approximates the temperature at these altitudes (b). Doppler shift measured from a scanning beam can also provide wind data (c). Taken from *Chu et al. (2012)*.

The sodium layer from 80 to 105 km makes sodium lidars ideal for MLT observations. The absorption line widths of the return signal provide sodium temperature measurements, and scanning breams use the doppler shift in the absorption spectra to calculate windspeed (Figure 4.1b and c). The sodium lidar used in Research Study 2, deployed at ALOMAR, Norway, is the same system described in Bossert et al. (2014). A brief overview of the system is given here. The resonance fluorescence sodium lidar (She et al., 2002) measures winds, temperatures, and sodium densities from ∼80 to 105 km. The lidar beams are tilted off zenith at 20^o to measure line of sight winds which are converted to meridional and zonal wind components. The beam footprint near 80 km is ∼40 m in diameter, and the meridional and zonal beams have a separation of ∼80 km. The range bins for the data presented in this study are 150 m. Temporal bins are averaged into 1.386 minute bins. A five bin boxcar smoothing is used for both altitude and time bins. The pseudo horizontal resolution depends on the local windspeed advecting structures through the beam. A sample lidar measurement is shown in Figure 4.2.

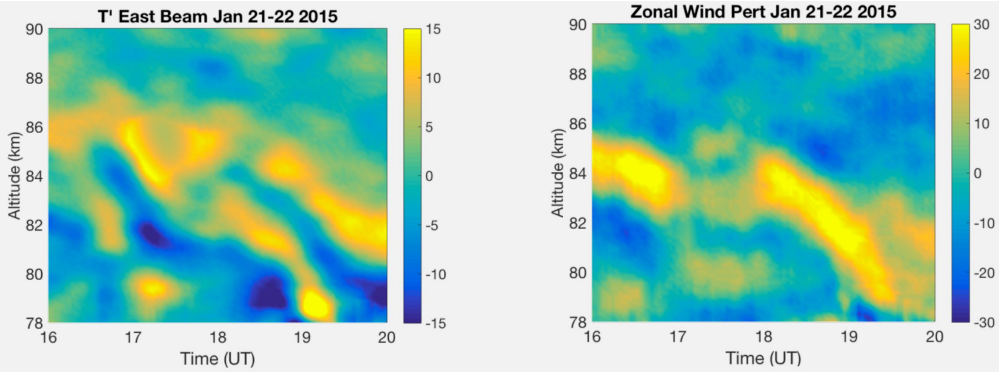

Figure 4.2: Na lidar wind and temperature perturbations measured at ALOMAR research station. Taken from *Bossert et al. (2016)*.

4.1.2 AMTM and ANI

The advanced mesospheric temperature mapper (AMTM, see Pautet et al. (2014)), also used in Research Study 2, is an optical instrument that measures temperatures from the rotation-vibration hydroxyl (OH) band that is located at 86.8±2.6 km with a full width at half maximum (FWHM) extent of $\sim$ 8 km (Baker and Stair, 1988; She and Lowe, 1998). An indium-gallium-arsenide camera captures the spectral peaks produced by the dominant OH vibrational modes, using their ratio to calculate temperature using the method of Makhlouf et al. (1995). The resulting 2D images show temperatures accurate to $\pm 2 - 4$ K over a 180 km x 144 km field with horizontal resolution of 0.5 km. Temperature measurements are produced every 30s, and data are averaged over the vertical depth of the OH layer. This high resolution sensor can characterize the horizontal properties of GWs and turbulence, including horizontal wavelength (λ_x), horizontal phase speed (c), and wave orientation. A sample image from Pautet et al. (2014) is shown in Figure 4.3.

The Aerospace Corporation's near-IR camera (ANI) is an OH imager that operates on the same principle as the AMTM. It produces a slightly smaller 120 km x 120 km viewing field with 0.5 km horizontal resolution, but the circuitry allows for 2s sampling to enable the characterization of faster-evolving thermal structures (Hecht et al. (2014)).

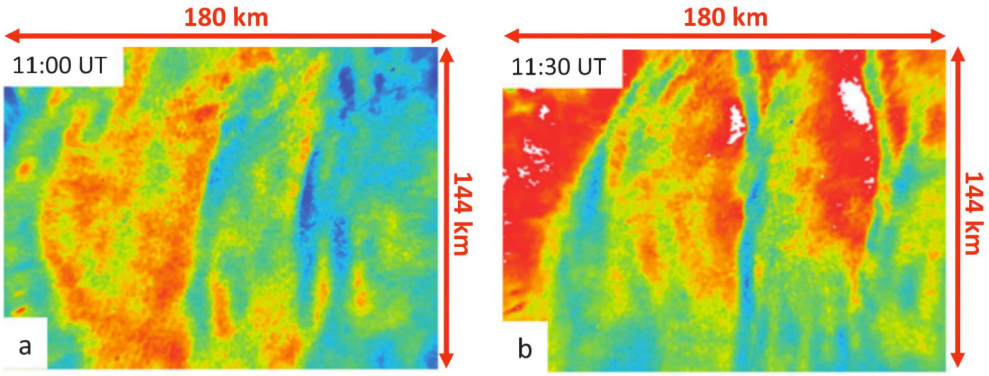

Figure 4.3: AMTM temperature measurement from the DEEPWAVE field campaign showing sawtooth temperature perturbations of a high-amplitude GW at two times. Taken from *Fritts et al. (2016)*.

4.2 Mesospheric Cloud Imagers

PMCs are the highest clouds in the atmosphere, forming near 80 km just below the mesopause at the coldest point in the atmospheric temperature profile. PMCs form during the summers in both the northern and southern hemispheres when the mesosphere is coldest and most humid, allowing the ice crystals to form in a thin vertical range often less than 1 km deep. Since the MLT is relatively dry most of the year, PMCs have a short observation season from $\approx$ 40 days before to $\approx$ 80 days after the summer solstice, and they generally occur at latitudes of 50^o or higher. The high altitude of the clouds enables them to be seen after dark (before dawn) when the sun is still (already) illuminating the mesosphere, giving them the alternate name noctilucent clouds or NLCs (Benze (2012)).

4.2.1 Ground-based Photography

Ground-based PMC imaging uses high-resolution cameras looking up at a slant angle with a wide field of view. The cameras employed by Baumgarten and Fritts (2014) use a two camera setup with a wider ($127^o \times 85^o$) and narrower ($9.5^o \times 6.3^o$) field of view to capture large scale influences and small resolvable features down to $\mathcal{O}(20 - 50m)$ with images captured every 3s. While the slant angle viewing makes it more challenging to visually distinguish

between horizontal feature separation and separation along the slant angle of the observation (through the 1 km cloud layer), the resolvable spatial resolution of the features in the images is higher than any other sensor viewing the MLT. A sample image set is shown in Figure 4.4.

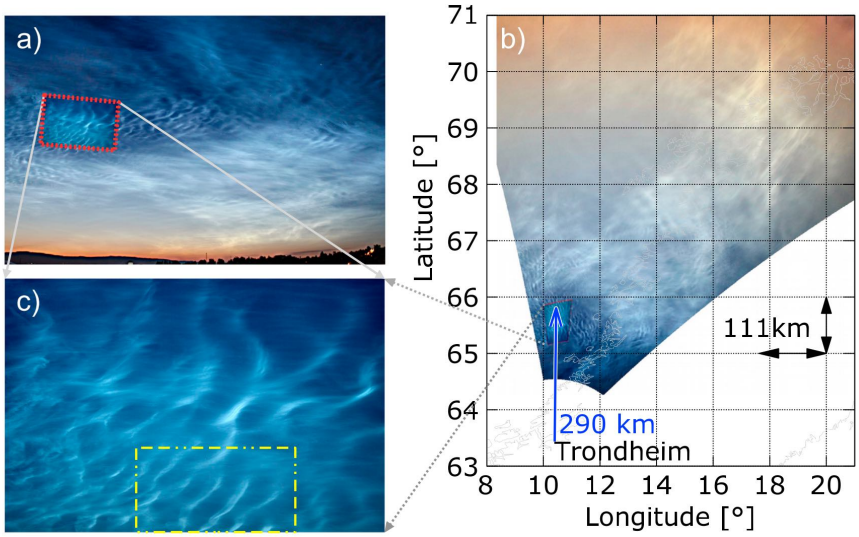

Figure 4.4: Ground based image from wider field of view camera (a) with projection on to latitude-longitude map (b) showing the location of features relative to the observer. The narrow field of view camera image (c) is located in the red box shown in (a) and (b). Taken from *Baumgarten and Fritts (2014)*.

4.2.2 Satellite Imagers

Space observations have the distinct advantage of being able to observe PMCs over the polar caps at any solar depression angle, day or night. The cloud imaging and particle size (CIPS) instrument employs a satellite-based ultraviolet imager on an orbital path that has near-complete polar coverage over its 15 daily orbits. The instrument has a 960 km x 1140 km field of view with spatial resolution of 5 km x 5 km pixels and a sampling rate of 1 image every 43 seconds. Cloud morphology data is measured by albedo, the ratio of scattered radiance to incoming solar radiance. A high degree of orbit overlap above 70^o latitude allows successive passes over the same structures with a 90 minute cadence, showing the temporal evolution of large scale features in the clouds. A sample image showing several ice ring measurements is shown in Figure 4.5 (Thurairajah et al. (2013)).

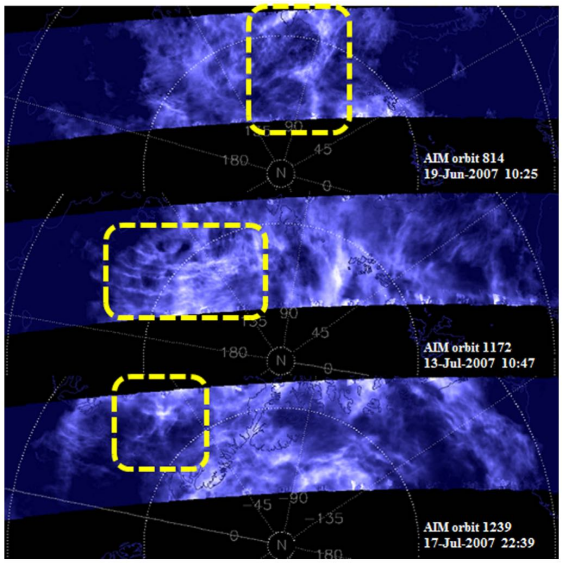

Figure 4.5: Ice ring structures in PMCs observed with the CIPS satellite instrument. Taken from *Thurairajah et al. (2013)*.

4.3 Summary

State-of-the-art observation techniques enable characterization of MLT dynamics over a broad range of spatial and temporal scales, with each instrument having unique resolving abilities and observational coverage. These instruments quantify many of the important GW and instability parameters used to characterize GW dynamics in this region, but no one instrument can characterize the horizontal, vertical, and temporal evolution of GW structures without the use of additional instruments. Using horizontal and vertically sampling instruments together (e.g., lidar and AMTM operating in unison) can more completely diagnose GW influences, and as a result, many satellites and ground observation centers operate multiple MLT instruments simultaneously for research campaigns. Though the data is comprehensive where the instrument domains intersect, a vertical profile running through a horizontal plane cannot approximate a 3D volume without some form of context provided by simulations.

Chapter 5

Gravity Wave-Fine Structure (GW-FS) Studies to Date

5.1 Idealized Modeling of Gravity Wave Interactions in MLT-like Environments

The first simulation studies of GW-FS interactions were conducted in 2009 (see Fritts et al., 2009a), using a triply periodic direct numerical simulation (DNS) code to characterize GW breaking dynamics down to turbulent scales. The study was unique in its use of a high resolution Boussinesq spectral code employing $Re \approx 10^4$ (10x larger than previous simulations), capable of resolving into the viscous range of turbulence. They found the impact of small scale dynamics to be significant, with highly time-variable turbulent structures and wave-wave interactions that alter the evolution of the flow. Comparing 2D and 3D simulations, they found that properly resolved 3D instabilities significantly reduce the amplitude of persistent 2D structures and secondary GW excitation. GW distortions of the fine structure were found to be highly dependent on the relative orientations of the features - GWs aligned with fine structures produced divergent vertical velocities that deepen the fine structure, while misaligned features produced divergent horizontal velocities that thin the layers, resulting in the formation of characteristic *sheet and layer* structures that increase the complexity of the environment and persist for long periods of time. It was also determined that a stable initial condition ($Ri \geq 1/4$) does not preclude the development of turbulence in a domain where many scales of interactions are actively evolving the flow.

Several recent studies have demonstrated the extent to which nonlinearity and realistic

Re enable complex flow dynamics in the MLT. Lund and Fritts (2012), using an anelastic simulation incorporating GW contributions to the mean flow, found that the inclusion of wave-induced mean flow leads to significant background wind variation at higher altitudes and a high degree of vertical wavelength (λ_z) compression in the trailing portion of the packet. The altered wind profile results in lower breaking altitudes and a higher likelihood of secondary GW generation. As a consequence, the vertical extent of ensuing turbulent structures is confined by a combination of sharper vertical gradients in the trailing packet and higher viscous dissipation discouraging instabilities at higher altitudes.

Several studies have also shown the potential for FS to promote GW propagation through critical levels and turning layers that defies conventional Ray Theory assumptions. Broutman et al. (1997) found that time-dependent critical levels imposed by IGWs do not completely prohibit GW propagation (contrary to the model assumptions used by Henyey et al. (1986)), showing that short GWs escape more readily through IGW critical levels when their vertical group velocity is less than the vertical phase speed of the IGW. Simulations by Walterscheid et al. (2001) showed that ducts can leak GW energy to higher altitudes when the evanescent region is shallow and the GW frequency is relatively high. Snively and Pasko (2008) found that GW energy can breach evanescent regions through both linear tunneling and nonlinear excitation of harmonic GWs. Sutherland and Yewchuk (2004) developed a formula to estimate GW transmission through an evanescent region as a function that depends on the ratios of ω vs. N (greater transmission for smaller $(\omega - N)$ when $\omega > N$) and k vs. the depth of the evanescent layer (greater transmission for thinner layers and smaller k). Follow-on studies by Nault and Sutherland (2007), Brown et al. (2008a), and Brown et al. (2008b) extended the transmission formula to arbitrary U and N profiles and determined the transmission dependence on amplitude (more transmission for higher GW amplitudes) and $\frac{m}{k}$ (more transmission for $\left|\frac{m}{k}\right| \approx 1$). These findings make a strong case for more observational studies of GW propagation through transient FS forcing in the MLT.

Nonlinear simulations of HFGW propagation through IGWs by Heale and Snively

(2015) demonstrate both 1) the inability of linear ray-tracing models to characterize GW transmission and filtering at critical layers and 2) the significant reductions in GW transmission resulting from steady-state (rather than time-evolving) background wind characteristics. They found that similar to the Fritts et al. (2009a) study, HFGW interactions with IGW perturbations are highly dependent on the relative orientation of the wave structures, such that a time-evolving background produces more conditions favorable to GW energy transmission to higher altitudes. This implies that any large-scale circulation model based on a steady-state assumption can significantly underestimate energy deposition and GW propagation in the thermosphere.

5.2 Observational Studies of Gravity Wave-induced Instabilities in the MLT

State-of-the-art observational studies of the MLT employ networks of ground based sensors and utilize simulation support to diagnose the dynamics in the observations and infer flow behavior in the surrounding volume. Being able to characterize observed dynamics with models can expand the domain and resolution of observations, contextualizing how they behave over broader spatial and temporal domains and verifying the dynamics producing features in the data.

To enable comparisons of models with observational data, Fritts et al. (2014c) developed a method to estimate GW and instability signatures in OH airglow based on potential temperature perturbations, treating OH as a passive tracer when instability dynamics are sufficiently rapid to advect OH brightness at short timescales. They found that 2D and 3D KH billow characteristics should be quantifiable in OH imagers for instabilities with sufficiently low Ri, enabling Re and Ri estimates from KHI scales. Snively et al. (2010) also developed an OH chemistry model that is adaptable for comparison with lidar and temperature mapper images.

Hecht et al. (2014) used this method to analyze ANI images over Chile, integrating the model results vertically to simulate airglow images with 500 m horizontal resolution viewed

from below and averaged with altitude. Approximating the local Re and Ri, DNS modeling provided an explanation for an observed instability structure that comprised counter-rotating rolls within a KHI. Diagnosing what appeared to be a relatively low Ri and relatively low Re, a KHI formed in this environment would be large and have its secondary instability development suppressed, matching what was observed. The KH features suggested an elevated turbulent viscosity that constrained the spanwise secondary instability features to larger scales than allowed by the true kinematic viscosity, roughly four times higher than expected at this altitude from the turbulent value ν_m and consistent with the findings of Hecht et al. (2005). Such a high viscosity value could occur in either 1) a low Re of 1000 at 87 km or 2) a high Re environment with elevated viscosity due to turbulence. The DNS also examined the influence of small-scale, turbulent dynamics enabled by the local Re and Ri below the resolution limits of the imager. When downsampled to the imager resolution, the fine scale features were impossible to distinguish (see Figure 5.1), showing that significant small scale dynamics could be influencing the observed dynamics beyond what can be identified by imagers alone.

Baumgarten and Fritts (2014) and Fritts et al. (2014a) used a ground-based imager to capture PMCs with extremely high temporal and spatial resolution. The slant angle viewing enabled characterization of fine structures in the clouds down to $\mathcal{O}(20 - 50\ m)$ without requiring vertical averaging as was the case for Hecht et al. (2014). The results showed that GWs play a major role in modifying the background stratification to evolve instabilities, exhibiting interactions over a broad range of spatial and temporal scales with considerable intermittency. Instability-estimated parameters in the simulations again produced structures that matched the observed morphologies down to turbulent scales, verifying the accuracy of Re and Ri estimates obtained from the PMC images. The results also displayed primary and secondary instability characteristics consistent with a higher kinematic viscosity over the expected molecular level, giving credence to the hypothesis of Hecht et al. (2014) that residual turbulence from near-continuous GW-FS interactions can lower the effective Re and

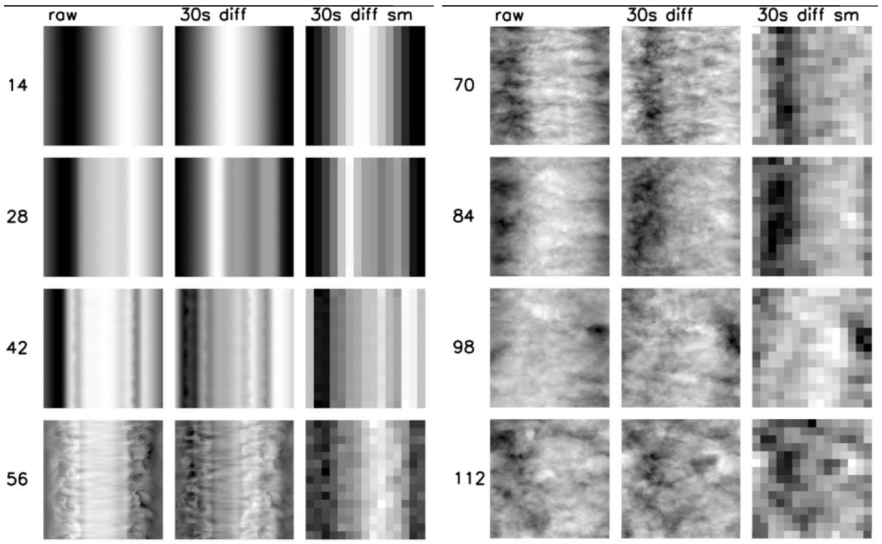

Figure 5.1: DNS of dynamics influencing PMC images, simulated with *Re* and *Ri* approximated from PMC instability scales. Each set of 3 images shows the raw simulation data (left), data averaged over two time steps (middle), and data downsampled to ANI resolution (right) at the time shown to the left of the images, showing that the small scale influences cannot be resolved or characterized by the ANI imager. Taken from *Hecht et al. (2014)*.

encourage large, coherent instability structures in the MLT.

Heale et al. (2017) conducted simulations of a large, multiscale MLT GW event measured by the DEEPWAVE campaign (see Bossert et al. (2015)). Lidar and OH imager data showed a range of vortical structures with GW and instability sources that were identified with the help of simulations (see Figure 5.2). Simulations also produced reconstructed state variable profiles over a broader altitude range than could be observed to diagnose the physical sources of observed behaviors in the flow. *Ri* profiles showed that instabilities in the HFGWs preferentially occur in the warm phase of the background tidal wave structures, primarily because the negative potential temperature gradients needed for convective instability occur most prominently above the warm phase of the tides. Airglow data also showed smaller scale wave structures that were diagnosed as secondary GW structures generated by multiscale wave interactions.

Fritts et al. (2017) evaluated turbulence characteristics observed by PMC ground im-

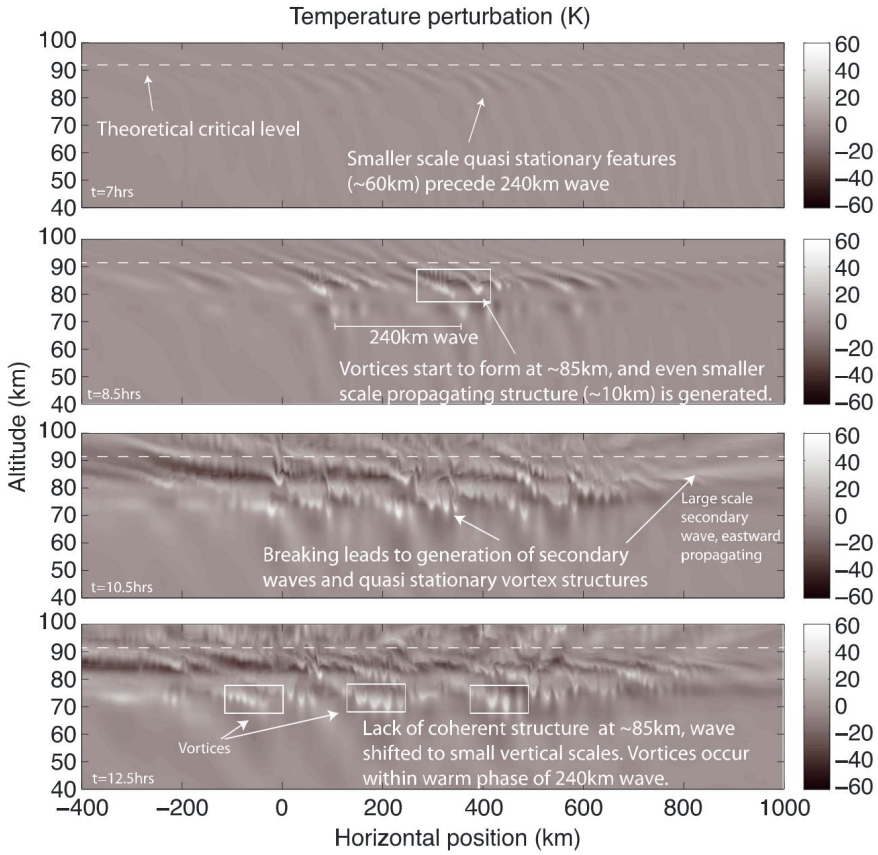

Figure 5.2: Simulation of a GW breaking event in DEEPWAVE using observational parameters to initialize the model. The simulations make it possible to distinguish vortical structures produced by GWs from vortex structures produced by instabilities. Taken from *Heale et al. (2017)*.

agers, using GW and instability scale estimates to study the dynamics of the observations with simulations. Observed PMC vortex rings identify the plane of GW propagation, allowing the approximation of GW λ_z and ω. A brightness profile with the approximated PMC depth is then applied to GW breaking DNS to identify analogous structures (see Figure 5.3). Making the appropriate scale conversion, the simulation data can then estimate the GW breaking contribution to the energy dissipation rate (ϵ) in the MLT, adding significant utility to the observations by enabling the calculation of quantitative turbulence parameters from the data.

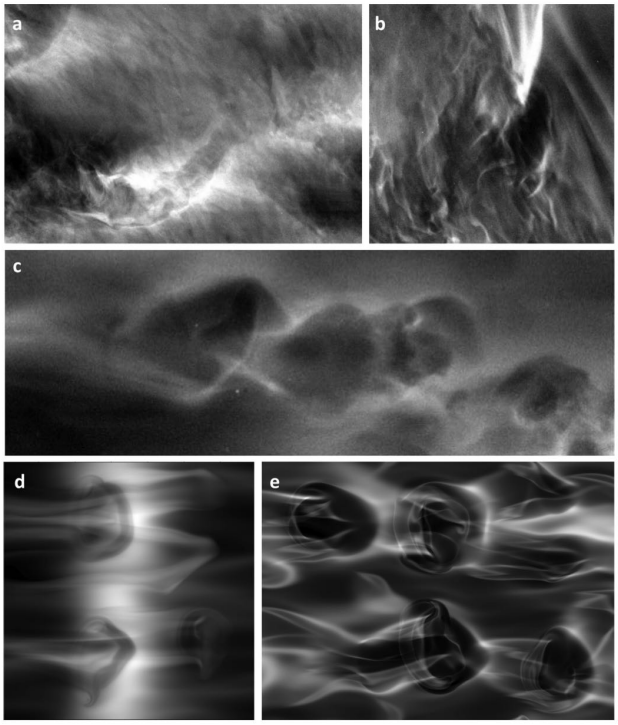

Figure 5.3: Vortex rings at various stages of evolution shown in PMC imagers (a-c) and reproduced in GW breaking DNS (d and e). Vortex rings observed in (c) outline the phase lines of a GW, enabling the approximation of λ_z and ω to compare with corresponding DNS results. Taken from *Fritts et al. (2017).*

5.3 Summary

Simulation-based studies of complex, nonlinear GW dynamics identify several dominant influences in more general GW-FS interactions and the extent to which the evolution of layering and energy transport characteristics depends on 3D, nonlinear dynamics at small spatial scales. Observational studies identify systemic GW-influenced layering and instability evolution patterns when GWs propagate through the MLT, providing explanations for unexpected physical behaviors and quantifying observational data with simulation diagnoses. Studies such as these demonstrate the potential for complex flow evolution enabled by GW-FS interactions and motivate further studies of this environment as observations reveal more unexplained phenomena.

The dynamics of GW-FS interactions are understood to be complex, but a comprehensive study isolating how specific aspects of these interactions determine GW propagation, energy and momentum transport, and background flow evolution has not yet been completed. Further, these dynamics have not been shown to exist elsewhere in the atmosphere where these same complex layering structures are known to occur. A simulation-based approach is needed to identify the quantitative influences of GW-FS interactions, verify these behaviors with observations, and determine their influence on the rest of the atmosphere.

Chapter 6

Numerical Model Simulation Architecture Employed in This Research

Current observational techniques lack the ability to view the interactions of fine scale structures over a sufficiently large vertical range to discern their influence on GW propagation and transport of energy and momentum. Modeling studies to date with a sufficiently large domain have not resolved the multiscale dynamics that dictate the evolution of the flow, and high resolution modeling efforts that can resolve these instability and turbulence dynamics have been confined to idealized Boussinesq flows to date. A suitable simulation architecture should capture the full range of active scales in GW-FS interactions in the MLT; such a code exists and is employed for all studies in this research.

6.1 Finite Volume Anelastic Code-Equations

The simulation studies in this research employ 3D finite-volume solutions to the anelastic Navier-Stokes equations following the formulation of Lipps and Hemler (1982) and Lipps and Hemler (1990), where density fluctuations are only considered in the buoyancy term. Here anelastic (no elastic energy) refers to the formulation in which sound waves are excluded and the timescale is set by the buoyancy frequency N. The equations employ a modified thermodynamic definition of potential temperature such that the system of equations conserves mass, momentum, total energy, and potential vorticity.

The equations in a non-rotating frame are

$$\frac{\partial \overline{\rho} u_j}{\partial x_j} = 0 \tag{6.1}$$

$$\frac{\partial \overline{\rho} u_i}{\partial t} + \frac{\partial \overline{\rho} u_i u_j}{\partial x_j} = -\frac{\partial p'}{\partial x_i} + \left(\frac{\overline{\rho} \theta' g}{\overline{\theta}} - \frac{p'}{H} \right) \delta_{i3} + \frac{\partial}{\partial x_j} \left[\mu \left(\frac{\partial u_i}{\partial x_j} + \frac{\partial u_j}{\partial x_i} \right) \right] \tag{6.2}$$

$$\frac{\partial \overline{\rho} \theta}{\partial t} + \frac{\partial \overline{\rho} \theta u_j}{\partial x_j} = \frac{\overline{\theta}}{c_p \overline{T}} \left[\mu \left(\frac{\partial u_i}{\partial x_j} + \frac{\partial u_j}{\partial x_i} \right) \frac{\partial u_i}{\partial x_j} - \frac{\partial}{\partial x_j} \left(\kappa \frac{\partial T}{\partial x_j} \right) \right] \tag{6.3}$$

where the solution variables are the wind components $u_i = (u, v, w)$, the potential temperature θ, and the pressure fluctuation p'. c_p is the specific heat at constant pressure and δ_{ij} is the Kronecker delta. μ and κ are the molecular viscosity and thermal conductivity, respectively, and they are related to temperature through Sutherland's law,

$$\mu = \mu_0 \frac{T_0 + c}{T + c} \left(\frac{T}{T_0} \right)^{\frac{3}{2}} \tag{6.4}$$

where c is Sutherland's constant for air, $c = 110K$. The anelastic definition of the potential temperature fluctuation,

$$\frac{\theta'}{\overline{\theta}} = -\frac{\rho'}{\overline{\rho}} + \frac{p'}{\overline{\rho} g H} \tag{6.5}$$

relates p', ρ', and θ' to the scale height H as defined in Equation 2.18 in Chapter 2. Temperature is defined with a linearized form of the ideal gas law

$$\frac{T'}{\overline{T}} = \frac{p'}{\overline{p}} - \frac{\rho'}{\overline{\rho}} = \frac{\theta'}{\overline{\theta}} + \frac{p'}{\overline{p}} \left(1 - \frac{\overline{p}}{\overline{\rho} g H} \right) \quad , \tag{6.6}$$

and the dispersion relation then takes the form

$$\omega^2 = \frac{k^2 N^2}{k^2 + m^2 + 1/4H^2} \quad . \tag{6.7}$$

GW perturbations are initialized in the form

$$\psi' = \psi_0 e^{i(kx + m_0 z - \omega_0 t)} \tag{6.8}$$

where $k = 2\pi/\lambda_x$ and $m = 2\pi/\lambda_z$ are the horizontal and vertical wavenumbers, λ_x and λ_z are the horizontal and vertical wavelengths, and $\omega_0 = k(c - U_0[z])$ is the initial intrinsic frequency in the reference domain.

The anelastic equations are discretized using the scheme presented in Felten and Lund (2006), which contains no artificial dissipation. Each simulation is run in 3D with a weak noise spectrum added to the $T(x, y, z)$ field to facilitate instability formation. A dynamic LES implementation provides further confidence in the energetics, using an evolution of the subgrid-scale eddy viscosity model developed by Germano et al. (1991) to determine an eddy viscosity appropriate to the flow state.

6.2 Code Capabilities

Developed to enable deep atmospheric simulations that can characterize instabilities through the onset of turbulence, the code architecture has many capabilities that make it ideally suited for GW simulation studies in the MLT, including

(1) The code architecture has sufficient spatial resolution to resolve the fine-scale vertical and horizontal structures identified by lidar and PMC imagery (Baumgarten and Fritts (2014)), down to $\mathcal{O}(10\ m)$. The code can characterize scales of interest to turbulence without requiring any assumptions of parameterizations, due to its ability to resolve the inner scale of turbulence for Re representative of the MLT.

(2) The code architecture simulates a 3D environment that properly characterizes the evolution of instabilities and their effects on the evolution of the flow environment. As demonstrated in the findings of Andreassen et al. (1994), Fritts et al. (1994) and numerous subsequent studies, GW breaking and the resulting turbulence are fundamentally 3D processes, and the resulting GW amplitudes and transport dynamics would not be accurately characterized by 2D simulations that constrain the vortical structures and energy evolution of the flow.

(3) The code architecture can run with a large vertical and horizontal domain that encompasses the influential dynamics of GW-FS interactions in the MLT. Large

computational resources allow for a tall/wide domain that avoids confining the spatial modes of the local GW dynamics that would produce spectral artifacts at the domain scales. A low domain minimum altitude allows GW propagation up to the MLT with physically grounded initial conditions, and a high vertical ceiling allows characterization of energy transport and propagation effects extending to higher altitudes.

(4) The anelastic code is designed to accommodate exponential density that enables realistic dynamics at higher altitudes emerging from perturbations lower down. Density and GW amplitude scaling allow realistic GW propagation conditions, enabling simulations over many scale heights that aren't inhibited by the Boussinesq approximation.

(5) The inclusion of transient GW mean flow contributions ensures that the code architecture accounts for the dominant dynamics known to influence MLT GW propagation, as per the findings of Bölöni et al. (2016) and Dosser and Sutherland (2011b).

6.3 Background Profile Generation for FS Studies

The background profiles employed in Study 1 and Study 3 apply isolated FS to the background stability and wind profiles that are prescribed as

$$N^2[z] = N_0^2 + \left(N_1^2 - N_0^2\right)\ sech^2\left[\frac{z - z_0}{d}\right] \tag{6.9}$$

$$U[z] = U_0 + \frac{U_1 - U_0}{2}\left(1 + tanh\left[\frac{z - z_0}{d}\right]\right) \tag{6.10}$$

where N_0 and N_1 are the background and peak Brunt-Vaïsala frequencies, U_0 and U_1 are the background wind speeds below and above the prescribed shear layer, z_0 is the altitude of the center of the layer, and d is the half layer depth. Uniform wind and stability profiles are generated by setting $N_1^2 = N_0^2$ and $U_1 = U_0$. The background temperature is initialized as

$T = 240K$ at the lower boundary, with a density scale height of 7 km and a background N of $0.02s^{-1}$ representing a mean over the lower and middle atmosphere. The resulting buoyancy period is $T_B = 2\pi/N = 314s$.

The background wind and temperature profiles used in Study 2 are generated directly from observational data. Lidar and Saura data from the event are fit together with a sum of sine function and smoothed with the desired $(U,T)_0$ using a *tanh* function smoothed over 2 km. This produces piecewise functions of U and T defined as

$$U,T(z) = \begin{cases} (U,T)_{lidar} \times F + (U,T)_0 \times (1-F) & z \leq 105\ km \\ (U,T)_{lidar\ |\ z=105\ km} & z > 105\ km \end{cases} \tag{6.11}$$

where

$$F = \frac{1}{2}\left(1 + tanh\left[\frac{z - z_{min}}{2km}\right]\right) \tag{6.12}$$

is the *tanh* smoothing function, where z_{min} is the bottom altitude from the U,T profiles selected for optimal smoothing with $(U,T)_0$ that minimizes artifacts.

6.4 Parameter Definitions

For prescribed shear and/or N^2 layers using Equations 6.9 and 6.10, the initial minimum Richardson number (Ri) is given by

$$Ri_{min} = \left(\frac{N^2[z_0]}{\left(\frac{\partial U}{\partial z}\right)^2[z_0]}\right) = 4N_1^2\left(\frac{d}{U_1 - U_0}\right)^2 \quad . \tag{6.13}$$

The dominant Reynolds number in the initial condition can be calculated either from the shear layer parameters,

$$Re = \frac{(U_1 - U_0)\,d}{2\nu} \tag{6.14}$$

or from the GW scales, given by

$$Re = \frac{\lambda_z^2}{T_B \nu} \quad , \tag{6.15}$$

with Equation 6.15 used for all studies herein. The molecular Prandtl number for the atmosphere is set at 1 to have the same resolution constraints for the velocity and temperature fields, slightly higher than the expected Pr of ~ 0.7. As a consequence of this choice, there will be a slight increase in prominence of smaller scale structures in the temperature field relative to the velocity than in the real atmosphere (Dong et al., 2016) and a slight reduction in mixing efficiency (Rahmani et al., 2016). To seed the instability formation, a white noise spectrum is added to the initial temperature field, with an amplitude roughly 10^{-5} of the initial temperature perturbations prescribed in the GW.

6.5 Vertical Mesh Configurations

For Studies 1 and 2, a meshing routine was devised to apply a power-law stretched vertical grid with enhanced resolution at a specified altitude. The mesh is determined by an iterative routine that determines the power law stretching parameters to meet pre-specified requirements for altitude domain limits, desired altitude of resolution maximum, and maximum allowable grid spacing in the domain. The vertical mesh used in all simulations from Study 1 is shown in Figure 6.1.

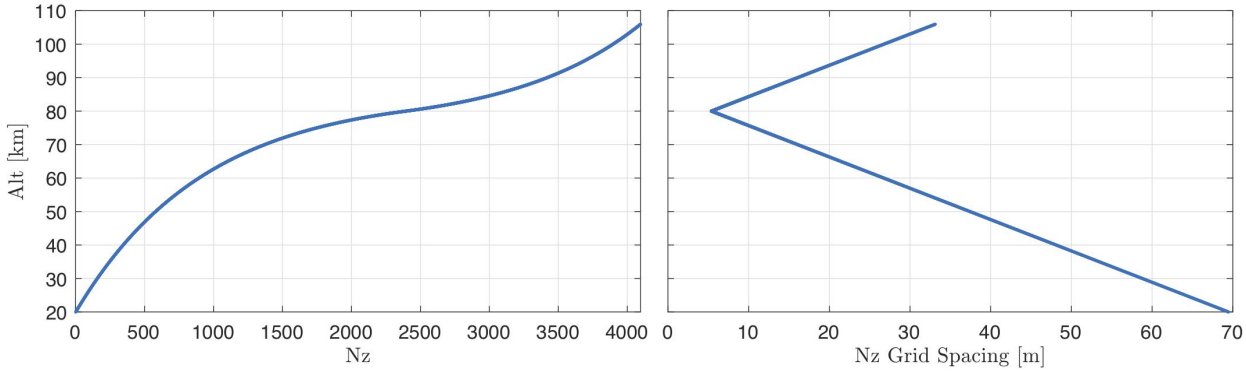

Figure 6.1: Vertical mesh incorporating power law stretching about 80 km, shown in terms of point layout and vertical spacing as functions of altitude.

For Study 3, a revised power-law stretching routine was devised to replace the stretching formula in the region of maximum resolution with a region of fixed grid resolution about 80

km. This altitude range has a maximum resolution matching the streamwise and spanwise grid spacing, such that the instability dynamics about the imposed layer at 80 km can be evaluated in a constant resolution region while still taking advantage of grid stretching above and below. A sample of this grid configuration is shown in Figure 6.2, plotted with minimum grid spacing of 10 m, 20 m, and 30 m. For simulations in Study 3 with grid spacing greater than the maximum spacing used in Study 1, a simple uniform vertical grid is employed.

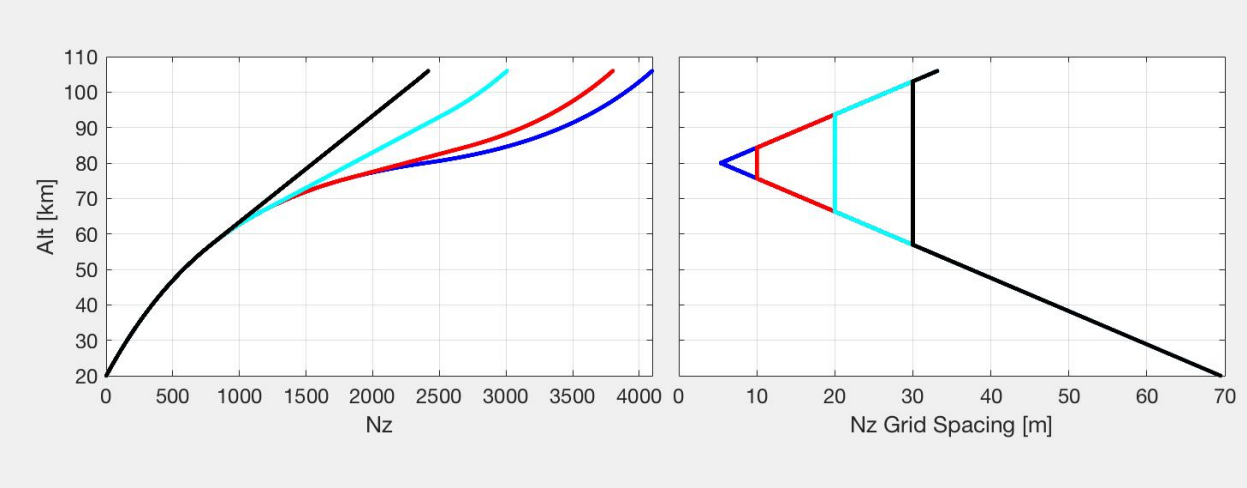

Figure 6.2: Vertical grid stretching mechanism used for Study 3, with region of fixed minimum grid spacing about 80 km where FS is applied. The mesh above and below the fixed grid spacing region is identical to the parameters used in Study 1.

6.6 Initial Testing and Validation

A number of initial test cases were run to refine the environmental parameters to approximate observed GW-FS interactions. The initial target was to reproduce a characteristic chain of KH billows forming on the upper crest of a GW as it enhances a local shear layer. This was first achieved for a horizontally and vertically localized GW in a deep domain (Figure 6.3a) and then shown to be roughly identical in a λ_x-width domain with a uniform GW packet in the horizontal (Figure 6.3b). The λ_x-width domain showed comparable scales and amplitudes of GW-induced structures and temperature evolutions occurring at roughly the same times, enabling the simulation to characterize the same interaction with reduced

computational resources.

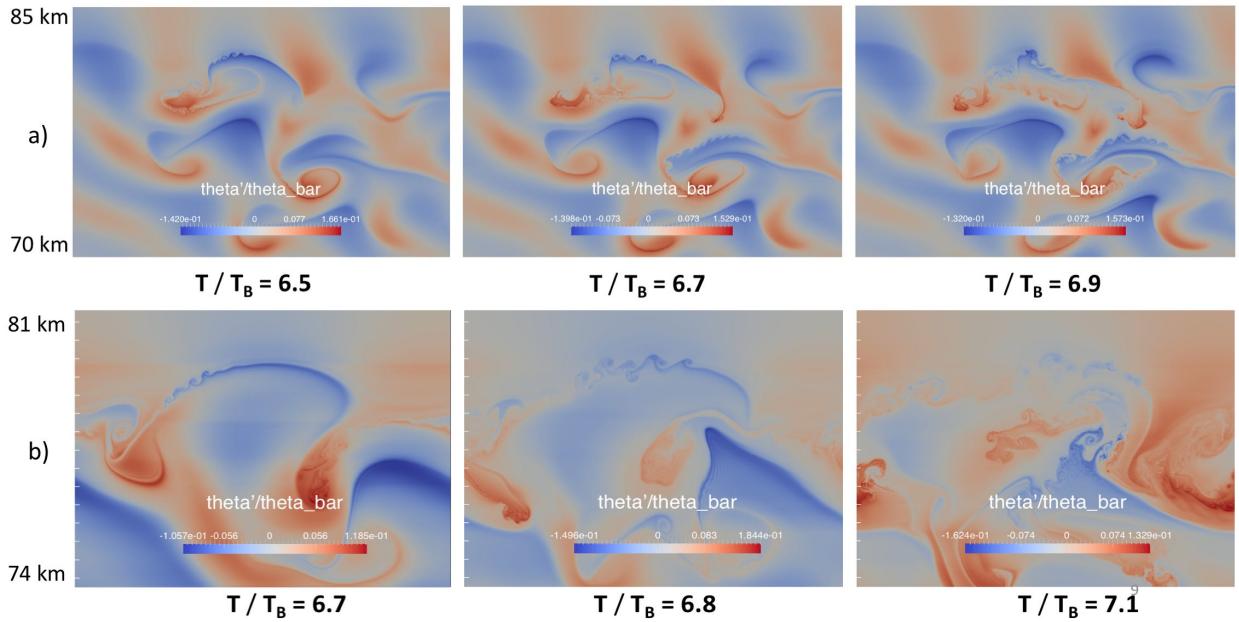

Figure 6.3: KHI and secondary instabilities on the upper crest of a GW produced with FV code simulation runs with (a) a horizontally localized GW packet in a wide domain and (b) a horizontally uniform GW packet in a periodic domain. The results are adequately similar to move forward with the narrower periodic domain for future studies.

6.7 Summary

The anelastic finite volume code is a suitable simulation architecture to probe the dynamics of GW-FS interactions in and around the MLT. For this application, we highlight its ability to 1) Capture nonlinear dynamics, including wave contributions to the mean flow evolution; 2) Scale density with altitude to enable realistic GW amplitude evolution; 3) Characterize GW filtering and transmission through turning layers, unlike ray-tracing routines; and 4) Enable deep atmospheric simulations with sufficient resolution to characterize instabilities through the onset of turbulence. Initial testing validates the code's ability to reproduce observable phenomena, paving the way for use in the studies described hereafter.

Chapter 7

Gravity Wave Propagation through Isolated Fine Structures in the MLT

This Chapter presents a numerical study of GW packets propagating through isolated layers of enhanced shear and/or stability and identifies the influences of different layer characteristics on the overall flow evolution. The purpose of this numerical analysis is to demonstrate the significant impact of fine structures on GW propagation and dissipation, instability dynamics, and the changes to the background wind and stratification. The Chapter first presents the evolution of a GW propagating through uniform wind and stability to establish a baseline set of GW and environmental metrics. The results then demonstrate how the inclusion of fine structures in the wind and stability profiles yields a wide array of responses, indicating how specific features in the vorticities (including baroclinic vorticity contributions), initial instability evolutions, and 3D turbulence onsets define the times and locations of induced instabilities and produce distinctive, lasting features in the background winds.

The Chapter is organized as follows: The physical parameters employed in this study are defined in Section 7.1. Section 7.2 presents simulation results from nonlinear GW propagation through a uniform background, providing a baseline case for comparison with cases including FS. The effects of GW propagation through FS layers are discussed in Section 7.3. Section 7.4 discusses how these results build on previous findings, and a summary of the results is given in Section 7.5.

7.1 Parameter Definitions

The model domain extends 20 km (one GW λ_x) in the streamwise (x) direction, 1 km in the spanwise (y) direction, and from 20-105 km in altitude (z). The domain employs periodic horizontal boundary conditions and a 15 km sponge layer at the top of the vertical domain, capping the useable domain at $z = 90\ km$. The code is executed on Department of Defense high performance supercomputers with a $(Nx, Ny, Nz) = (2048, 64, 4096)$ grid, having streamwise and spanwise grid resolution of $(\Delta x, \Delta y) = (10\ m, 16\ m)$ and a power-law stretched vertical mesh with $(\Delta z_{max}, \Delta z_{min}) = (70\ m, 5\ m)$. The vertical grid employs a stretch factor of $\gamma = 0.001$ symmetrically about the region of highest resolution at $z = 80\ km$.

All simulations are initialized with a GW described by $(\lambda_z, \lambda_x, \omega_0, c_0) = (10\ km, 20\ km, N/2, -30 m/s)$ with a Gaussian amplitude distribution centered at 50 km with a full width at half maximum depth of 10 km. The initial GW amplitude is set to satisfy $|u'| \approx U_0$ when the center of the packet reaches 80 km, and $U_0 = -c_0$ sets the initial observed horizontal phase speed at 0. Uniform wind and stability are applied to the background profiles as $(U_0 = U_1 = -c_0,\ N_0^2 = N_1^2 = 0.0004 s^{-2})$ in Equations 6.9 and 6.10. FS included in the background wind and stability profiles for each case is shown in Table 7.1 and Figure 7.1, with all FS cases having $(z_0,\ d) = (80\ km,\ 125\ m)$. Cases 3 to 4 include positive $\overline{U}_z$ FS, while Cases 5 to 6 include negative $\overline{U}_z$ FS. Cases 2, 4, and 6 also include positive N^2 FS. Cases 3 and 5 have a minimum Ri of 0.25 (neutrally stable), and Cases 4 and 6 have a minimum Ri of 0.5 (stable).

Table 7.1: Background Parameters for Each Case

Case	$U_0\ [ms^{-1}]$	$U_1\ [ms^{-1}]$	$N_0^2\ [s^{-2}]$	$N_1^2\ [s^{-2}]$
1	30	30	0.0004	0.0004
2	30	30	0.0004	0.0008
3	30	40	0.0004	0.0004
4	30	40	0.0004	0.0008
5	30	20	0.0004	0.0004
6	30	20	0.0004	0.0008

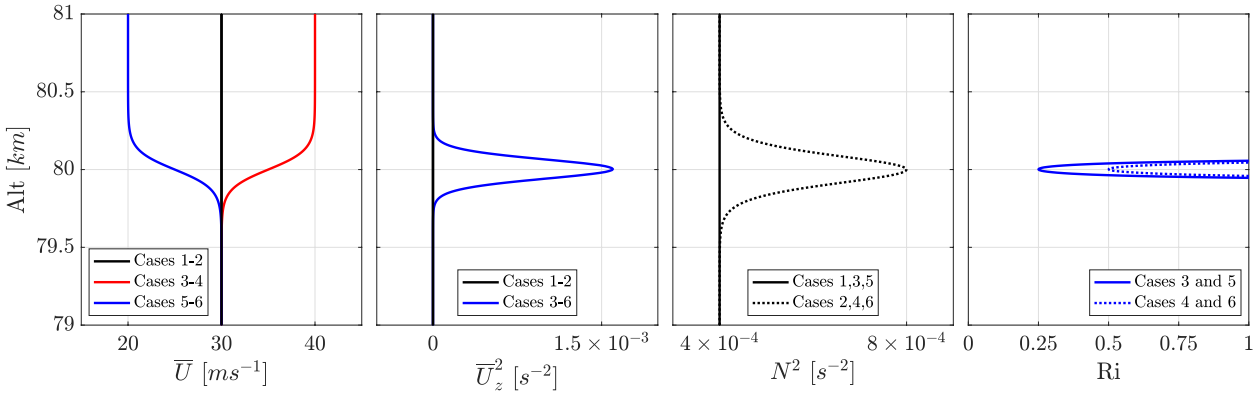

Figure 7.1: Background profiles used to initialize simulations for Cases 1 to 6.

The Reynolds number (Re) is calculated from the GW length scale as

$$Re = \frac{\lambda_z^2}{T_B \nu} \quad . \tag{7.1}$$

We assume a turbulent viscosity of $\nu_{turb} = 3\nu$ based on estimates of an elevated effective viscosity due to pre-existing turbulence (Baumgarten and Fritts, 2014; Fritts et al., 2014a; Hecht et al., 2014; Fritts et al., 2014c; Hecht et al., 2018), where ν is the true viscosity $\sim 1.5{\times}10^{-5}\ m^2 s^{-1}$ at ground level and $\nu_{turb} \sim 2.8\ m^2 s^{-1}$ at 80 km. For GW with $\lambda_z = 10\ km$, this results in $Re \approx 10^5$ where fine structures arise accompanying flow instabilities.

Assuming a representative $\epsilon \approx 0.5\ m^2 s^{-3}$ as in recent GW breaking simulations (see e.g., Fritts et al., 2018a,b, 2017, 2009a), the expected inner scale of turbulence for density fluctuations can be approximated as

$$l_0 = 7.4\eta = 7.4\left(\nu_{turb}^3/\epsilon\right)^{\frac{1}{4}} \approx 20\ m \tag{7.2}$$

(Hill and Clifford, 1978). This value falls within the range $l_0 \approx 10 - 20\ m$ predicted for the mesopause by Hocking (1985) and gives a corresponding Kolmogorov length scale of $\eta \approx 2.6\ m$. Because the resulting ratio of model resolution to η, $R_{x,z} = (\Delta x, \Delta z)/\eta \approx 2 - 4$, is larger than the desired $R \approx 1.5 - 2.1$ for DNS (Moin and Mahesh, 1998; Pope, 2000), LES is employed in all simulations to ensure proper energetics.

7.2 Case 1: Nonlinear GW Propagation through a Uniform Background

The initial evolution of the u' and w' GW fields is shown in Figure 7.2. Red and blue contours indicate positive and negative values, and this colormap is used for the remainder of the figures. SA occurs as the GW resides in a region where the divergence of its momentum flux accelerates the mean flow. Nonlinear SA influences become apparent when $|u'|$ surpasses U_0 at $\sim 2.5T_B$, increasing phase speed above the direction of GW propagation at the leading edge of the packet. The effects of SA quickly dissociate the phase alignment of the wind perturbations, sending ripples through the domain that modulate the associated fluxes and induced mean wind. The localized SA onset creates an abrupt shift in the GW vertical wavelength, visible at $\sim 3.7T_B$, as λ_z increases in the region of accelerated c and compresses the GW below. The distinct behavior at the altitude of the initial λ_z disturbance is most pronounced in w' fields, where the phase lines appear to rotate and separate the negative phase at $\sim 6.7T_B$. The phase lines at the altitude of the initial λ_z disturbance fully detach at $\sim 7.3T_B$ as a visible modulation progresses down through the w' domain whereas u' phase structure remains relatively uniform.

Figure 7.3 shows the vertical fluxes of vertical momentum and horizontal momentum, $\langle w'^2 \rangle$ and -$\langle u'w' \rangle$, divided by density and plotted at log_{10} scales. $\langle\rangle$ indicates streamwise averaging. The dissociated phase alignment of u' and w' produces a modulation in the GW fluxes from $\sim$ 4 to $8T_B$. The maximum $\langle w'^2 \rangle$ occurs at the altitude of the initial λ_z disturbance above 80 km at $\sim 4T_B$, after which point regions of higher vertical flux progress downward through the domain following the phase behavior observed in the w' fields. This feature does not occur in the horizontal momentum flux (not shown), but the vertical flux of vertical momentum takes on the characteristic ripple from $\langle w'^2 \rangle$.

Figure 7.4 shows the induced mean flow from the GW, given by Equation 2.14. The initial $\Delta\overline{U}$ envelope roughly matches the initial Gaussian GW amplitude distribution, but by $\sim 3.7T_B$ the induced wind is larger at the top of the packet as SA onset enhances the

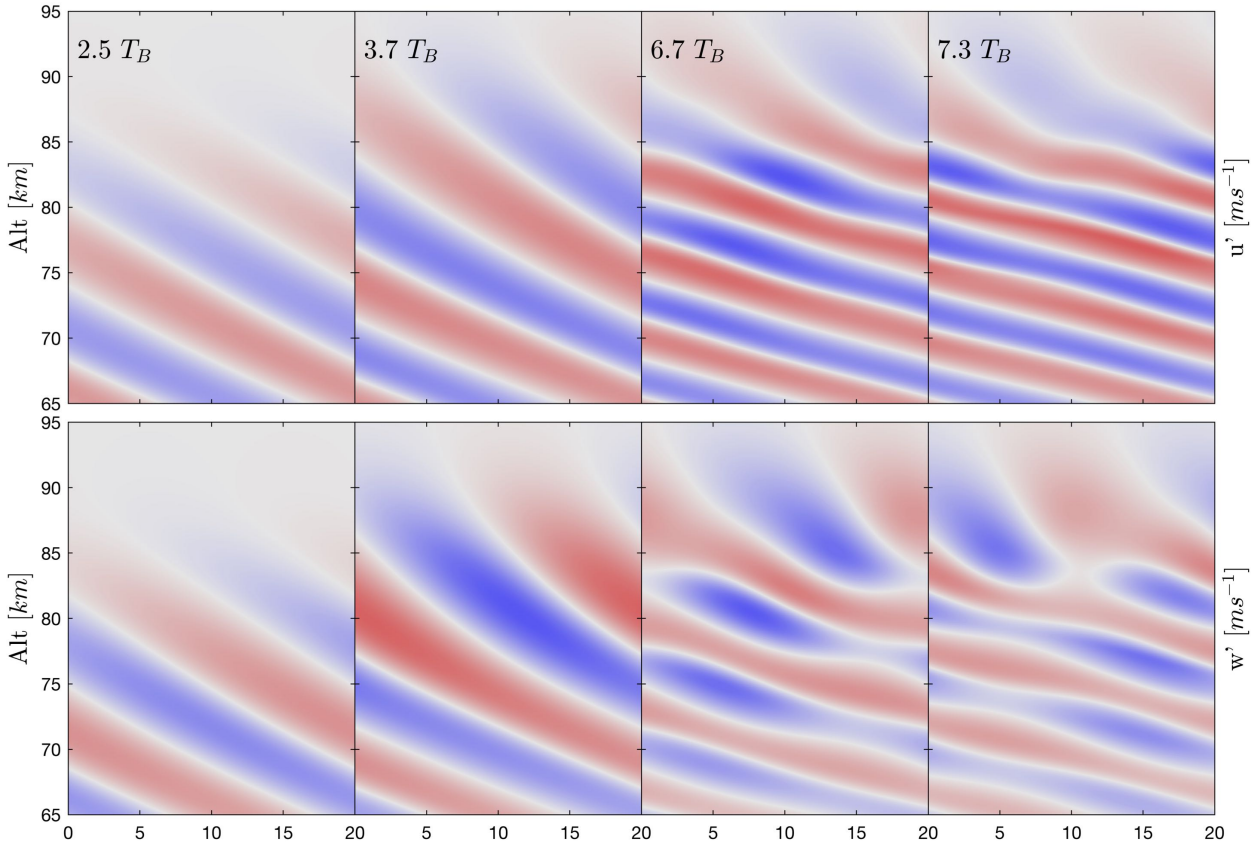

Figure 7.2: GW u' and w' perturbations in the x-z (streamwise-vertical) plane for Case 1 at four different times. Around $\sim 3.7T_B$, the relative phase structures and amplitudes of u' and w' vary with altitude because of the changing environment, as SA effects produce a rapid shift in λ_z near 85 km.

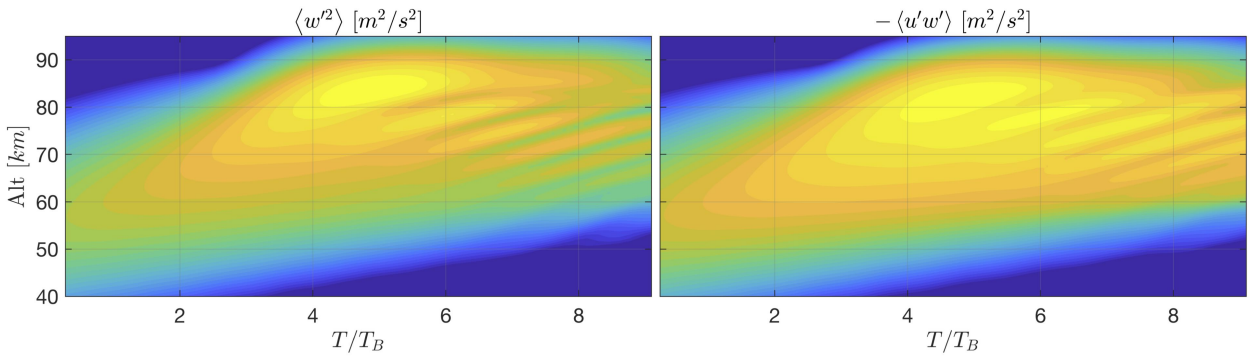

Figure 7.3: Horizontally averaged vertical fluxes of vertical momentum (left) and horizontal momentum (right) for Case 1, divided by density. The modulated vertical flux of vertical momentum produces a corresponding modulation in the vertical flux of horizontal momentum.

local momentum flux. The modulations in $\langle u'w' \rangle$ produce corresponding ripples at $\sim 6.7T_B$,

which then diminish to a more uniform $\Delta\overline{U}$ slope at $\sim 10T_B$ with the maximum $\Delta\overline{U}$ just over $2\overline{U}_0$. $\Delta\overline{U}/\Delta\overline{U}_{max}$ in the right panel provides a clearer comparison of the amplitude envelope of $\Delta\overline{U}$, which decreases slightly in vertical extent over time.

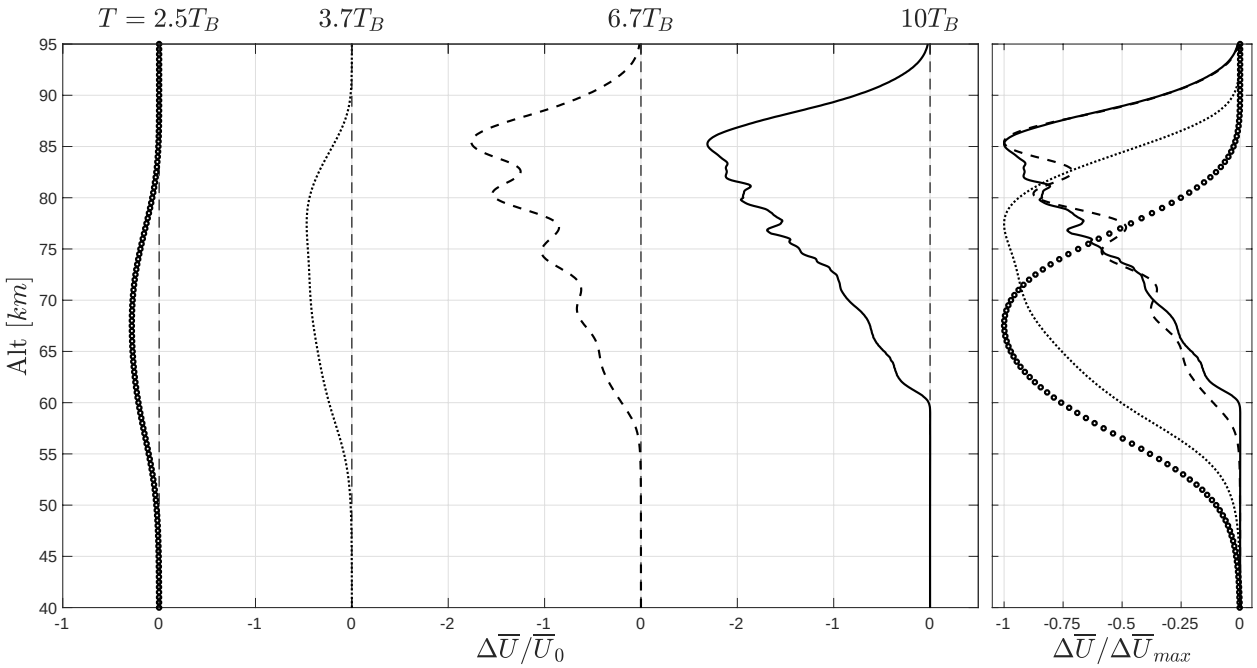

Figure 7.4: Normalized $\Delta\overline{U}$ evolution for Case 1, showing initial vertically symmetric amplitude distribution of the packet, higher $\Delta\overline{U}$ at the top of the packet as GW amplitude increases with altitude, and oscillations corresponding to the modulation of w', which diminish by $10T_B$. $\Delta\overline{U}/\Delta\overline{U}_{max}$ (right panel) emphasizes the depth of the induced wind region, which does not change significantly with time.

The rippling effect of the vertical flux and its associated changes to the background horizontal winds have been documented in several recent studies of nonlinear GW propagation and attributed to several potential sources. Dosser and Sutherland (2011a) observed modulated wind profiles as a consequence of modulational instability, which occurs for GWs that satisfy

$$|m| < \sqrt{\frac{k^2 + \frac{1}{4H^2}}{2}} \tag{7.3}$$

However, Dosser and Sutherland (2011a) also observed modulated GW amplitude profiles late in the evolution of modulationally stable GWs for which there was no corresponding modulation in the induced wind. Fritts et al. (2015) observed modulations in altitude of

$\Delta\overline{U}(z)$ and $\rho\langle u'w'\rangle$ that decay with time for modulationally stable GW packets undergoing SA, suggesting that modulated wind profiles may occur as a consequence of any GW packet undergoing SA. They further found that higher ω_0 reduces the depth of the modulation. Snively (2017) observed a similar "layering of fluxes" in the vertical momentum flux for GW packets that experience SA, attributing the feature to partial reflection of the GW packets. In the case of reflection, Snively argues, the horizontal fluxes of left- and right-going reflected GWs cancel out, yielding no net change to $\langle u'^2\rangle$ but resulting in harmonic vertical forcing that can generate acoustic GWs. While the source of the ripple effect is still a subject of debate, the occurrence of GW-modulated wind profiles is well-documented and should not be viewed as an anomaly.

7.3 Cases 2 to 6: Nonlinear GW Propagation through Shear and Stability

The instability evolutions for positive shear and stability FS cases (2 to 4) are described in Section 7.3.1, with the negative shear FS cases (5 and 6) evaluated in Section 7.3.2. The large scale implications of all 6 cases are discussed in Section 7.3.3, including an overview of turbulent transition and background flow implications.

7.3.1 Cases 2 to 4: Initial Instability Evolution

The vortical evolution of the flow reveals distinguishing features that develop for each FS case. Figure 7.5 shows the initial FS layer evolution represented by the spanwise component of vorticity, $\zeta_y = \frac{\partial u}{\partial z} - \frac{\partial w}{\partial x}$, the rotational tendency in the streamwise-vertical (x-z) plane. At early stages, the flow is largely 2D and ζ_y is the dominant vorticity component. Positive (negative) ζ_y denotes (counter)clockwise rotational tendencies or strong positive (negative) shear in the presence of small $\frac{\partial w}{\partial x}$. The N^2 FS in Case 2 generates no initial ζ_y, while the positive $\overline{U}_z$ FS in Cases 3 and 4 produces a sheet of positive ζ_y in the initial condition. At $\sim 5.3T_B$, the initial FS warps and kinks as the GW propagates upwind with enhanced c. The rotation of the initial N^2 FS compresses the local vertical GW scales and enhances $\frac{\partial\theta}{\partial z}$,

creating local θ' maxima that generate positive (negative) ζ_y as the layer is advected above (below) its initial altitude (see Panel 1 for Case 2 and discussion of baroclinic sources and sinks in the following paragraph). The advecting rotation of the initial $\overline{U}_z$ FS transforms positive $\frac{\partial u}{\partial z}$ to negative $\frac{\partial w}{\partial x}$, thus retaining its ζ_y sign and magnitude (see Panel 1 for Case 3). In Case 4, where both of these effects are present, positive ζ_y from the initial $\overline{U}_z$ FS is enhanced by the N^2 FS as it advects upward and reduced by the N^2 FS as it advects downward, the net effect largely identical to Case 3 but with a stronger clockwise rotational tendency above 80 km. Enhanced negative $\frac{\partial u}{\partial z}$ below each initial FS produces a layer of intensified negative ζ_y at 78 km (see Cases 2 to 4 from 6 to 7.3T_B), while the topsides of the initial positive $\overline{U}_z$ layers in Cases 3 and 4 also continue to intensify as the local positive ζ_y increases.

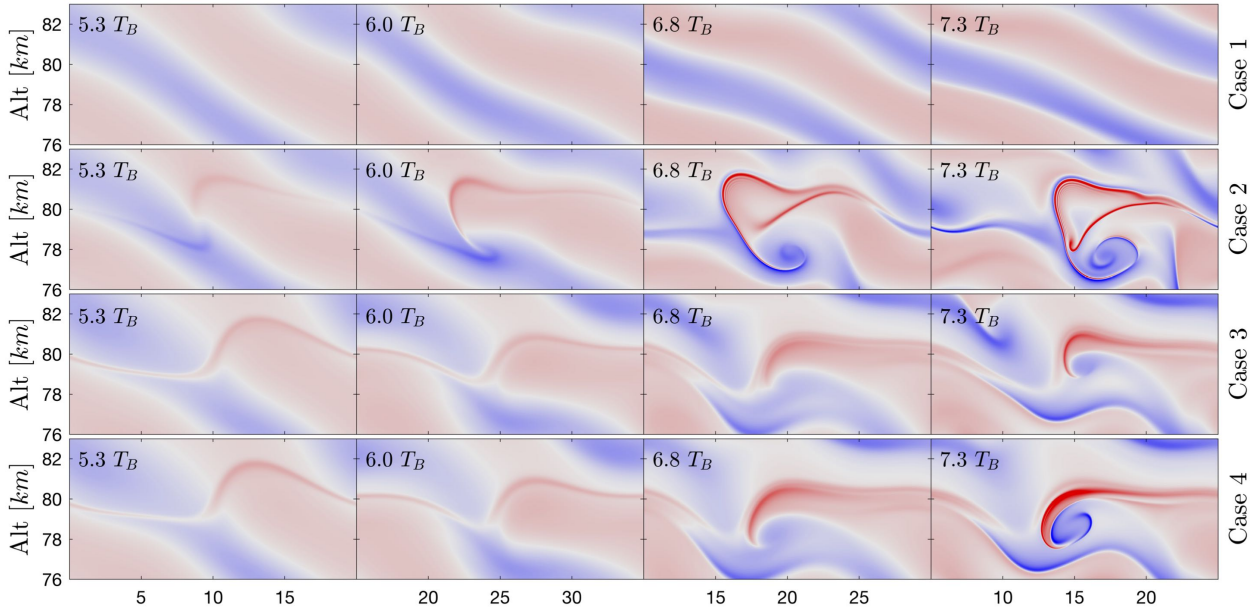

Figure 7.5: ζ_y fields at 4 different times for Cases 1 to 4, with a translating horizontal domain centered on the instability structures to emphasize distinctions among the initial instabilities as they evolve. Unique ζ_y behaviors caused by $\overline{U}_z$ and N^2 FS are apparent in Cases 2 and 3, respectively, and the evolution in Case 4 is an approximate superposition of the dominant behaviors in these two cases with both types of FS present. Cases 2 and 4 have higher ζ_y amplitudes than Case 3 after the initial FS rotates.

Baroclinic sources and sinks are important ζ_y sources in Case 2 and Case 4 as the

rotating N^2 FS produces horizontal temperature gradients that misalign local pressure and density gradients. Figure 7.6 shows the evolution of the baroclinic source term (see Equation 2.25) corresponding to Figure 7.5. As the N^2 FS rotates towards $\frac{\partial \theta}{\partial z} \sim 0$ in Cases 2 and 4, enhanced horizontal θ' gradients rapidly intensify the baroclinic source term from 6 to $7.3T_B$ and generate higher amplitudes on the corresponding vertical positive ζ_y sheets - baroclinic sources in Case 2 have twice the amplitude of Cases 3 and 4 at $6T_B$, and baroclinic sources at $7.3T_B$ are $\sim$ one order of magnitude larger in Cases 2 and 4 than Case 3. In the absence of initial positive $\overline{U}_z$, the vertical positive ζ_y sheet in Case 2 expands downward into the intensifying negative $\frac{\partial u}{\partial z}$ region (i.e. the region of negative ζ_y visible in Figure 7.5 at $6.8T_B$), growing larger than the corresponding roll-up structures in Cases 3 and 4. While all 3 FS cases develop instabilities before $10T_B$, the enhanced baroclinity in Cases 2 and 4 further accelerates the instability onsets relative to Case 3 and yields more rapid progressions to smaller scale dynamics. An evaluation of the initial instability evolution follows for each FS case.

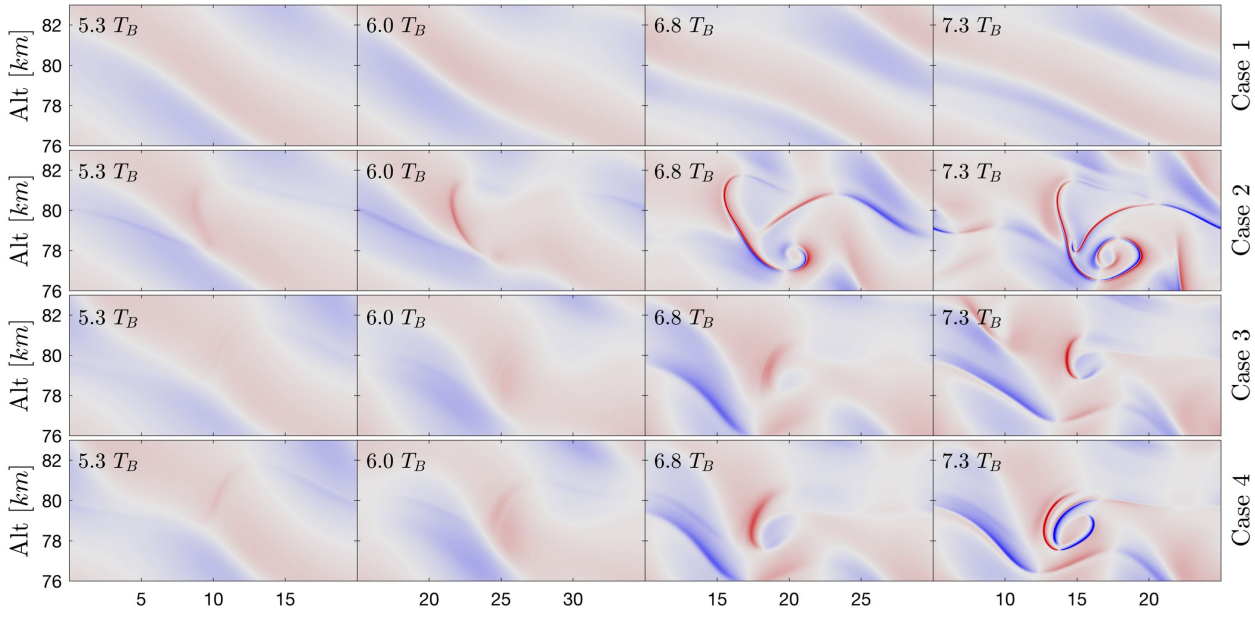

Figure 7.6: $\frac{1}{\rho^2}\left(\nabla\rho \times \nabla P\right)_y$ fields at 4 different times for Cases 1 to 4, with translating horizontal domain as in Figure 7.5. Baroclinic sources are stronger in Cases 2 and 4, where the rotation of the initial N^2 FS produces large horizontal θ' gradients.

The initial instability rollup in w', θ', ζ_y, and $\frac{1}{\rho^2}\left(\nabla\rho \times \nabla p\right)_y$ is shown for Cases 2 to 4 in Figures 7.7 to 7.9, respectively, at 1 minute increments. Viewing these fields side-by-side reveals how the evolution of each field impacts the other fields and helps to identify which dynamics, i.e., advection or baroclinic forcing, account for the different characteristics in each case. Important shared features in the initial instabilities include 1) initial vortical structures with scales $\approx \lambda_{z_0}/2$ comprised of opposing, intensified ζ_y sheets, with initial instabilities forming in regions of intensified $\frac{\partial u}{\partial z}$ that are visible in the ζ_y fields at the top (positive) or bottom (negative) of the structure; 2) rapid intensification of baroclinity leading to the initial overturning motion, with opposite sign baroclinic sheets occurring for local horizontal θ' extrema that in turn drive the thinning and intensification of the corresponding ζ_y sheets; 3) strong buildup of $\frac{\partial w}{\partial x}$ that enhances regional ζ_y on the interface of horizontally rotated w' phase lines; and 4) enhanced background $\frac{\partial u}{\partial z}$ surrounding the most intensified ζ_y sheets that instigate the initial vortices. Notable distinctions among the different cases include 1) initial vortex formation at the bottom of the structure in Case 2 with counterclockwise rotation (negative ζ_y), in a region of negative $\frac{\partial u}{\partial z}$, vs. initial vortex formation in the top of the vortical structure in Cases 3 and 4 with clockwise rotation (positive ζ_y), in regions of positive $\frac{\partial u}{\partial z}$; 2) earlier vortex formation in Cases 2 and 4 relative to Case 3, largely driven by the increased baroclinity in their initial N^2 FS; and 3) larger vertical scales of the initial vortical structure of Case 2 in the absence of initial $\overline{U}_z$.

Figures 7.10 to 7.12 show the $\zeta_x = \frac{\partial w}{\partial y} - \frac{\partial v}{\partial z}$ and $\zeta_y = \frac{\partial u}{\partial z} - \frac{\partial w}{\partial x}$ components of vorticity in a common volume at the time of the initial streamwise vortices for Cases 2 to 4. As with ζ_y, ζ_x is the streamwise vorticity component which describes clockwise (positive) and counterclockwise (negative) rotational tendencies in the spanwise-vertical (y-z) plane. ζ_y is shown on the x-z (streamwise-vertical) slice, and ζ_x is shown on several y-z (spanwise-vertical) slices to highlight the three-dimensional nature of the transition to turbulence. Several important features are apparent when viewing the intersecting ζ_x and ζ_y slices: 1) The initial spanwise wavenumber instability comprises streamwise-aligned counter-rotating

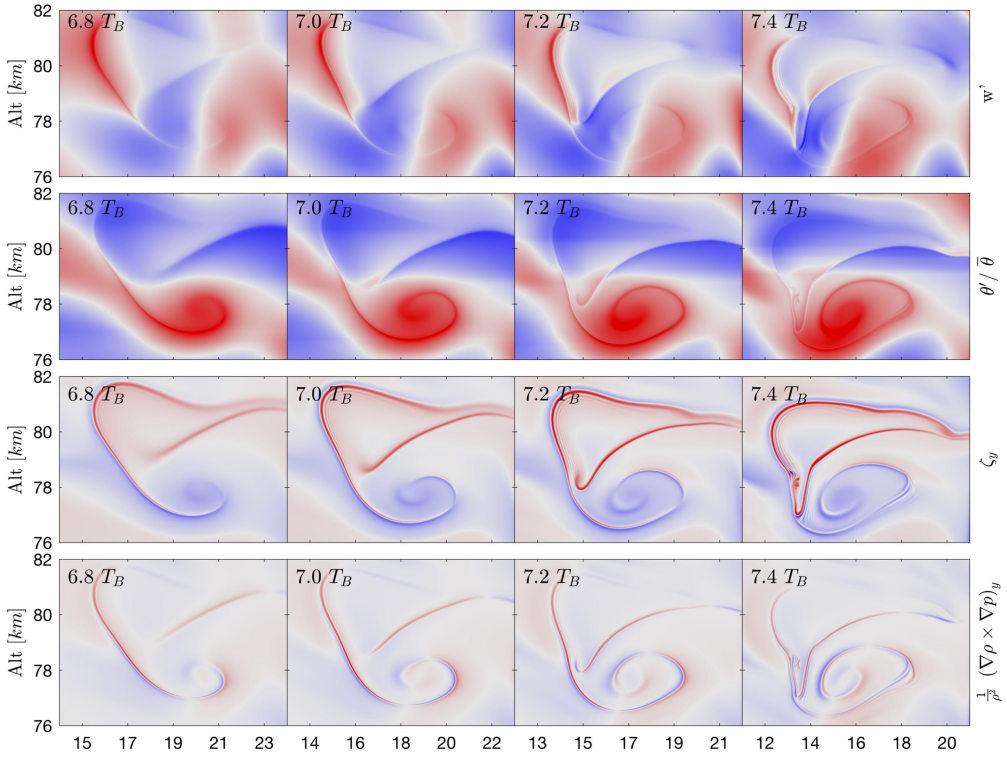

Figure 7.7: w', $\theta'/\overline{\theta}$, ζ_y, and $\frac{1}{\rho^2}\left(\nabla\rho \times \nabla P\right)_y$ fields at 4 different times for Case 2. The initial instability develops in the region of negative ζ_y at the bottom of the main vortical structure, producing rotation earlier and over a larger vertical extent than Cases 3 and 4.

vortices, as seen in many previous similar flows, and for which the primary energy sources appear to be shear and buoyancy. 2) Spanwise ζ_x vortices precede the evolution of secondary 2D instabilities. 3) ζ_x rotational tendencies are most significantly enhanced between strong, opposing ζ_y sheets where stability is a minimum. 4) Spanwise vortex pair formation on the edges of the sheet of high shear in the initial vortices suggests that the instabilities are most similar to KHI in character, particularly for Case 4. 5) Instability vortical structures are well-resolved, giving confidence in the the accuracy of the GW and primary instability features and background flow evolutions that occur as a consequence of the multi-scale evolution in each case.

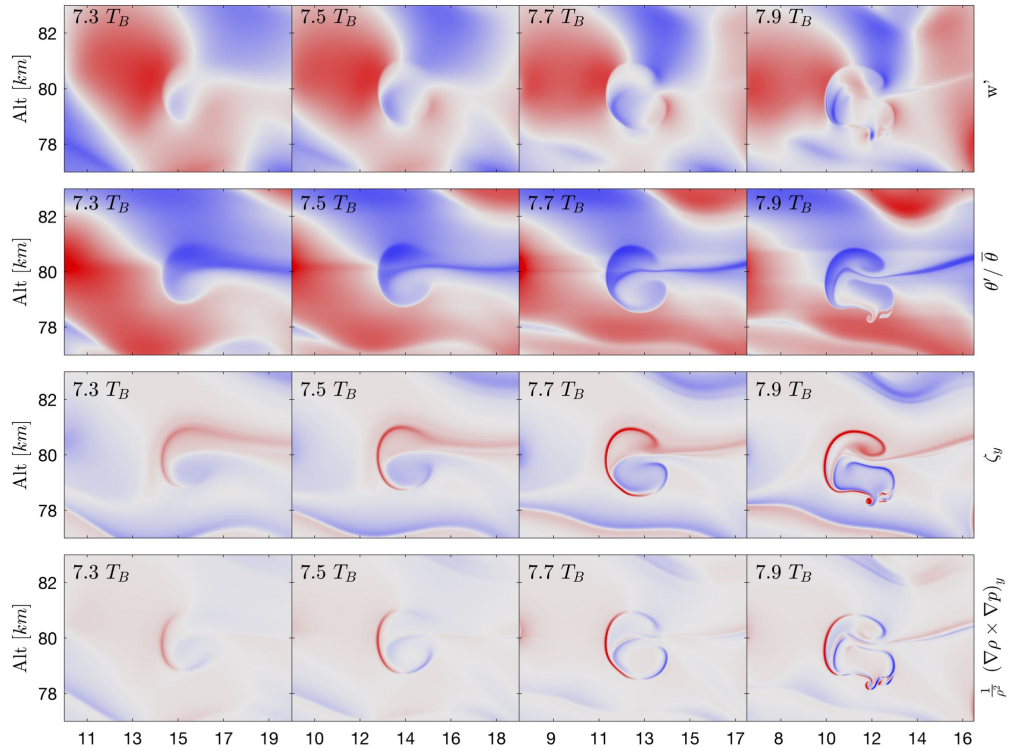

Figure 7.8: As in Figure 7.7 for Case 3. The initial instability develops in the region of positive ζ_y at the top of the main vortical structure at a later time than Cases 2 and 4.

7.3.2 Cases 5 and 6: Initial Instability Evolution with Negative Shear

Cases 5 and 6 reverse the shear direction of Cases 3 and 4, respectively, such that the FS decreases the background wind while imposing the same mean Ri. The reduction in $\overline{U}$ above 80 km reduces, rather than increases, the GW vertical group velocity, intensifying the dynamics that occur at and below the FS and diminishing the impact above. The early stages of nonlinear GW evolution are shown in the $\theta'/\overline{\theta}$ and $\frac{1}{\rho^2}\left(\nabla\rho\times\nabla P\right)_y$ fields in Figures 7.13 and 7.14, respectively. Cases 5 and 6 differ from Cases 3 and 4 in that: 1) Upwind c increases more rapidly across the enhanced shear layer, creating an earlier rollup of the vorticity structures at 80 km and earlier evolution of 2D and 3D flow instabilities. 2) The initial $\overline{U}_z$ layer has negative ζ_y and counterclockwise rotational tendency, such that the N^2 FS in Case 6 enhances, rather than offsets, the negative ζ_y sheet as it advects downward,

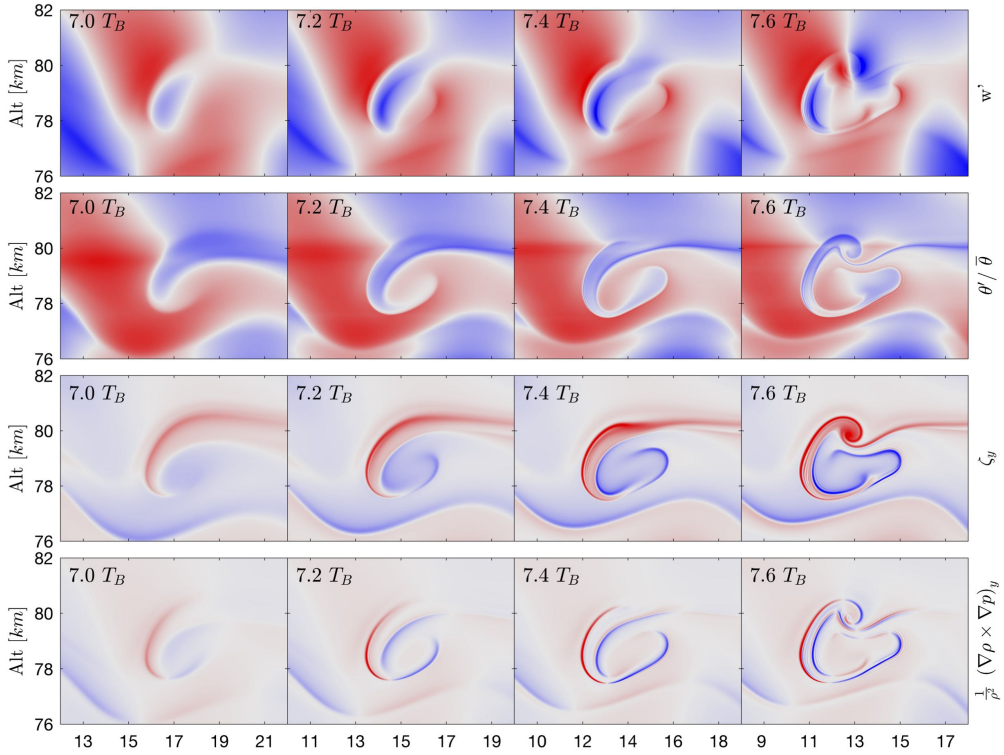

Figure 7.9: As in Figure 7.7 for Case 4. The initial instability develops in the region of positive ζ_y at the top of the main vortical structure as in Case 3, but it produces rotation earlier than Case 3 following the initial instability in Case 2.

accelerating the evolution of instabilities relative to Case 5. 3) Strong baroclinity occurs at earlier times, with and without an initial N^2 perturbation, as the rotating FS generates prominent horizontal θ gradients and corresponding baroclinic tendencies. Since FS advects upwind with the enhanced GW c in all FS cases, the baroclinity enhances positive ζ_y at the top of the vortical structure as in Cases 2 and 4. Relative to Case 5, the inclusion of N^2 FS in Case 6 does not significantly alter the morphology of the vortical evolution, owing to negative $\overline{U}_z$ and N^2 FS having similar ζ_y behavior above and below the layer.

The roll-ups of the initial instability structures are shown for Cases 5 and 6 in Figures 7.15 and 7.16, respectively. As in Figures 7.7 to 7.9, the evolutions are shown at 1 minute increments for the vertical wind, potential temperature, spanwise vorticity, and baroclinity. The negative $\overline{U}_z$ cases are distinct from Cases 2 to 4 in that 1) they produce initial in-

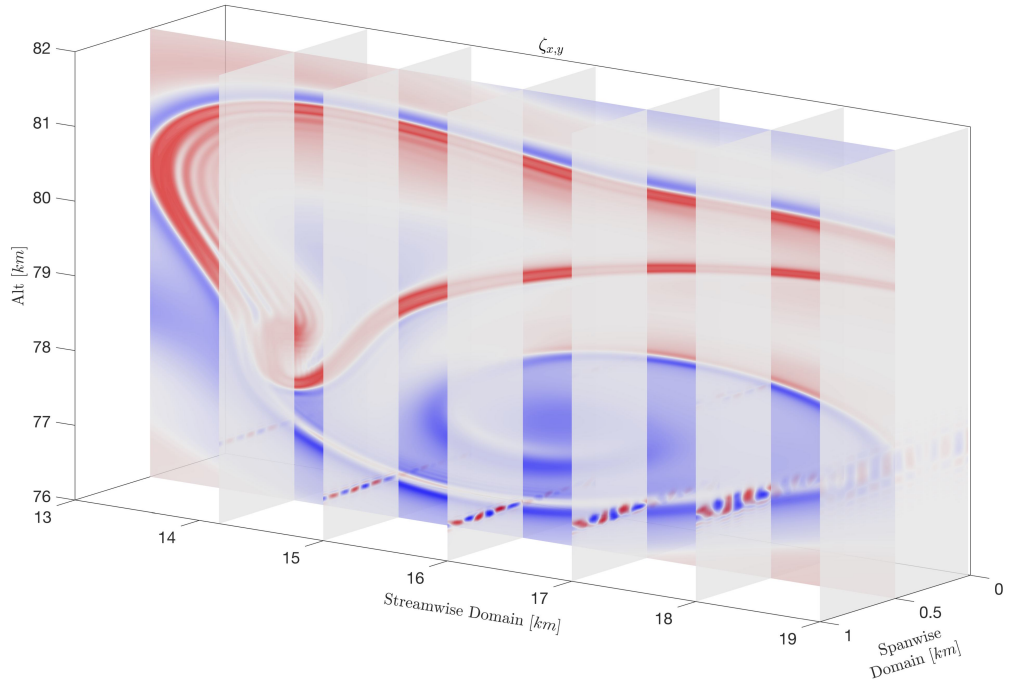

Figure 7.10: ζ_x and ζ_y fields, shown on intersecting slices through a common volume, for the initial instability onset in Case 2 at $7.3T_B$. ζ_y is shown on the x-z (streamwise-vertical) slice, and ζ_x is shown on several y-z (spanwise-vertical) slices. Vorticity amplitudes are magnified to emphasize the structure of the main ζ_x and ζ_y sheets, and the opacity of each slice is determined locally by the vorticity amplitude. The initial spanwise instability occurs as pairs of counter-rotating ζ_x vortices form between strong, opposing ζ_y sheets in locations of minimum stability. The vorticity layering adjacent to the main vertically-oriented ζ_y sheet develops as a consequence of the adjacent baroclinic sheets, caused by the tilted surfaces with opposing rotational tendencies that develop around the dominant ζ_y sheet. Vortical structures are well-resolved and give confidence in the accuracy of large-scale instability features and background characteristics induced by the flow.

stabilities 1 to $2T_B$ earlier, and 2) they have simultaneous vortex development on the top positive ζ_y sheet and the bottom negative ζ_y sheet. The negative ζ_y sheet is surrounded by a large negative $\frac{\partial u}{\partial z}$ buildup from the upward propagating GW, producing one large vortex of roughly the same scale as the initial vortices in Cases 2 to 4, whereas the top positive ζ_y sheet develops a chain of smaller vortices as the sheet flattens out. Baroclinic sheets accompany the dominant vertically aligned ζ_y features and again develop source/sink pairs about the strongest horizontal θ' gradients that intensify the vorticity to amplitudes $\sim$ one order of magnitude larger than Cases 2 to 4 from $\sim$ 4 to $6T_B$. The stronger baroclinity associated

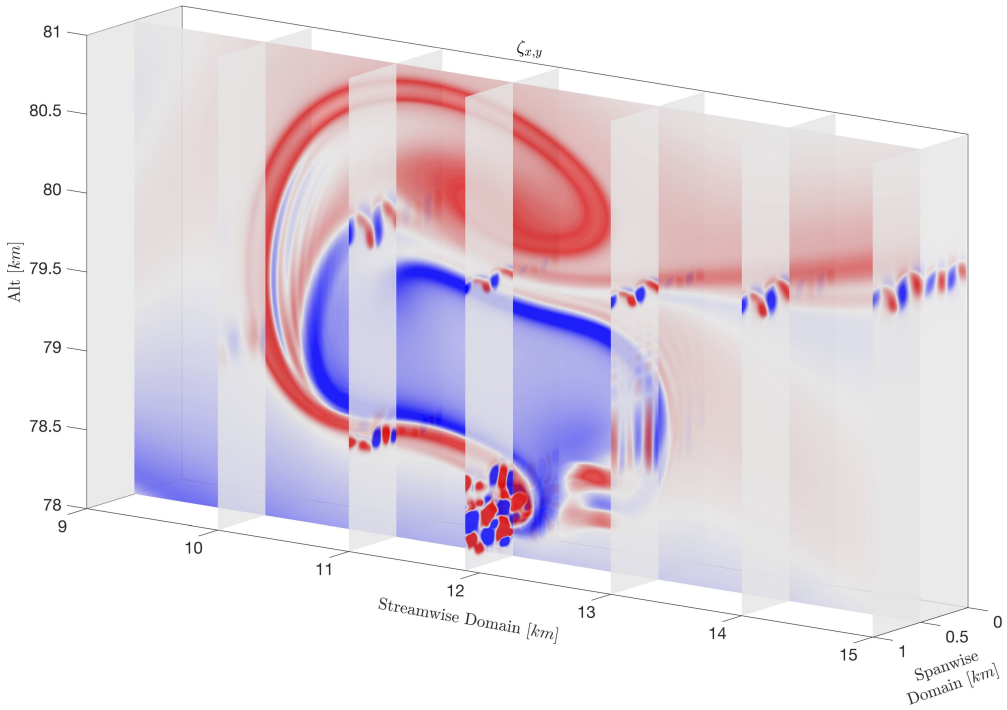

Figure 7.11: As in Figure 7.10 for Case 3 at $7.9T_B$.

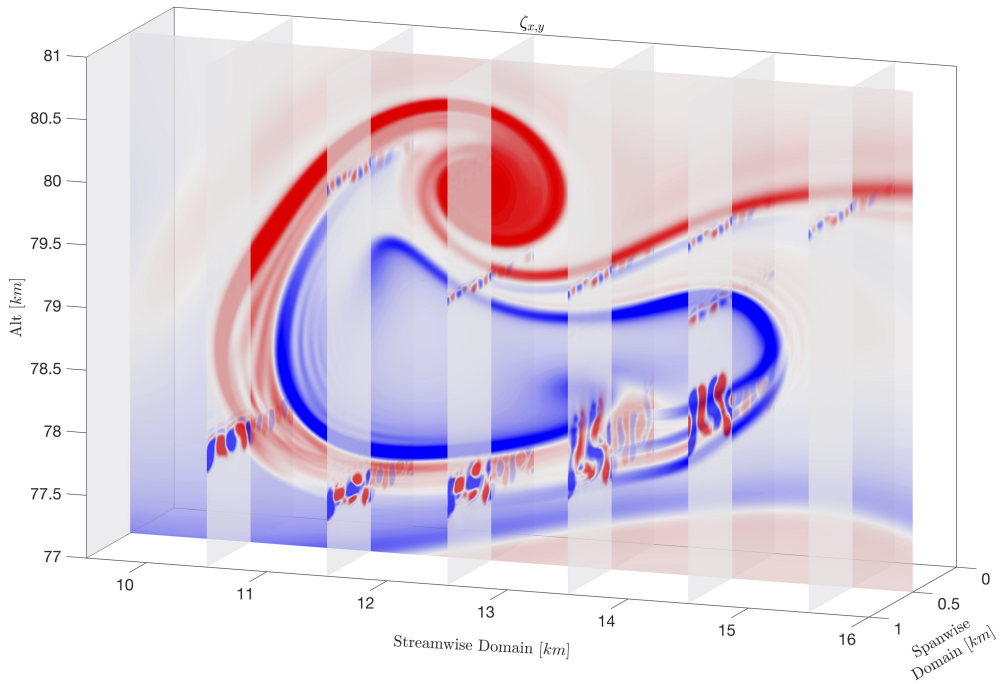

Figure 7.12: As in Figure 7.10 for Case 4 at $7.6T_B$.

with the N^2 FS in Case 6 accelerates vortex formation by $\sim 0.2T_B$ and generates additional

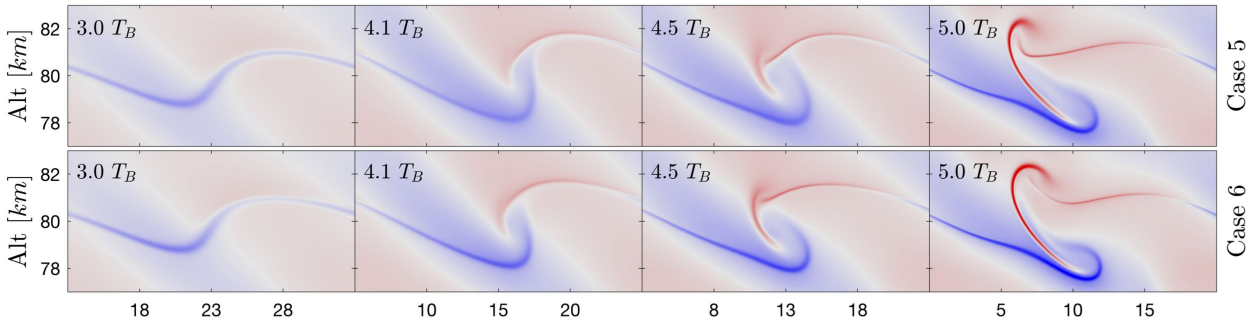

Figure 7.13: As in Figure 7.5 for Cases 5 and 6. The added N^2 FS in Case 6 has the same vortical tendencies as Case 5, producing higher peak vorticity without diminishing ζ_y amplitudes at the bottom of the vortical structure.

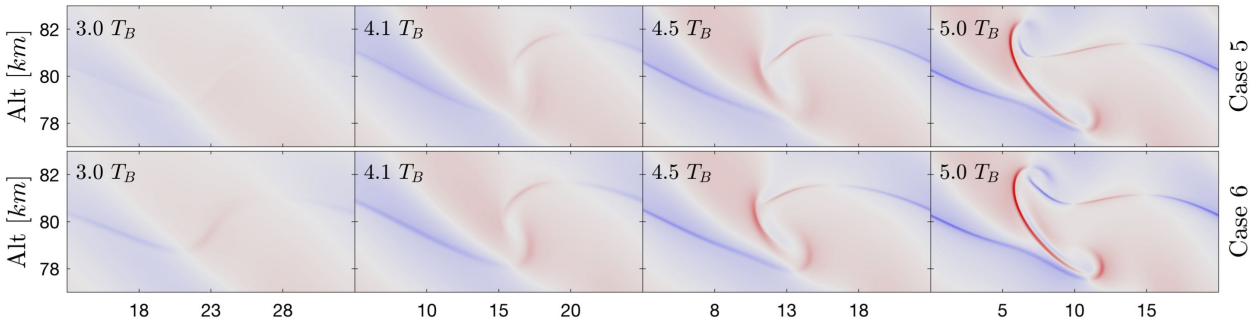

Figure 7.14: As in Figure 7.6 for Cases 5 and 6. The enhanced baroclinity supported by the N^2 layer in Case 6 sharpens the vertically-oriented ζ_y features and promotes earlier instability onset.

vortices on the positive ζ_y sheet.

Figures 7.17 and 7.18 show the ζ_x and ζ_y components of vorticity in a common volume at the time of the initial streamwise vortices for Cases 5 and 6. In both cases, spanwise ζ_x vortex pairs accompany the bottom negative ζ_y sheet and the vertically oriented region of the positive ζ_y sheet intensified by the baroclinity. That the spanwise vortex pairs are most well-formed on the original negative $\overline{U}_z$ sheet further support the notion that shear drives the turbulent transition. As with Cases 2 to 4, the spanwise vortex pairs are located at the interface of the strongest shear layers and their opposing ζ_y sheets. Case 6 has larger, more coherent spanwise vortical structures that give rise to more rapid progression to smaller spatial scales and the eventual turbulent cascade.

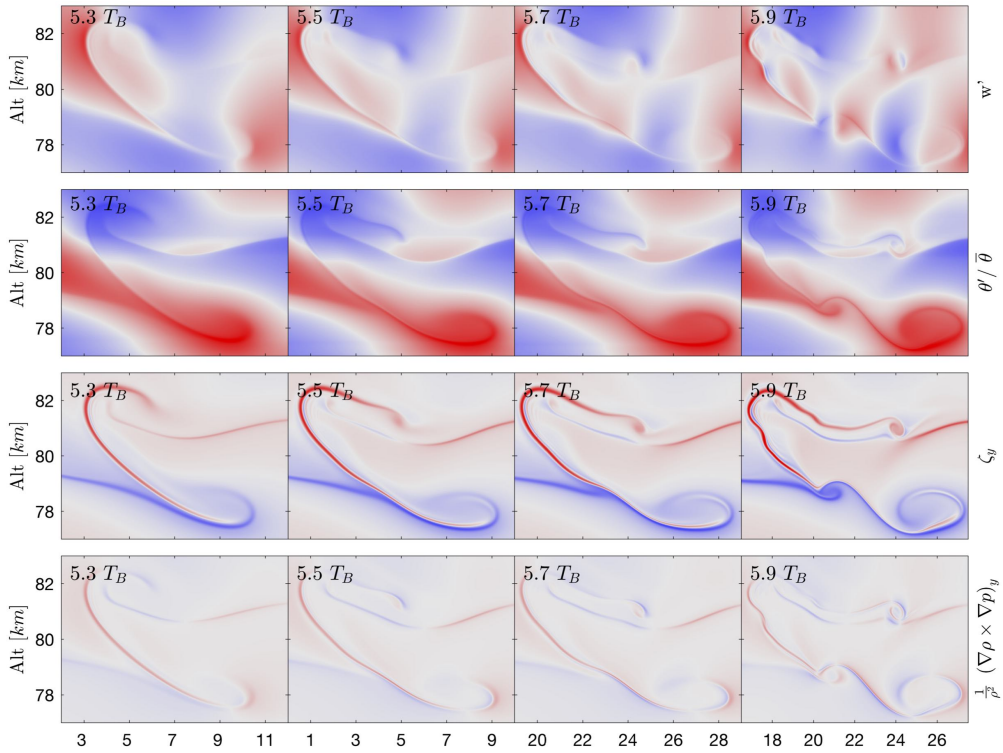

Figure 7.15: As in Figure 7.7 for Case 5. The initial instabilities develop simultaneously in the regions of positive (negative) ζ_y at the top (bottom) of the main vortical structure at earlier times than Cases 2 to 4.

7.3.3 Turbulence Evolution, Scale Progression, and Large-Scale Influences of Instability Dynamics

The development of the primary and secondary streamwise instability structures, and their eventual transition to fully-developed turbulence for all six cases discussed above, are presented in Figure 7.19, comprising the spanwise ζ_y fields and the associated $\Delta\overline{U}$ profiles (colored to match Figures 7.20 and 7.21 below). Individual instability features in all 5 FS cases exhibit characteristics resembling common morphologies of convective and shear instabilities, but they evolve in localized regions that preclude the application of plane-parallel flow analysis in this environment. In all 5 FS cases, successive large-scale instabilities form above and below the initial instabilities as features in the initial instabilities progress rapidly to smaller spatial scales. Though the initial instability evolutions begin at different

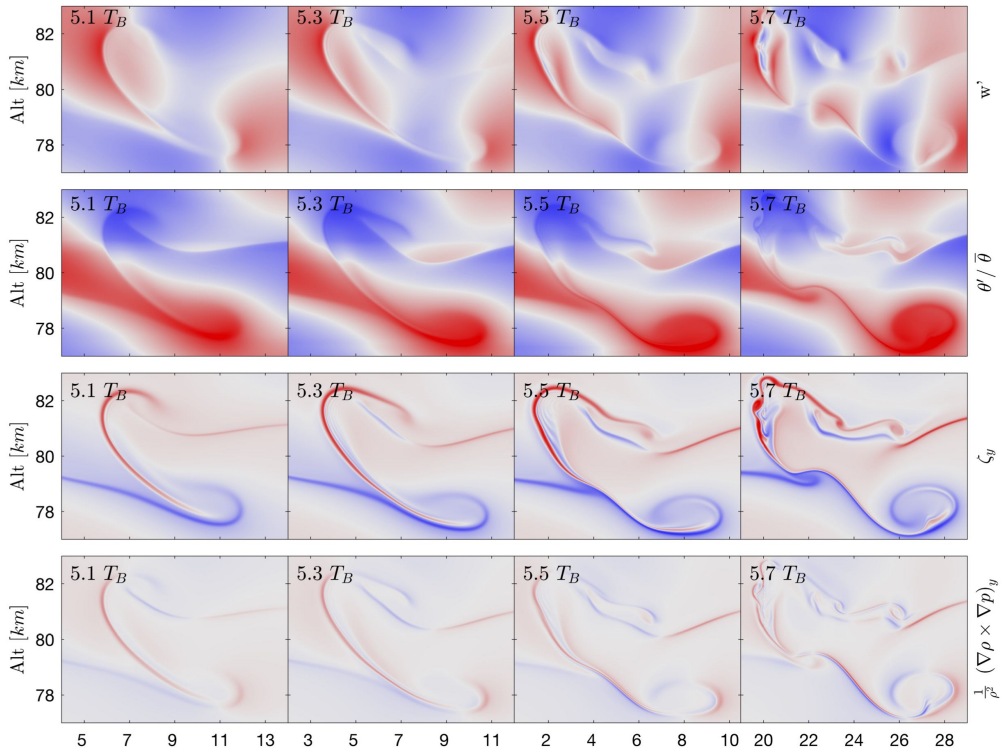

Figure 7.16: As in Figure 7.7 for Case 6. Similar to Case 5, the initial instabilities develop simultaneously in the regions of positive ζ_y (negative ζ_y) at the top (bottom) of the main vortical structure and slightly precede the instability onset in Case 5, owing to faster vorticity evolution caused by N^2 FS baroclinic contributions.

times, the progression to smaller scales and higher ζ_y amplitudes appears roughly the same when viewed at $1T_B$ increments, suggesting similar ϵ for each case (for further discussion of the turbulent scale progression, see paragraph accompanying Figure 7.20 below). Since the dominant component of ζ_y is $\frac{\partial u}{\partial z}$, regions of strong ζ_y indicate the locations of large scale features that appear in $\Delta\overline{U}$, i.e. $\overline{\zeta}_y \approx \frac{\partial}{\partial z}\left(\Delta\overline{U}\right)$. Dominant features in $\Delta\overline{U}$ align with the vortical tendencies imposed by the initial FS and retain the same orientation as turbulence evolves, suggesting that induced wind from both the GW momentum flux and turbulent dissipation will match the tendencies of FS imposed on the initial background. This agreement provides a pathway for understanding how individual instability evolutions dictate the GW impact on the large-scale, background flow.

The shifted timescales of the instability evolutions are better understood by examining

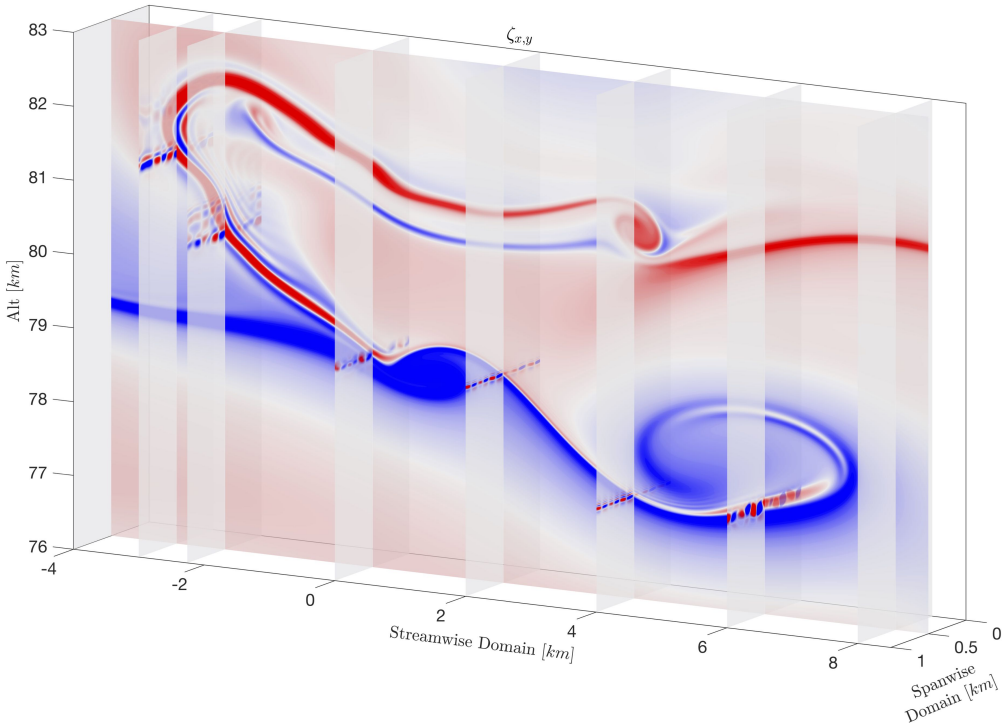

Figure 7.17: As in Figure 7.10 for Case 5 at $5.9T_B$.

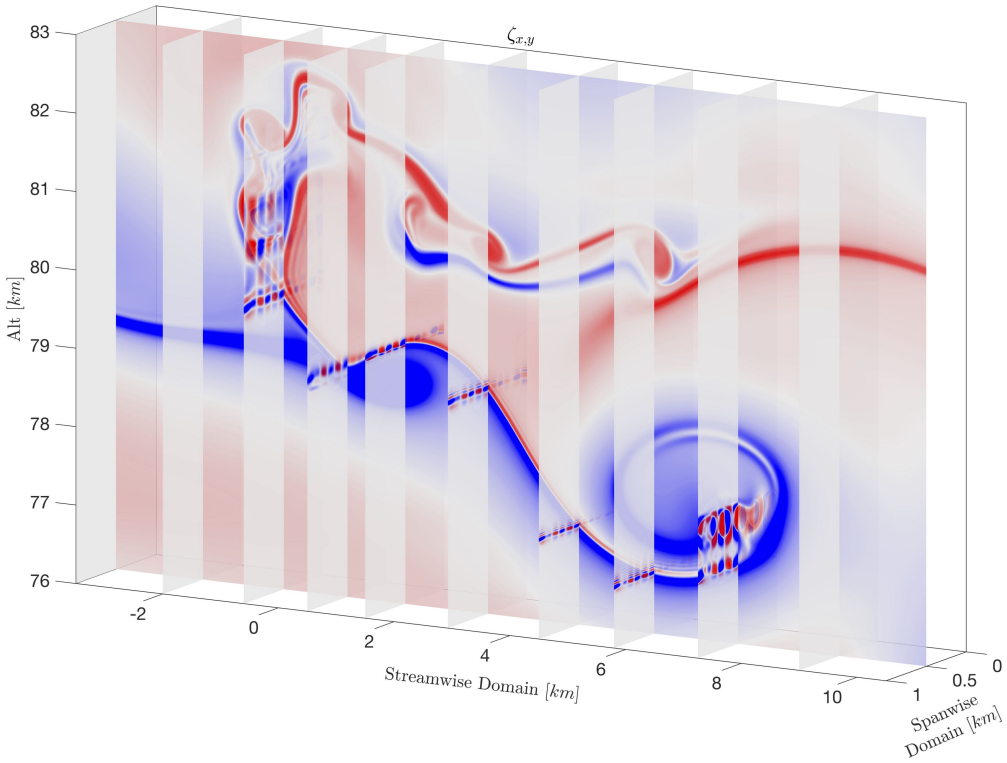

Figure 7.18: As in Figure 7.10 for Case 6 at $5.7T_B$.

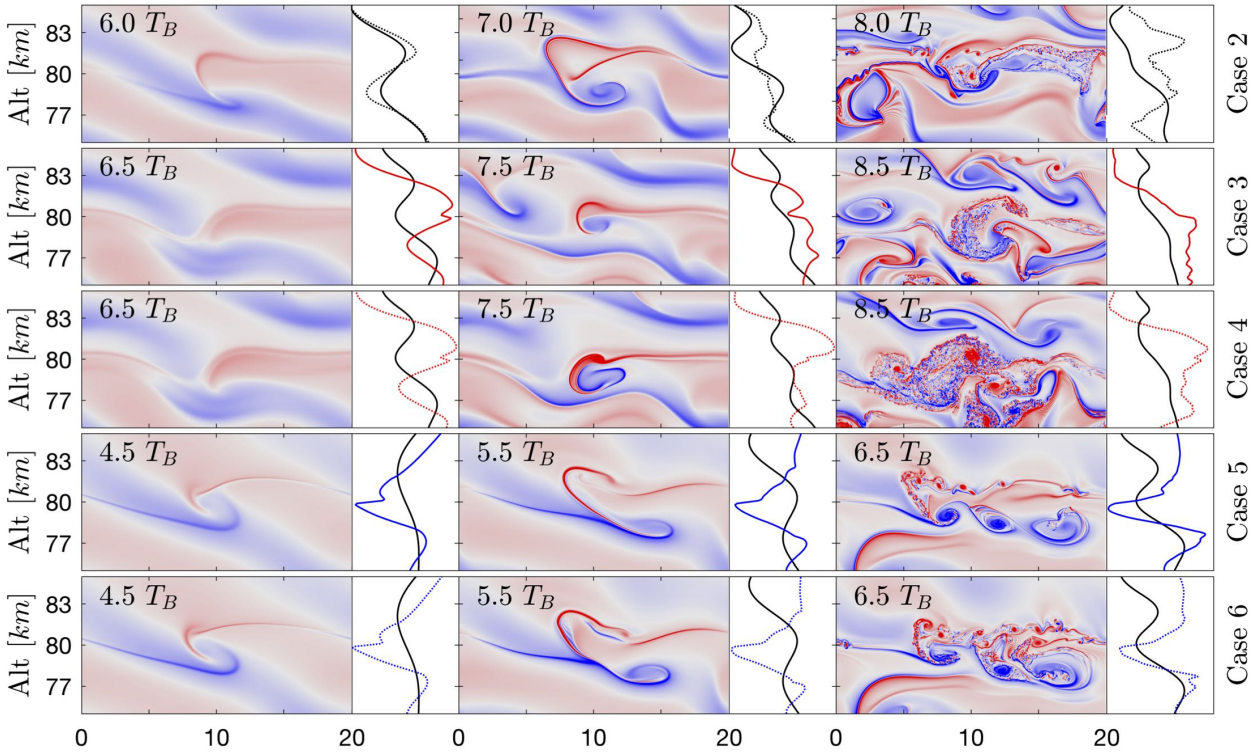

Figure 7.19: ζ_y fields and $\Delta\overline{U}$ profiles showing turbulence evolution for Cases 2 to 6. The ζ_y domain translates horizontally to emphasize the evolution of the dominant vortical structure. Solid black lines in the profiles show the corresponding $\Delta\overline{U}$ for Case 1 to emphasize changes to the induced wind as a consequence of FS in Cases 2 to 6. Dominant $\Delta\overline{U}$ features align with the initial vortical tendencies for each FS case, suggesting that dissipative tendencies follow FS locations and orientations.

Figure 7.20, which presents the power spectral density (PSD) periodograms of the u' horizontal wavenumber spectra as turbulence evolves in all 6 cases. The wavenumber spectra are averaged from 77 to 83 km to show the relative spatial energy distributions among the 6 cases, with the 5 FS cases converging to near-identical spectra at $\sim 8.5T_B$ when the turbulence has evolved. At each point in time, the wavenumber spectra exhibit a falloff scale marked by a sharp reduction in PSD amplitude at the high wavenumber end of the spectrum. For fully-evolved turbulence, this scale corresponds to $\sim l_0$, which marks the transition from the $-\frac{5}{3}$ slope of the inertial subrange to the sharper exponential cutoff of the viscous subrange (Tatarski, 1961). Dashed lines indicating slopes of $-\frac{5}{3}$ and -7 (an approximate slope for the viscous subrange from Heisenberg (1948)) are shown in the $8.5T_B$ panel for reference.

With similar ϵ for each case, the falloff scale indicates the smallest energy-containing scale at a given time, providing a temporal comparison of how far the turbulence evolution has progressed for each case. By $5.5T_B$, all 5 FS cases have more evolved turbulence than Case 1, with the two negative $\overline{U}_z$ cases (5 and 6) having smaller energy-containing scales than Cases 2 to 4 accompanying their earlier instability onset. By $6.5T_B$, the strong solenoidal tendencies in Case 2 have produced more evolved turbulence than the two positive $\overline{U}_z$ cases, placing the falloff scale for Case 2 midway between those of Cases 3 and 4 (positive $\overline{U}_z$) and Cases 5 and 6 (negative $\overline{U}_z$). By $7.5T_B$, the active turbulence evolution in all 5 FS cases begins to converge on the eventual spectrum seen at $8.5T_B$, where the $\sim -\frac{5}{3}$ slope region indicates an approximate inertial subrange of ~ 80 to 1000 m. The shift to a steeper exponential slope marks the transition to the viscous subrange, with an approximate l_0 of ~ 80 m.

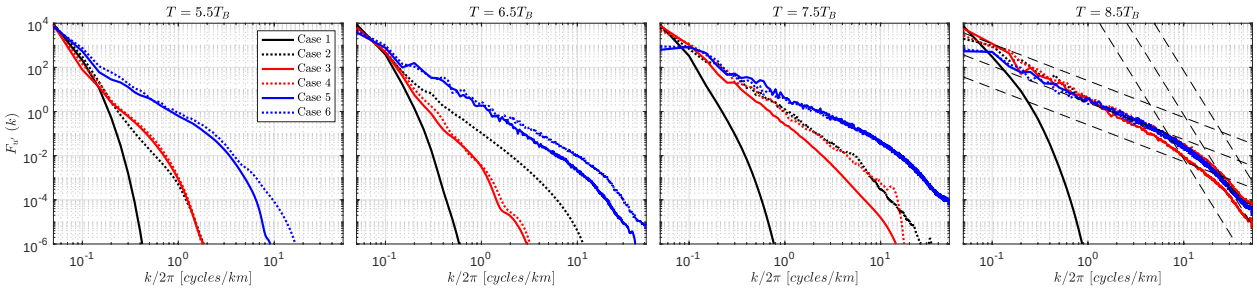

Figure 7.20: Normalized PSD plots of the u' horizontal wavenumber spectra averaged about the FS altitude as turbulence evolves in all 6 cases. The final panel at $8.5T_B$ shows the turbulent energy cascade imposed by the LES scheme, with $-\frac{5}{3}$ and -7 slope lines shown for reference to identify an inertial subrange of $\sim 80 - 1000$ m and a viscous subrange for spatial scales less than $l_0 \sim 80$ m. With similar ϵ values for Cases 2 to 6, the falloff scale in each wavenumber spectrum shows how far turbulence has progressed for each simulation at a given point in time.

It is worth noting that for each panel in Figure 7.20 before $8.5T_B$, the case order from largest to smallest falloff scale is identical: Case 1, Case 3, Case 4, Case 2, Case 5, Case 6. A closer evaluation of these relationships yields the following conclusions: 1) The presence of any FS type or orientation accelerates the tendency for instabilities and turbulence for a background GW of large amplitude. 2) For a given initial wind profile, adding N^2 FS (Cases 2,4,6, relative to Cases 1,3,5, respectively, i.e. dashed vs. solid lines) accelerates the

evolution of small scale features despite having larger initial Ri_{min}, increasing the baroclinic sources and intensities of small-scale vorticity that drive instabilities and GW dissipation. 3) For a given initial N^2 profile, adding negative $\overline{U}_z$ FS (Case 6 relative to Case 2) accelerates small scale feature evolution while adding positive $\overline{U}_z$ (Case 4 relative to Case 2) slows it down, owing to the constructive and destructive superposition of ζ_y tendencies that amplify negative $\overline{U}_z$ or reduce positive $\overline{U}_z$ and the vortical effects imposed by the N^2 FS, as discussed above. 4) $\overline{U}_z$ FS has a more dominant impact on the degree of scale progression acceleration than N^2 FS-adding $\pm\overline{U}_z$ FS to the N^2 FS (Cases 4 and 6 relative to Case 3) drastically shifts the scale energy distribution, whereas adding N^2 FS to the $\pm\overline{U}_z$ FS (Case 4 relative to Case 3, Case 6 relative to Case 5) produces a relatively smaller decrease in the falloff scale at a given time. As seen above, this behavior is also apparent in the instabilities, as the two cases for each $\overline{U}_z$ FS orientation form initial vortices with matching orientation and ζ_y sign.

Figure 7.21 shows the $\Delta\overline{U}$ evolution for Cases 1 to 6, with the final profiles shown together at $10T_B$. All 5 FS cases have distinguishing features both in their time evolution and their final profiles. In the absence of $\overline{U}_z$ FS, Case 2 bears the most resemblance to Case 1, having near identical time evolution up to $6T_B$ when instability onset occurs. Though the inclusion of N^2 FS in Case 2 results in a distinct final $\Delta\overline{U}$ profile relative to Case 1, adding N^2 FS to either $\overline{U}_z$ FS Case (Cases 4,6 relative to Cases 3,5) does not produce any distinctive change to the final $\Delta\overline{U}$ state. The two positive $\overline{U}_z$ cases both exhibit increased $\Delta\overline{U}$ above 80 km, while the two negative $\overline{U}_z$ cases exhibit decreased $\Delta\overline{U}$ above 80 km. These behaviors are a consequence of positive $\overline{U}_z$ influence on GW propagation, where positive (negative) $\overline{U}_z$ increases (decreases) the GW vertical group velocity and facilitates greater (reduced) momentum flux of the GW as it moves above the FS altitude. In the negative $\overline{U}_z$ cases, the GW effects are amplified at and below the FS layer as the GW takes longer to propagate through the initial negative shear than through the initial wind profiles in Cases 1 to 4, contributing to earlier vorticity buildup and instability onset in those cases. Though wind deceleration above 80 km lags in Case 1 relative to the positive $\overline{U}_z$ cases in the absence of

accelerated vertical group velocity, the GW eventually produces a comparable $\Delta\overline{U}$ at 85 km as GW propagation continues in the absence of instability. All 5 FS cases develop regions of increased $\Delta\overline{U}$ near 70 km at $8T_B$ as a region of predominantly negative ζ_y accumulates at the interface of the downward expanding turbulence.

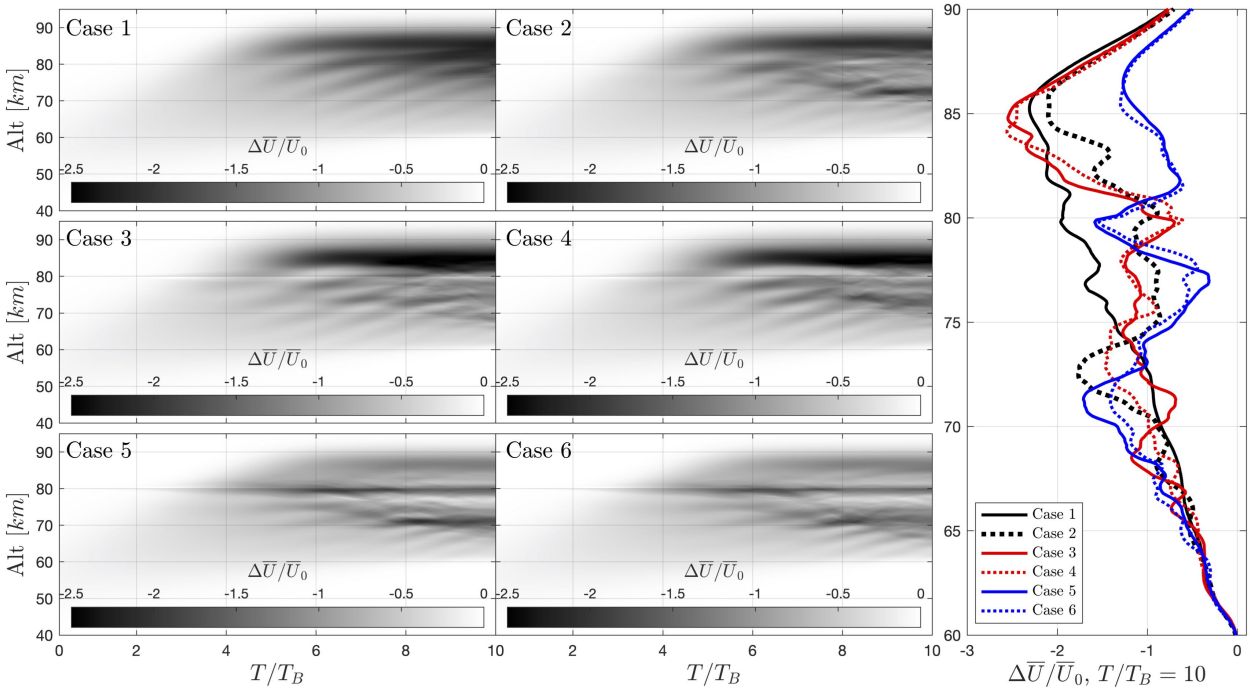

Figure 7.21: $\Delta\overline{U}/\overline{U}_0$ evolutions for Cases 1 to 6, with the profiles of all 6 cases at $10T_B$ together in the right panel. The distinctive features which develop early on at the FS altitude are retained in the final $\Delta\overline{U}/\overline{U}_0$ profiles, suggesting that the energy contributions of successive instabilities preferentially align with the vortical tendencies imposed by the initial FS. The depths of the shear-induced features in Cases 3 to 6 are an order of magnitude larger than their initial FS depths, demonstrating that the influence of GW-FS interactions on background wind evolution is greater than previously thought, even for relatively small layer depths and initial amplitudes.

The most pronounced $\Delta\overline{U}$ deviation from Case 1 occurs at the initial FS altitude, where Cases 3 and 4 (positive $\overline{U}_z$) exhibit a local reduction in $\Delta\overline{U}$ and Cases 5 and 6 (negative $\overline{U}_z$) exhibit a local increase in $\Delta\overline{U}$ in the $10T_B$ profiles from Figure 7.21. This behavior traces back to the evolution of the dominant ζ_y structures, where accumulated influence of the prevailing positive (negative) $\overline{U}_z$ determines the slope of the induced wind to create an amplified local reduction (increase) in $\Delta\overline{U}$ as the GW dissipates and transfers momentum

to the background wind. The $\sim$ 5 to 7 km depths of these excursions are an order of magnitude larger than the initial FS, with $30m/s$ $\Delta\overline{U}$ amplitudes three times larger than the velocity difference $(U_1 - U_0)$ imposed by the initial FS. The scale increase of the $\Delta\overline{U}$ impacts of the final states cannot be emphasized enough; even with benign initial FS depths and amplitudes, GW-FS interactions have the potential to generate lasting, GW-scale wind features with consequences for subsequent GWs in the MLT.

7.4 Expanding on Previous Findings

These results build on the many cases of observed and simulated GW-FS interactions by providing a comprehensive analysis of the instabilities and induced influences produced by GW propagation through isolated FS having different compositions. While previous studies emphasize the potential for FS to produce instabilities and influence the altitude of GW breaking, none have attempted to diagnose the unique behaviors associated with different FS superpositions and orientations and the resulting GW momentum deposition. High resolution DNS simulations to date provide accurate turbulence characterization but are generally constrained to thin, vertically periodic domains, whereas deep, coarsely-resolved simulations diagnose GW dynamics over broad altitude ranges at the expense of accurate energetics and turbulence descriptions at small scales. Simulation results presented here utilize a deep domain with high resolution and LES, enabling the characterization of large-scale GW breaking implications to an environment representative of the MLT with accurate FS evolution and turbulent energetics. It is worth noting that shear and stability FS observed in the MLT often have much larger magnitudes than those examined in this study (see e.g., Cao et al., 2016; Bossert et al., 2015, 2016; Fritts et al., 2014b); that GW propagation through relatively weak FS produces such significant impacts on the tendencies for GW dissipation and momentum deposition suggests that such events in the atmosphere having comparable or stronger FS features will have comparable or larger impacts on GW propagation and momentum transport and deposition.

Agreeing with the findings of Fritts et al. (2009a), the results of this study confirm the tendency to form GW-scale instabilities with much thinner initial layers of reduced amplitude, and further evaluate the instability morphologies for different layer compositions. Fritts et al. (2009a) also found that the dynamics of GW-FS interactions are orientation-dependent, much like the findings of Heale and Snively (2015) regarding high-frequency GW filtering by IGWs, and the results presented here expand on these findings by diagnosing the consequences of layer directionality and how they influence the background wind.

The results of this study further benefit from anelastic modeling enabling a larger vertical domain, having more direct relevance to dynamics in the MLT. Similar studies by Heale and Snively (2015) and Heale et al. (2017) have employed domains that were sufficiently large to represent accurate GW propagation in the MLT, but the simulations were resolution-constrained in a 2D domain with 500 m grid resolution, allowing no characterization of smaller-scale instability dynamics that might otherwise have arisen. Simulations in this study improve on these limitations by utilizing an 85 km vertical domain with resolved scales in 3D down to 10 m at 80 km, such that they are able to characterize 3D instability evolutions extending to turbulence scales in representative MLT environments.

In a recent two-part study, Fritts et al. (2018a) and Fritts et al. (2018b) simulated GW propagation into a mesospheric inversion layer (MIL), imposing a 100% amplitude N^2 enhancement and deficit below and above 80 km, yielding a 10 km MIL with an adiabatic layer on top. They identified important baroclinic influences on the vorticity evolution accompanying the initial instabilities, and they provided an extensive analysis of the turbulent energy dissipation and associated dynamics and fluxes. However, they did not consider additional influences of $\overline{U}_z$ on their imposed N^2 FS. To our knowledge, the present study is the first evaluation of combined $\overline{U}_z$ and N^2 FS impacts on GW propagation.

7.5 Summary

Results reported here describe responses for GWs propagating through shear and/or stability FS at 80 km to study the impact of FS characteristics on GW propagation, instability dynamics, and enhanced dissipation in the MLT. Case 1 establishes the baseline propagation characteristics for a HFGW in a uniform background, where the GW exhibits 1) SA onset after $\sim 4T_B$, which accelerates c in the direction opposed to GW propagation above 80 km and kinks the phase structure; 2) separation of u and w phase alignment between increased and decreased λ_z; 3) progression of w' amplitude modulation down from the altitude of the initial shift in λ_z, which manifests as changes in the GW momentum flux and ultimately the induced wind; and 4) amplitude-modulated wind profiles with perturbations that diminish with time, leaving a nearly-uniform $\frac{\partial \overline{U}}{\partial z}$ at $10T_B$ with maximum induced $\Delta\overline{U}$ at 85 km. In the absence of initial FS, GW propagation continues past $10T_B$ without producing any local instabilities.

Distinctive behaviors in Cases 2 to 4 can be traced to unique influences of N^2 and positive $\overline{U}_z$ FS. N^2 FS in Case 2 produces negative ζ_y below the initial layer and positive ζ_y enhancement to vertically aligned features as the FS rotates, with accelerated instability formation and initial counterclockwise vortices at the bottom of the resulting vorticity structure. Positive $\overline{U}_z$ FS in Case 3 produces a large region of positive $\overline{U}_z$ above the initial layer and a relatively smaller initial vortical structure, with slower instability formation and initial clockwise vortices at the top of the resulting vorticity structure. Case 4, with both positive $\overline{U}_z$ and N^2 FS, produces a combination of these effects, having instability character determined by the positive $\overline{U}_z$ FS and stronger vorticity with more rapid instability onset driven by the solenoidal tendencies induced by the N^2 peak.

The prominent features of Cases 5 and 6 help to distinguish between the effects of negative and positive $\overline{U}_z$ FS, and they reinforce the distinctions between N^2 and $\overline{U}_z$ FS influences in Cases 2 to 4. The negative $\overline{U}_z$ FS in both cases develops strong negative

ζ_y sheets below the initial FS and weaker positive ζ_y sheets above, producing initial large vortices on the intensified negative $\overline{U}_z$ and smaller vortices on the upper positive ζ_y sheet at the same time. As with the comparison of Case 4 and Case 3, the heightened baroclinity from the added N^2 layer in Case 6 intensifies the vertically aligned positive ζ_y sheet and accelerates instability evolution relative to Case 5. Negative $\overline{U}_z$ FS in both cases produces similar vortical tendencies to Case 2, but the initial instabilities evolve earlier and occur simultaneously above and below the layer. The qualitative similarity between Cases 5 and 6 again suggests that $\overline{U}_z$ FS plays a larger role in the vortical evolution of the flow while N^2 FS encourages earlier evolution of small scale features without altering the larger vortical structure.

The unique evolutionary characteristics of the GW-FS interactions in Cases 2 to 6 culminate in several important implications for the local environment, both in terms of sustained impacts of the final states and at finite time scales where transient distinctions are important. The smallest energy-containing scales at each time identify how far each case has progressed in its turbulence evolution, showing how the superposed vortical tendencies of each FS component delay or accelerate the onset of turbulence. The locations and relative intensities of dominant features in ζ_y clearly impact the GW momentum flux contributions to the background flow and largely dictate the lasting features that form in the induced wind. The locations of sustained features in the induced wind are determined by $\overline{U}_z$ FS, where the $\sim 30\ m/s$ amplitudes and ~ 5 to $7\ km$ depths dwarf the benign magnitudes of the initial FS forcing.

Chapter 8

Gravity Wave Propagation through an Evolving Inertial Wave in the MLT

This Chapter presents a simulation study characterizing the propagation of a HFGW through an evolving IGW background, an event observed by lidar and AMTM instruments at ALOMAR, Norway (69N, 16E). The variable environment posed by the background IGW can be perceived as a series of shear and temperature layers of various amplitudes and depths, each having direct physical consequences to the GW's intrinsic characteristics in a manner similar to the isolated layer interactions described in the previous chapter. The time-evolving background changes the propagation dynamics for the HFGW throughout the duration of the event, producing what appears to be intermittent propagation of the same GW at distinct times in the AMTM data. This case study provides a prime opportunity to explore the dynamics of transient GW propagation in a variable large-scale background, an environment which has only been considered in idealized simulation studies and cannot be characterized by current mesoscale models.

This event presents a challenging case to interpret without the aid of numerical simulations, as there are two critical discrepancies in the observed GW behavior between the two instruments:

(1) The AMTM observes intermittent GW propagation over the event, whereas the lidar data indicates that the GW should be present at the AMTM altitude through the full duration of the event; and

(2) The intrinsic characteristics of the GW identified in the AMTM indicate that it

should encounter a 6 km evanescent region immediately below the AMTM altitude, yet the AMTM shows GW phase motion indicative of GW energy passing through the AMTM and reaching higher altitudes, suggesting propagation dynamics that defy linear Ray Theory assumptions.

The goal of the simulation study for this event is to resolve these two discrepancies in the observations and ascertain the dynamics of the GW propagation that can explain these phenomena. Simulations of this data utilize the anelastic code's capacity to contextualize these measurements beyond their spatial and temporal constraints to explain their underlying dynamics. Data from the AMTM show the horizontal wavelengths, horizontal phase speed, and orientation of the GW with respect to the background winds. Lidar wind and temperature profiles show the evolution of the background IGW, and filtered profiles of the lidar data identify the vertical phase structure and perturbation amplitudes of the HFGW activity. These two datasets together provide the necessary parameters to simulate the GW propagating through this background environment and discern its underlying behavior.

The Chapter is organized as follows: The observational characteristics for this event are described in Section 8.1, including AMTM and lidar data in Sections 8.1.1 and 8.1.2, respectively. The simulation results are presented in Section 8.2, including the simulation methodology in Section 8.2.1, an overview of the whole event duration in Section 8.2.2, and the behavior at the times of the four distinct propagation regimes in the AMTM data in Sections 8.2.3 through 8.2.6, respectively. A summary of the findings and their implications is given in Section 8.3.

8.1 Event Characteristics Determined from Observations

On 21 January 2015, a sodium resonance lidar and advanced mesospheric temperature mapper (AMTM) observed intermittent propagation of a HFGW through an IGW over ALOMAR, Norway. The ALOMAR observatory is located at 69.3^o N latitude, with a cor-

responding inertial frequency of $f = 1.364 * 10^{-4} s^{-1}$ and an inertial period of 12.8 hours. Given that f is much higher than near equatorial latitudes, propagating GWs satisfying $f < \omega < N$ fall into a narrower range of frequencies than those at lower latitudes. The AMTM and lidar instruments used in this study are described in Chapter 4.

8.1.1 AMTM

The AMTM observations are shown at ∼21 Universal Time (UT), ∼23 UT, and ∼24 UT in Figure 8.1, where a HFGW of roughly identical wavelength, phase speed, and orientation is visible at ∼21 to 22 UT and then again at ∼24 to 25 UT. From ∼22 to 23 UT, small-scale features of several sizes and orientations cover the entire domain, and the GW phase structure is not visible. These features commonly indicate a superposition of linear wave instabilities that arise as a consequence of local forcing variations, and they indicate an evolution toward small-scale turbulence occurring beyond the observable resolution of the AMTM.

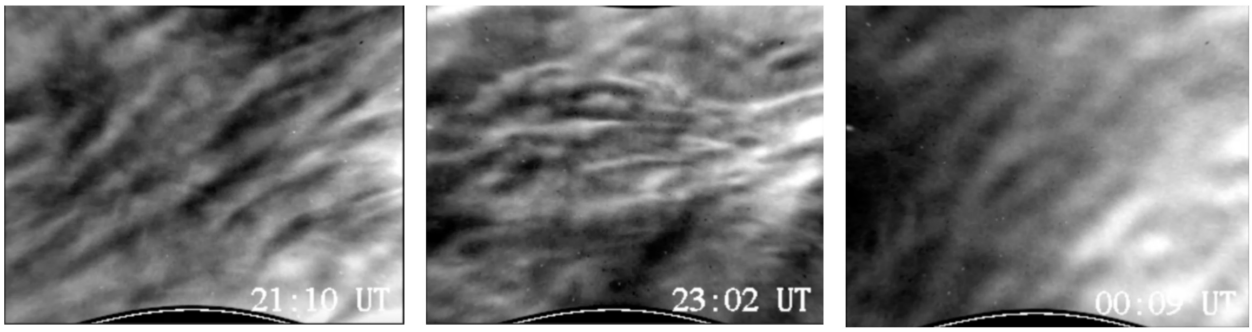

Figure 8.1: AMTM images from ∼21 UT, ∼23 UT, and ∼24 UT. GW phase structures with similar propagation characteristics are visible at ∼21 UT and ∼24 UT.

GW parameters derived from the AMTM observations are shown in Figure 8.2, taken at ∼21 UT when the GW is propagating. When observed at ∼21 UT, the propagating GW has a horizontal wavelength of $\lambda_x = 19$ km (panel 1), with an observed phase speed of $c = 15 m/s$ to the northwest calculated from phase motion between successive AMTM images. The corresponding GW perturbations observed in the lidar data should have a

period of $\frac{19000\ m}{15m/s} = 21$ min. The peak temperature perturbation amplitude of the observed GW is $\pm 3K$, shown in panel 2, though the amplitude may be reduced by averaging of the OH layer. OH density measurements from the nearest Sounding of the Atmosphere using Broadband Emission Radiometry (SABER) satellite overpass (panel 3) show the center of the OH layer at 86 km, indicating the approximate altitude of the AMTM data.

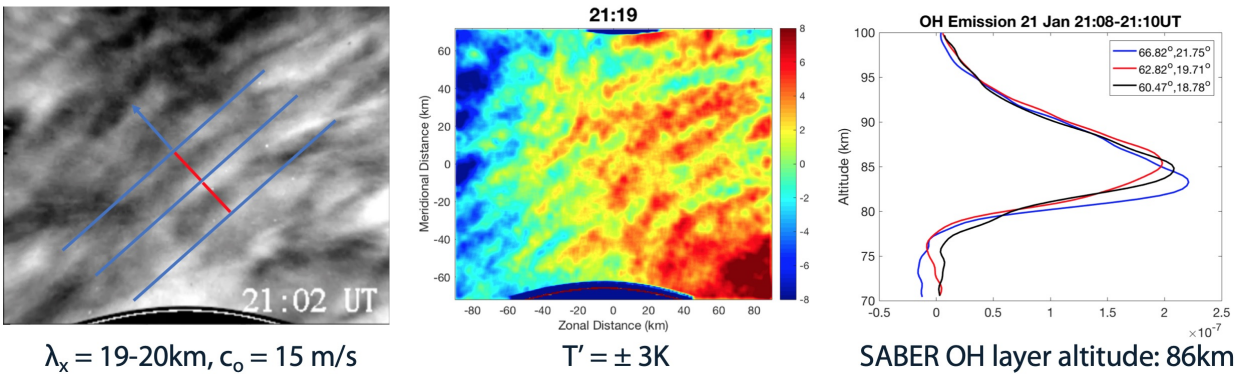

Figure 8.2: Propagating GW parameters derived from (a). the AMTM OH brightness intensity, which shows the movement of GW phase structures; (b). AMTM OH temperature fields, which show temperature perturbation amplitudes corresponding to the GW; and (c). SABER OH layer altitude as indicated by the nearest SABER satellite overpass. The respective GW parameters are labeled beneath each plot.

8.1.2 Lidar

Hourly-averaged wind and temperature profiles from the sodium lidar are shown in Figure 8.3, with the approximate AMTM altitude shown in red. The wind vector U is a projection of the wind magnitude in the plane of the GW propagation calculated from the N (meridional) and E (zonal) wind components, where positive U points toward the Southeast and the GW propagation direction is upwind (negative U). Winds are spliced together with wind data from the Saura MF radar to extend the data below 70 km. A large region of descending negative shear is visible above the AMTM for the full duration of the event, with an additional region of negative shear visible below the AMTM altitude from ~19 to 21 UT. Given that the GW will see a critical level where $U \leq -15m/s$, there's a high potential for intermittent filtering of the GW through this event.

The total wind field and temperature fields measured by the lidar are shown in Figure 8.4, with a seven hour filter applied to the winds in the left panel and no filter applied to the temperature data in the right panel. Winds in the left panel are spliced together with wind data from the Saura MF radar to extend the data down to 65 km. With a seven hour filtering period, an IGW is clearly visible in the upper region of the sodium layer, corresponding to the descending negative shear seen above 90 km in the hourly wind profiles. The temperature field shows many high frequency perturbations throughout the observational period which could account for the small-scale features observed in the AMTM from ~22 to 23 UT.

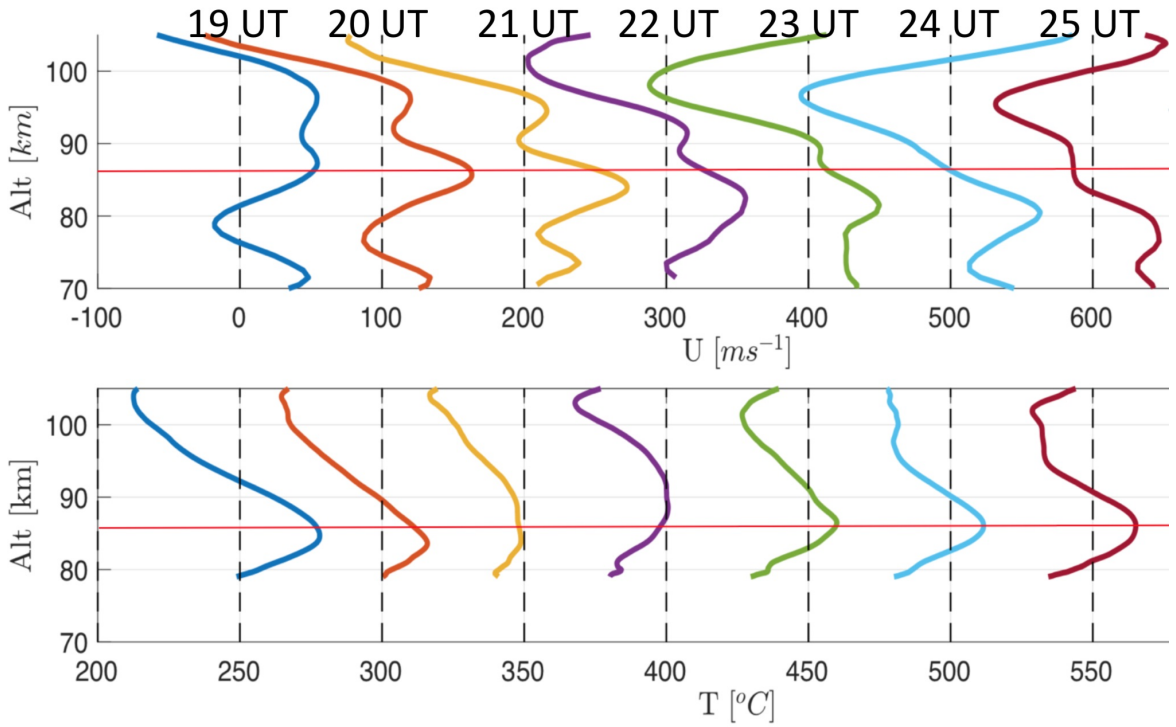

Figure 8.3: Lidar wind (top) and temperature (bottom) profiles for the event. U is projected to have the positive direction pointing to the southeast. The red line at 86 km shows the approximate center of the OH layer, indicating the altitude region visible in the AMTM.

Knowing the vertical wavelength and observed horizontal phase speed of the GW, the intrinsic frequency ω can be calculated from the lidar wind profiles as

$$\omega = k(c - U) = \frac{2\pi}{19000\ m}(U + 15m/s) \tag{8.1}$$

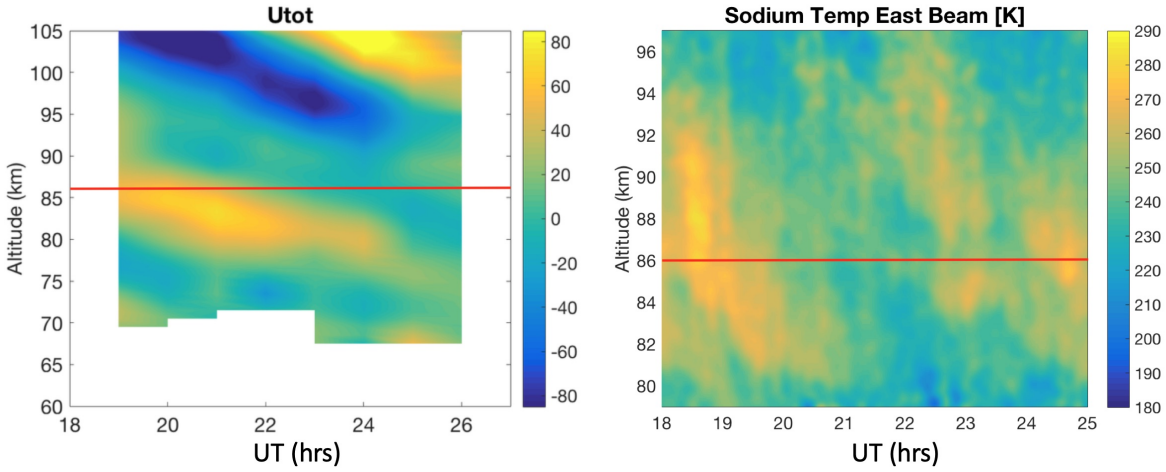

Figure 8.4: Sodium lidar and Saura wind measurements (left) and lidar temperature measurements (right). The wind data is filtered to emphasize the 7 hour IGW above 80 km, and the temperature data is unfiltered to show the higher frequency components present throughout the event.

The Brunt-Vaisala frequency N can also be calculated from the lidar temperature profiles as

$$N^2 = \frac{g}{T}\left(\frac{\partial T}{\partial z} + \Gamma\right) \tag{8.2}$$

where Γ is the lapse rate. Figure 8.5 shows the ω and N profiles calculated from the lidar data for each of the hourly averaged profiles. Each altitude range is color coded to indicate the expected propagation characteristics: green for vertical propagation, yellow for evanescence, i.e. $\omega > N$, and red for critical level filtering above altitudes where $\omega \to 0$, i.e. $U = c$. ~19 UT and ~20 UT profiles both have a critical level below the AMTM, making it unlikely for the GW to reach AMTM altitudes prior to ~21 UT. The AMTM also appears to be in an evanescent region from ~19 to 21 UT, making it likely that the GW observed at ~21 UT is seen at a slightly higher altitude where $\omega < N$ and phase motion would be visible within the FWHM extent of the OH layer. Looking at the ~21 UT ω profile, the GW in the AMTM is likely observed with $0.008 \leq \omega \leq 0.016 s^{-1}$, with a corresponding vertical wavelength of $\lambda_z \sim 10$ to 30 km.

The ~30 minute filtered lidar temperature perturbations are shown in Figures 8.6.

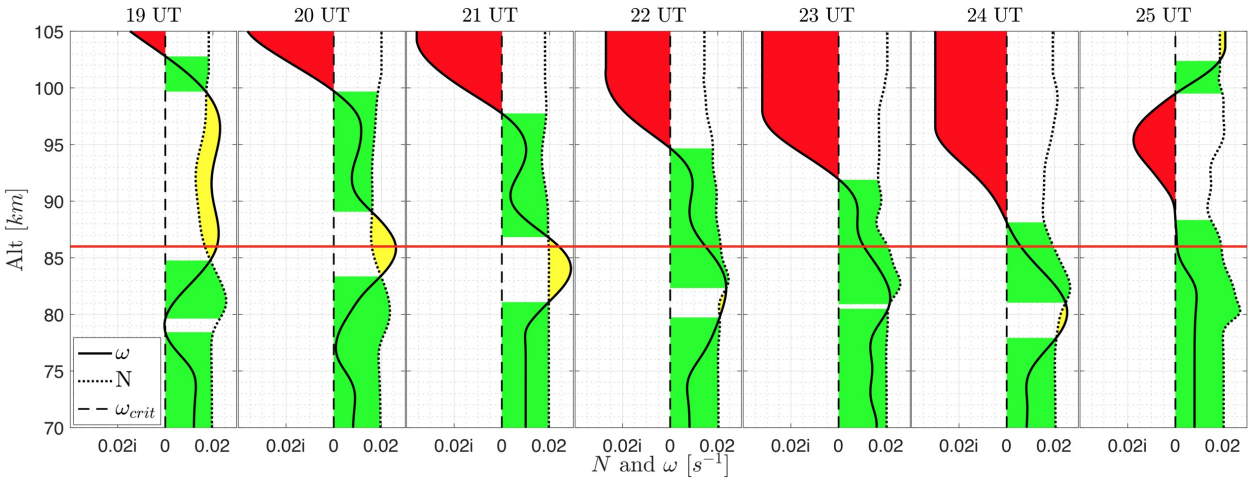

Figure 8.5: Hourly-averaged profiles of ω and N from the sodium lidar (80 to 105 km) and Saura data (70 to 80 km), with altitude ranges color-coded to indicate regions of GW propagation (green), evanescence (yellow), and critical level filtering (red).

Perturbations were obtained by subtracting the average background temperature at each altitude, and applying a bandpass time filter with 40 dB stopbands for periods less than 4 minutes and periods greater than 70 minutes. The lidar temperature amplitude at ∼21 UT is comparable to the AMTM, but higher temperature amplitudes of $\pm 8K$ are also observed at 80 km and 90 to 94 km in the east beam, suggesting higher temperature amplitudes in the initial GW that are diminished at 86 km where evanescence is predicted by the lidar wind profiles. The reappearance of higher amplitudes above the evanescent region suggests that the GW reaches higher altitudes by tunneling through the evanescent region. The filtered temperature perturbations over the whole event duration show no obvious intermittency in the GW signature from ∼20 to 25 UT, suggesting that the GW source is continuous despite not being visible in the AMTM from ∼22 to 24 UT. The lidar also shows higher temperature amplitudes below the AMTM altitude range at ∼23 UT, indicating the potential for partial GW reflection below the evanescent region indicated in Figure 8.5.

The local Ri must be considered to evaluate the potential for instabilities from ∼22 to 23 UT. While a single wind profile is calculated from the north and east beams, each beam has its own temperature profile, leading to different Ri profiles for each beam. Ri

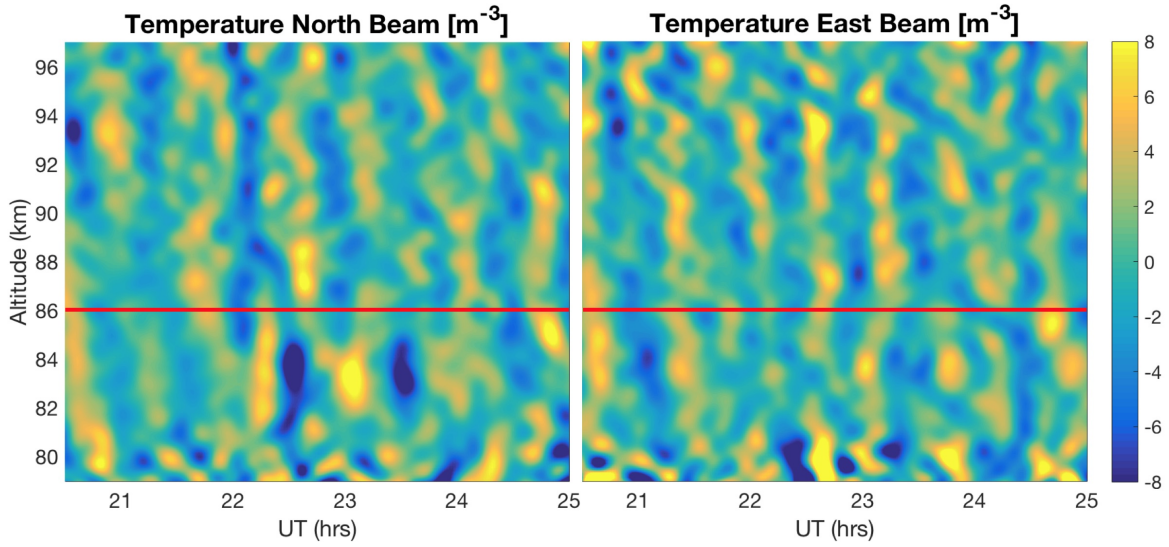

Figure 8.6: Lidar temperature perturbations from the north and east beams with ∼30 minute bandpass filtering applied. GWs matching AMTM characteristics at ∼21 UT occur continuously from ∼20 to 25 UT, with amplitude variations suggesting regions of evanescence and tunneling behavior at the altitudes indicated by the temperature profiles.

calculated from the lidar data is shown in Figure 8.7 for the north and east beams, as well as the average of the two. All three plots show the tendency for convective or shear instabilities just above 86 km at ∼22 UT, likely explaining the instabilities seen in the AMTM. Both individual beams also show $Ri < 0$ at ∼23 UT, but owing to the altitude offset between these observations, the instability tendency does not appear in the averaged Ri. Because the east and north beams are each pointed 20 degrees off zenith, there is a ∼80 km horizontal offset between the two beams at 86 km, creating the potential for an extended instability region to be observed at different altitudes in each beam, i.e. along the slanted phase of a GW. This suggests a high degree of localization to the instability dynamics such that while appearing domain-wide in the AMTM, they may not be widespread-enough to stop GW propagation through the AMTM region. Bearing this in mind, the temperature profile from one of two beams, rather than the average, is used to evaluate the GW propagation from ∼22 to 23 UT to address the potential for local instability dynamics.

The localized ω and N profiles derived from 30-minute averaged profiles and a single

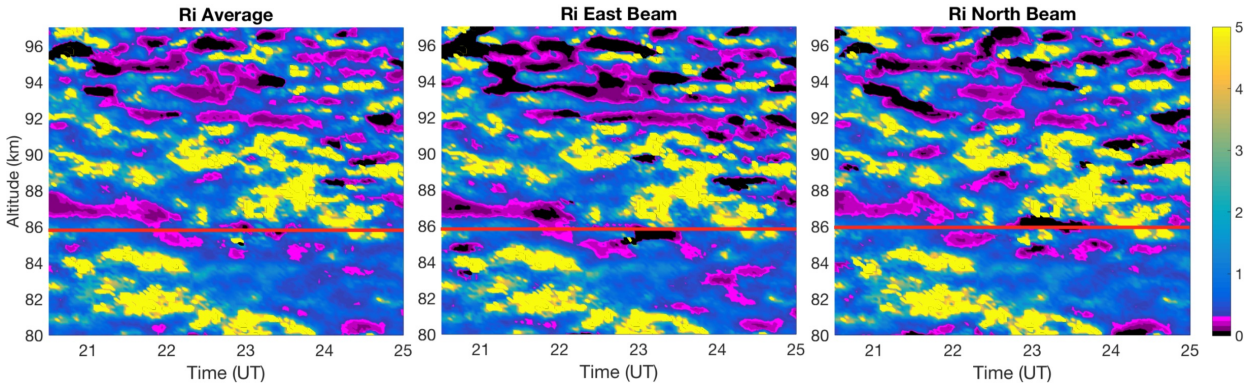

Figure 8.7: Ri from lidar winds and temperatures, showing convective (negative Ri, shown in black) and shear (positive $Ri < 0.25$, shown in purple) instability tendencies from ∼21 to 23 UT. That convective Ri occurs at different altitudes in East and North beams suggests horizontally localized instability conditions that do not cover entire AMTM domain.

beam temperature are shown in Figure 8.8 for ∼22 to 23 UT. Given the timescales of Ri evolution, the background profiles used for simulations at ∼22 UT and ∼23 UT employ 30 min filtering rather than 60min filtering to capture the instability tendency in these regions. At ∼22 UT, the strong negative shear at the AMTM altitude creates a high likelihood for shear instabilities, and with a critical level immediately above the layer it is expected that local propagation at this time will be constrained just above the AMTM. The ∼23 UT profile, calculated from the east beam only, shows an overturning region of near-constant density ($N^2 \to 0$) just below the AMTM that will likely generate convective instabilities.

8.2 Event Characteristics Determined From Simulations

The model domain extends 19 km (one GW λ_x) in the streamwise (x) direction, 0.5 km in the spanwise (y) direction, and from 20 to 120 km in altitude (z). The domain employs periodic horizontal boundary conditions and a 10 km sponge layer at the top of the vertical domain, capping the useable domain at $z = 110\ km$. The code is executed on Department of Defense high performance supercomputers with a 2-D $(Nx, Ny, Nz) = (512, 1, 1024)$ grid, having streamwise grid resolution of $\Delta x = 40\ m$ and a power-law stretched vertical mesh with

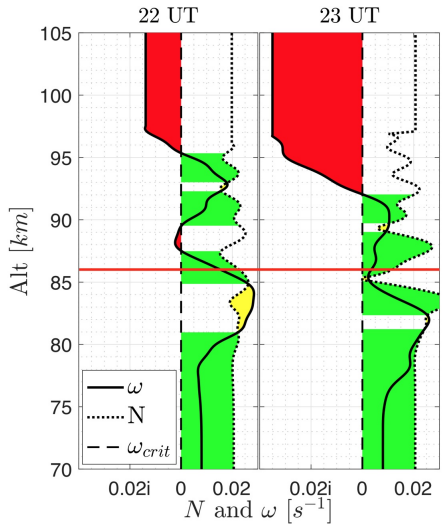

Figure 8.8: As in Figure 8.5 for the 30-minute averaged profiles at ∼22 UT and ∼23 UT. Temperature data from a single lidar beam is used in order to include the horizontally localized N values that occur at different altitudes in the lidar beams. The profiles reveal shear (∼22 UT) and convective (∼23 UT) instability conditions near the AMTM altitude.

$(\Delta z_{max}, \Delta z_{min}) = (300\ m, 30\ m)$. The vertical grid employs a stretch factor of $\gamma = 0.004$ symmetrically about the region of highest resolution at $z = 85\ km$. Simulation runs in Section 8.2.5 use a refined 3-D mesh employing $(Nx, Ny, Nz) = (512, 32, 1024)$ over the domain with a moderately enhanced stretch factor of $\gamma = 0.006$, yielding spanwise grid resolution of $\Delta y = 15\ m$ and $(\Delta z_{max}, \Delta z_{min}) = (400\ m, 14\ m)$ vertical grid resolution, with symmetrical stretching about the potentially turbulent regions at $z = 84\ km$.

8.2.1 Methodology

In order to evaluate the GW propagation dynamics observed in the AMTM and lidar, GWs are initialized with the parameters identified in the AMTM and allowed to propagate through the wind and temperature profiles from the lidar. The GW is initialized with a gaussian half-depth of 10 km centered at 50 km so it can propagate naturally up to the AMTM altitude. The wind profiles are extended down to 70 km by smoothing the lidar data to the local Saura winds. The initial GW parameters are $(\lambda_x,\ c_o,\ \omega_0) = (19\ km,$

$-15m/s$, $0.008 : 0.002 : 0.016s^{-1}$), where ω_0 is set by the background wind at 50 km. The wind and temperature profiles from the lidar and Saura data are fit together with a sum of sine function and implemented in the code in the manner described in Chapter 6. The initial GW amplitude is set to have perturbations of $\pm 8K$ at 80 km as observed by the lidar. GWs with all 5 ω_0 are simulated to propagate through each set of 7 hourly profiles, to simulate the evolving IGW background without requiring a wide enough domain to resolve the full IGW. Simulations are capped at 1 hour durations to analyze the general propagation characteristics of the GW over the event. As noted by Heale and Snively (2015), using 7 stationary background profiles to represent the IGW will diminish some of dynamics induced by the continuous movement of the IGW phases, but it enables higher domain resolution of $O(20m)$ to evaluate the evolution of fine scale features in the data. The simulations are primarily 2D, with the 3D spanwise domain extended to 0.5 km and LES only needed for the ∼22 to 23 UT simulations.

8.2.2 Event Overview

The phase structure of the simulated GWs is shown for $\omega_0 = 0.008s^{-1}$ and $\omega_0 = 0.016s^{-1}$ in Figures 8.9 and 8.10, respectively, for propagation through each of the hourly averaged background profiles from the lidar observations. Both GW frequencies show the same locations of critical levels ($\lambda_z \to 0$, near-horizontal phase lines) and evanescent regions ($\lambda_z \to \infty$, near-vertical phase lines) for each profile, verifying that the propagation dynamics are self-similar for the full range of likely GW frequencies in this event. At ∼19 UT and ∼20 UT, both simulation results show critical level filtering below the AMTM, confirming that the GW should not be visible in the AMTM at these times. At all other times, the GW appears to continue propagating through the AMTM altitude until it is filtered out by the descending region of negative shear corresponding to the -U phase of the IGW. The phase structure at ∼21 UT shows the GW in an evanescent region at the AMTM, with higher amplitudes above and below that match the filtered lidar observations. From ∼21

to 25 UT, the GW reaches AMTM altitudes, despite the AMTM showing only small-scale features spread throughout the domain at ∼22 UT and ∼23 UT. Since simulations through the hourly averaged profiles at ∼22 UT and ∼23 UT do not show any of the small-scale features observed in the AMTM, simulations initialized with the profiles from Figure 8.8 are used for direct comparisons with the observational data (see next section). Since the lidar data also shows a continuous GW signature from ∼22 to 23 UT, it is possible that the features observed in the AMTM could be advecting through the domain such that they obscure, rather than prevents, GW propagation at these times. This possibility will be discussed more below.

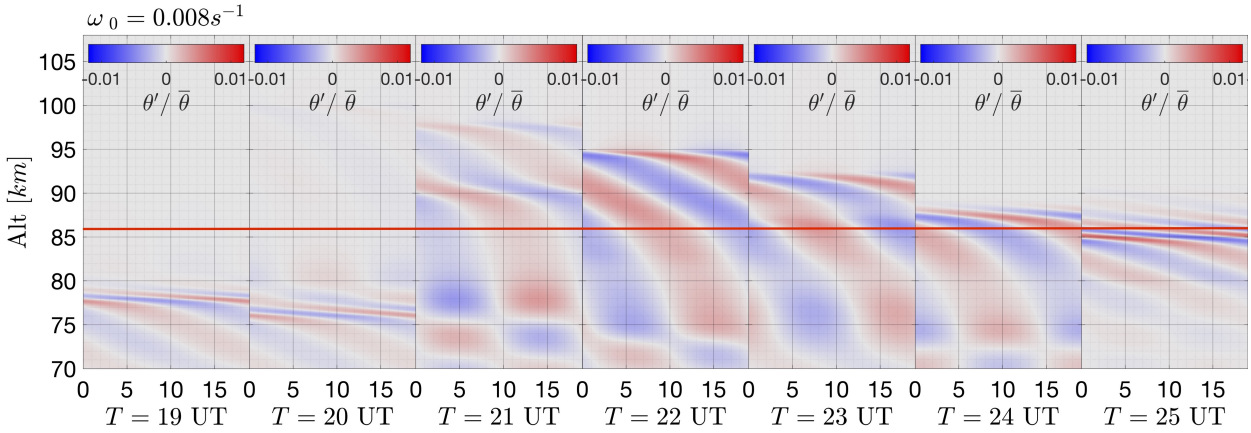

Figure 8.9: Simulated $\theta'/\overline{\theta}$ fields showing how the GW phase structure varies with altitude for a GW initialized with $\omega_0 = 0.008s^{-1}$ when propagating through the lidar wind and temperature profiles. Simulations indicate that a GW with the characteristics observed at ∼21 UT should be able to reach AMTM altitudes from ∼21 to 25 UT.

Figure 8.11 shows the $\theta'/\overline{\theta}$ fields for all five ω at the same elapsed time for the ∼21 UT profile simulations. GWs with all five ω_0 produce the same altitude-dependent evanescent regions and critical levels, but distinguish themselves in several important ways. Higher frequency GWs have higher amplitude temperature perturbations and more energy buildup at critical layers. This accelerates the progression of tunneling through the evanescent region around 80 km, produces a larger amplitude at 90 km at earlier times, and hastens the development of reflection at the bottom of the evanescent region near 70 km, which eventually

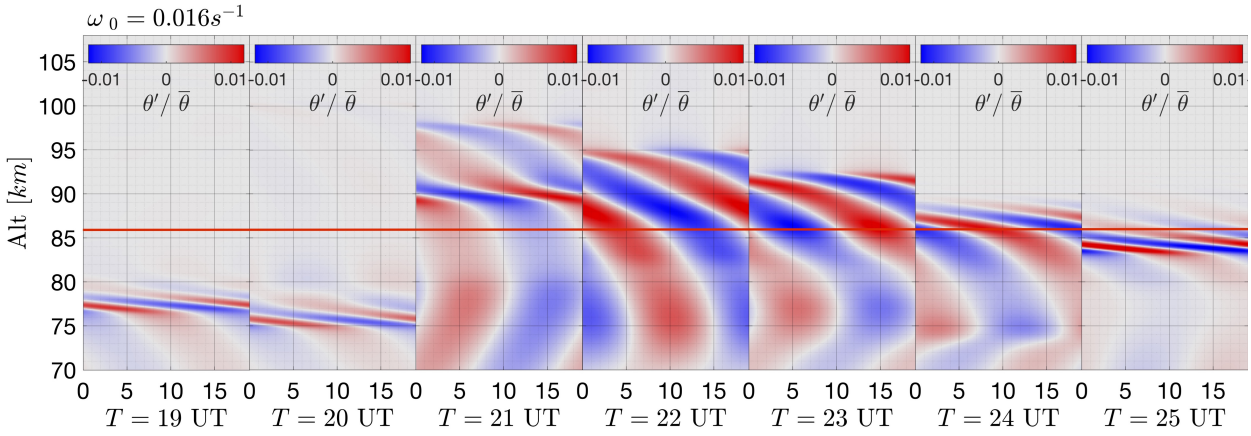

Figure 8.10: As in Figure 8.9 for a GW initialized with $\omega_0 = 0.016s^{-1}$. Similarities with Figure 8.9 indicate consistent altitude-dependent propagation characteristics for the full range of tested GW ω_0 values, with higher amplitudes producing sharper vertical gradients at higher ω_0 that could generate instabilities.

occurs for smaller ω_0 at later times. As a consequence of their larger amplitudes, higher-ω_0 GWs produce larger vertical gradients of temperature and wind in regions where the background sharply changes, resulting in lower local Ri that increase the likelihood of instability formation in these regions. If the GWs are the source of the small-scale features observed in the AMTM from ~22 to 23 UT, the GW ω_0 is more likely closer to $0.016s^{-1}$ than $0.008s^{-1}$.

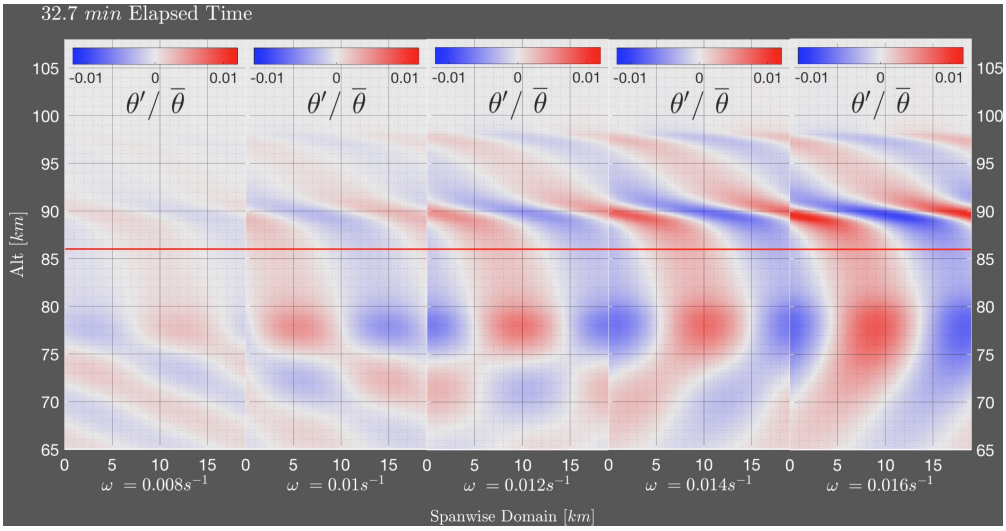

Figure 8.11: $\theta'/\bar{\theta}$ GW phase structure shown at the same elapsed simulation time for all five ω_0 GWs propagating through the ~21 UT lidar profiles. Larger ω_0 GWs develop reflection at earlier times and have higher amplitude buildup below evanescent regions.

A side-by-side comparison of the lidar-derived ω and N evolution, the simulation results, and the AMTM and lidar observations will now be shown in the time-regions outlined by the event observations to diagnose GW behavior at each stage in the event.

8.2.3 19 to 20 UT: Filtering

The simulated and observed GW parameters for ∼19 UT and ∼20 UT are shown in Figures 8.12 and 8.13, respectively, including lidar-derived ω and N profiles (left panel), $\theta'/\overline{\theta}$ phase structure for the simulated GW with $\omega_0 = 0.008s^{-1}$ and $0.016s^{-1}$ (middle panel), and the AMTM observations (right panel). At ∼19 UT, the critical level visible in the lidar profiles cuts off GW propagation above 79 km such that the simulated GW does not reach AMTM altitudes. By ∼20 UT, the critical level has diminished, allowing partial GW transmission into the evanescent region at later times in the simulation. AMTM observations show scattered small-scale features but no sign of GW activity, agreeing with the predicted dynamics from the simulation.

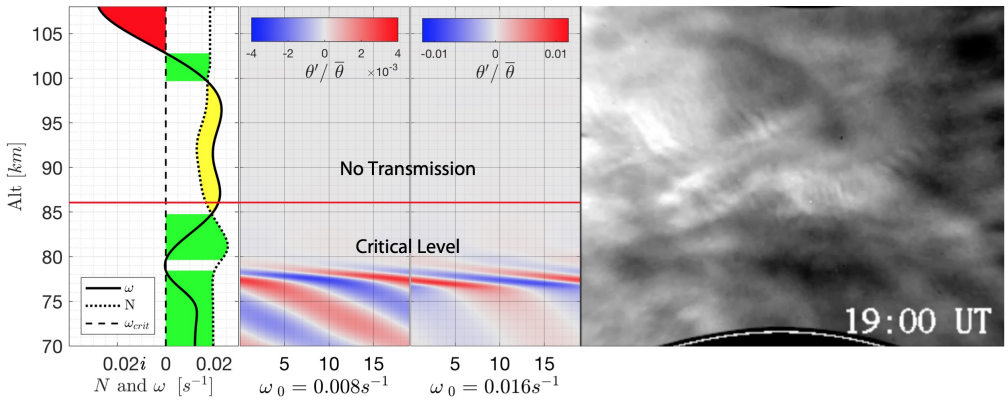

Figure 8.12: ω regimes at ∼19 UT showing propagation (green), evanescence (yellow), and $\omega < 0$ (red); simulated $\theta'/\overline{\theta}$ fields showing no GW transmission through critical level; and AMTM intensity.

8.2.4 21 UT: Propagation

The simulated and observed GW parameters for ∼21 UT are shown in Figure 8.14, including lidar-derived ω and N profiles (panel 1), $\theta'/\overline{\theta}$ phase structure for the simulated

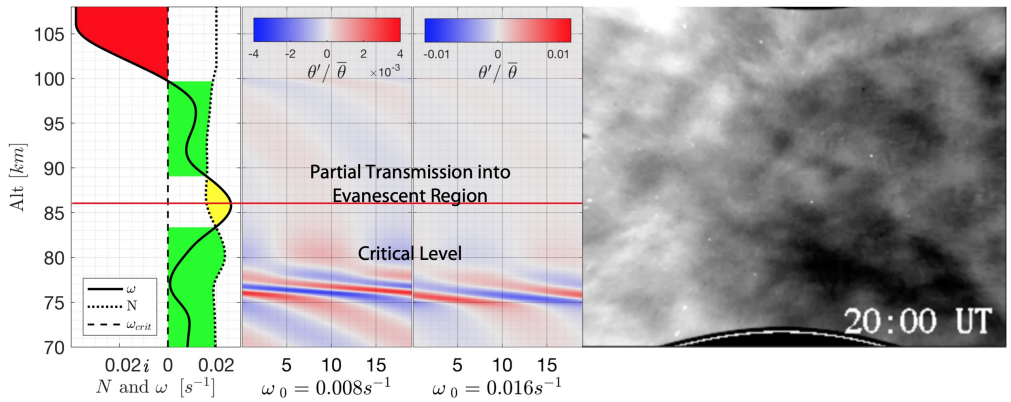

Figure 8.13: As in Figure 8.12 for ∼20 UT. Simulated $\theta'/\overline{\theta}$ fields indicate partial transmission of GW energy through the critical level at later times, with no coherent GW phase structure visible in the AMTM.

GW with $\omega_0 = 0.008s^{-1}$ and $0.016s^{-1}$ (panels 2 and 3), the filtered lidar temperature fields (panel 4), and the AMTM observations (panel 5). Here the coherent GW phase structure is visible in the AMTM where the lidar profiles identify an evanescent region. For both low and high ω_0, the GW tunnels through the evanescent region, accumulating amplitude at the near-critical level at 90 km before experiencing critical level filtering at 98 km. At later times, GW reflection occurs at the bottom of the evanescent region as most of the GW amplitude has passed through. Lidar temperature fields show the same higher amplitude regions occur near ∼80 km and 94 km, and the phase structure matches that of the simulation, indicating that the propagation dynamics are well-captured by the simulation parameters.

Figure 8.15 shows the vertical flux of the horizontal momentum, $-< u'w' >$, for both low and high ω_0. Both simulations show similar patterns of propagation behavior, with reflection at the bottom of the evanescent region occurring shortly after tunneling and a slight delay before the GW can propagate through the near-critical level at 90 km. Doubling the frequency results in an approximate 2x increase in vertical group velocities, with the GW producing the same behavior in roughly half the time for the high frequency case. The increased momentum flux (and corresponding GW perturbation amplitudes) above and below the evanescent region are confirmed by the filtered lidar perturbations in Figure 8.14.

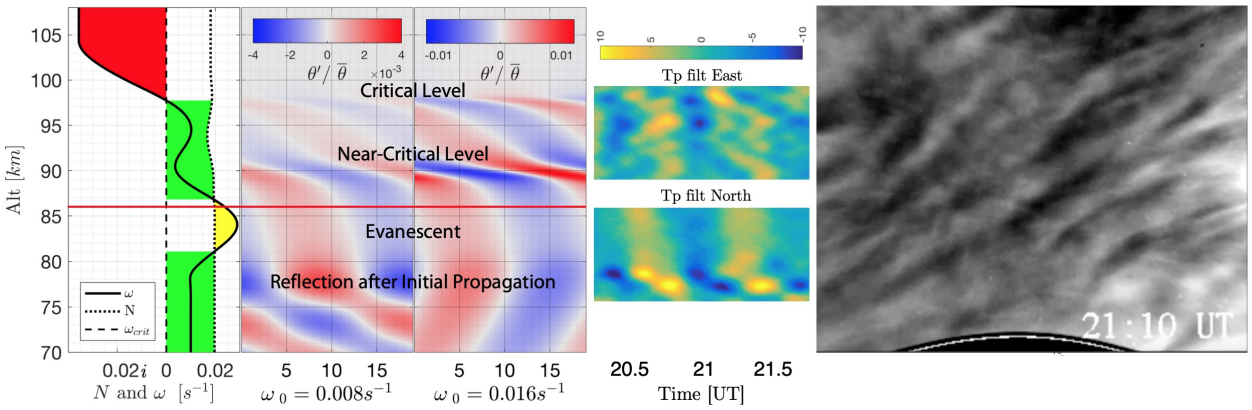

Figure 8.14: ω regimes at ~21 UT showing propagation (green), evanescence (yellow), and $\omega < 0$ (red); simulated $\theta'/\overline{\theta}$ fields showing no GW transmission through the critical level; filtered lidar temperature perturbations; and AMTM intensity. $\theta'/\overline{\theta}$ fields from the simulations and lidar data show GW tunneling through the evanescent region at AMTM altitudes, with phase structure showing propagation above and below the evanescent region.

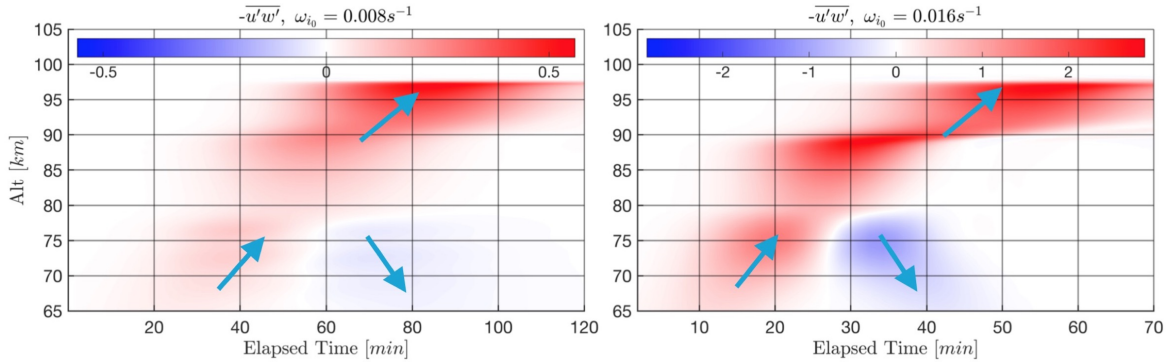

Figure 8.15: GW momentum flux divided by density for low and high ω_0, showing indications of tunneling and reflection at the evanescent layer.

8.2.5 22 to 23 UT: Instabilities

The simulated and observed GW parameters for ~22 UT and ~23 UT are shown in Figures 8.16 and 8.17, respectively, including lidar-derived ω and N profiles (panel 1), $\theta'/\overline{\theta}$ phase structure for the simulated GW with $\omega_0 = 0.008s^{-1}$ (panel 2), the vorticity for $\omega_0 = 0.016s^{-1}$ (panel 3), the filtered lidar temperature fields (panel 4), and the AMTM observations (panel 5). ω profiles obtained from the 30-minute averaged background profiles show a narrow altitude range of strong negative shear (indicated by decreasing ω) between an evanescent region ($\omega > N$, 81 to 84 km) and a critical level ($\omega \to 0$, 87.5 km). For the

$\omega_0 = 0.016s^{-1}$ simulation, the amplitude accumulation in this region, immediately below the critical level, generates Kelvin Helmholtz instabilities with prolonged GW propagation, providing one potential explanation for the instabilities seen in the AMTM at this time. At ~23 UT, weak instabilities only form for the largest $\omega_0 = 0.016s^{-1}$ below the mixing region with near-uniform density ($N^2 \rightarrow 0$) at 85 km. Little of the GW amplitude is able to tunnel through the $N^2 = 0$ region until much later times in the simulations, such that this region of $N^2 = 0$ could locally reduce the appearance of the GW in the AMTM. The thin evanescent layer below generates GW reflection, so this could also reduce the GW presence at the AMTM altitude. In the lidar data, higher GW amplitudes are observed from 84 to 85 km immediately below the layer suggesting a building of GW amplitude below the evanescent region, yet none of these behaviors explain the small-scale features observed in the AMTM at this time.

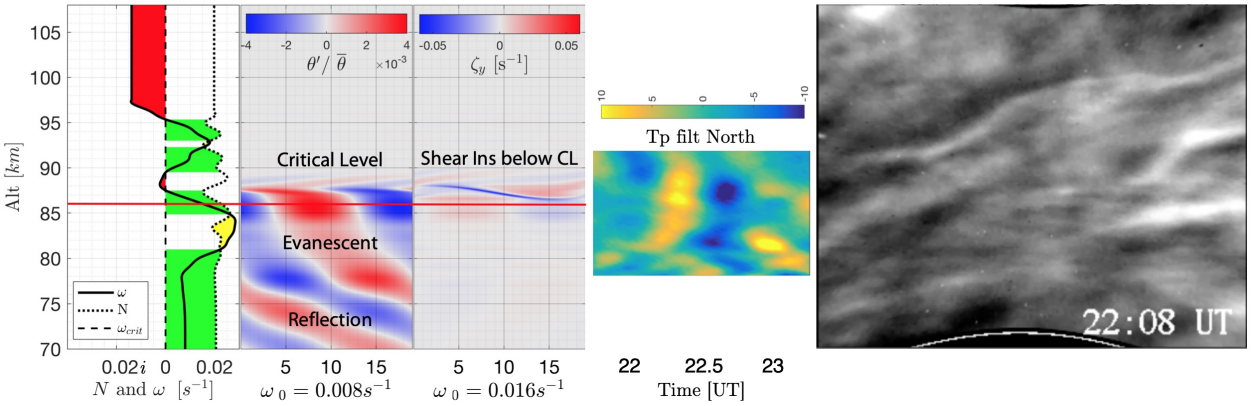

Figure 8.16: As in Figure 8.14 for ~22 UT. Simulated $\theta'/\overline{\theta}$ fields indicate a critical level below 90 km, while vorticity (ζ_y) shows the potential for shear instability formation at later times with larger initial ω. The obscured GW in the AMTM indicates instability formation.

Upon evaluating the behavior of the simulated and observed GWs from ~22 to 23 UT, it seems unlikely the GW is producing the instability features observed in the AMTM for several reasons: 1) The observed instability features occur in multiple orientations that do not align with the direction of GW propagation as would be expected for KHI formed by the GW. 2) The instability features span the entire AMTM field of view, whereas the

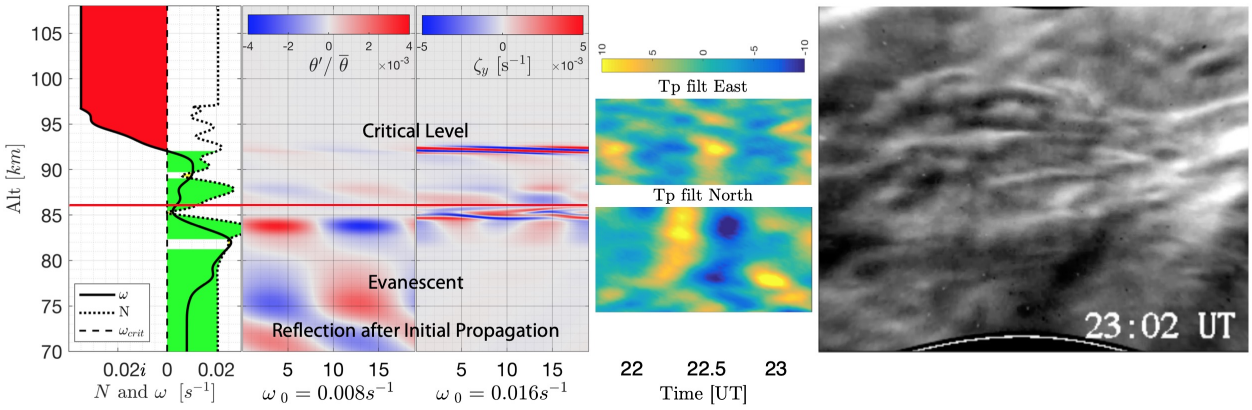

Figure 8.17: As in Figure 8.14 for ~23 UT. AMTM intensity shows EW-aligned instabilities at at 86 km where the lidar has heightened T' amplitudes. Simulated $\theta'/\overline{\theta}$ fields show the potential for instability development at 86 km where $N^2 \rightarrow 0$.

lidar profiles show instability conditions that are sufficiently localized to disagree between the two beams, which are ~80 km apart. Such local instabilities would not form coherent structures large enough to span the full AMTM domain. 3) Instability features from ~22 to 23 UT move to the east across the AMTM with time, such that they appear to be advected by the background wind rather than propagating in this direction. 4) Filtered lidar observations show no intermittency in GW propagation, and simulations through the average lidar profiles from these times suggest that the GW is likely able to propagate up through this region to the critical layer imposed by the IGW at higher altitudes. Despite the potential for localized shear and convective instabilities to form at these times near 86 km, the alignment and propagation of AMTM instabilities suggest the instabilities are advecting through the AMTM domain rather than being generated by the GW.

8.2.6 24 to 25 UT: Propagation

The simulated and observed GW parameters for ~24 to 25 UT are shown in Figure 8.18 for ~24 UT and Figure 8.19 for ~25 UT, including lidar-derived ω and N profiles (panel 1), $\theta'/\overline{\theta}$ phase structure for the simulated GW with $\omega_0 = 0.008s^{-1}$ and $0.016s^{-1}$ (panels 2 to 3), the filtered lidar temperature fields (panel 4), and the AMTM observations (panel

5). At ∼24 UT, the GW is observed in AMTM with the same orientation, λ_x, and c as the GW observed at ∼21 UT. The GW amplitude is reduced in the evanescent region from 77 to 81 km, but the GW is able to tunnel through the evanescent region and exhibit larger amplitude above at the AMTM altitude just below the critical level. These characteristics are also observed in the filtered lidar perturbations, which exhibit higher amplitudes near 80 km and 84 km corresponding to reflection below the evanescent region and amplitude build up below the descending critical level. The critical level just above the AMTM reduces GW amplitudes above 86 km, but the reduced N^2 peak below the AMTM at ∼25 UT also raises the GW amplitude at the AMTM, producing less reflection that enables more of the GW to reach the AMTM. The similarity to GW characteristics observed at ∼21 UT suggests that the GW source is continuous from ∼21 to 25 UT, making advection (rather than GW generation) the most likely source of the small-scale features observed from ∼22 to 23 UT.

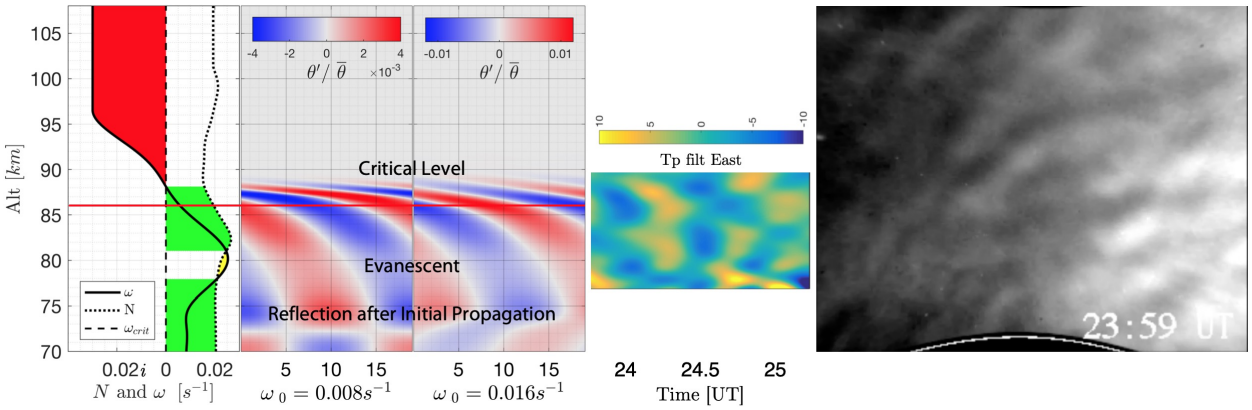

Figure 8.18: As in Figure 8.14 for ∼24 UT. Simulated $\theta'/\overline{\theta}$ fields indicate propagation up to a critical level above the OH layer where the GW is visible in the AMTM. GW characteristics in the AMTM match observations from ∼21 UT.

8.3 Summary

Results presented here utilize numerical simulations to describe intermittent GW propagation through an IGW, a 7 hour event observed by AMTM and lidar instruments over ALOMAR, Norway. Complexities in the GW and environmental evolution lead to dynam-

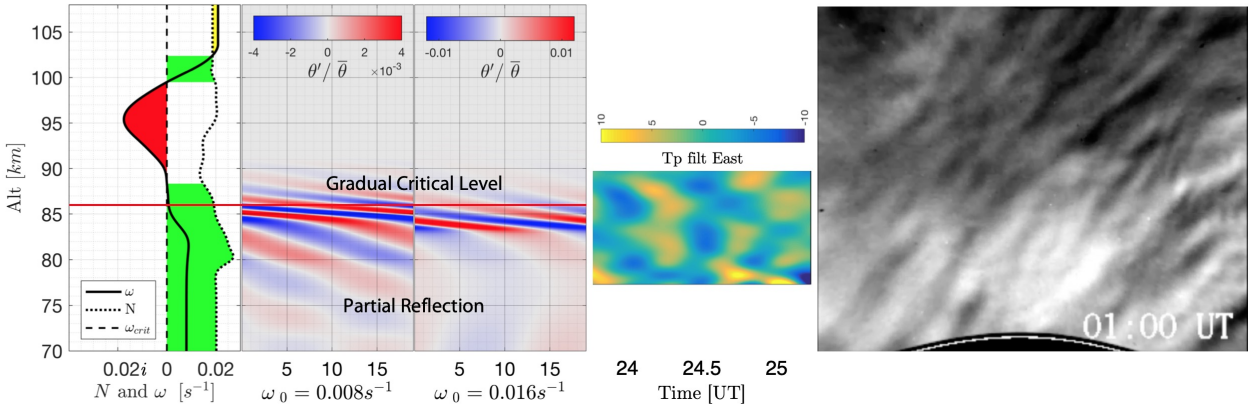

Figure 8.19: As in Figure 8.14 for ∼25 UT. The expanding critical level reduces $\theta'/\overline{\theta}$ amplitudes at the AMTM altitude. AMTM intensity shows the GW signature slowly diminishing.

ical discrepancies between lidar and AMTM observations, where the AMTM observes GW propagation above a lidar-identified evanescent region that should reflect the GW, and the AMTM observes a 2 hour gap in GW propagation at times when the lidar observes continuous propagation. Combining the GW and background characteristics from AMTM and lidar observations, the anelastic model simulates the GW propagating through hourly background profiles over the event to determine the dynamics behind the observational discrepancies.

Combining the propagating GW parameters observed in the AMTM and the IGW background characteristics observed in the lidar profiles, the expected propagation characteristics for the GW can be analyzed over the full event duration. N and ω profiles indicate a critical level below the AMTM at ∼19 UT and ∼20 UT that prevents the GW from reaching the AMTM. The profiles also indicate deep evanescent regions below the AMTM from ∼20 to 22 UT and at ∼24 UT, in addition to a narrow evanescent region at ∼23 UT. Linear ray-tracing methods indicate that all of these evanescent regions should reflect the GW and prevent propagation up to the AMTM altitude. N and ω only indicate linear propagation characteristics up to the AMTM at ∼25 UT. Ri profiles from the lidar also show conditions promoting localized instabilities at the AMTM altitudes from ∼22 to 23 UT.

Comparing filtered lidar wind and temperature profiles with AMTM observations, the

observed GW propagation characteristics do not agree with the expected characteristics from the background profiles. GW propagation is observed in the AMTM at ∼21 UT and ∼24 to 25 UT, whereas N and ω profiles only support linear propagation characteristics up to the AMTM at ∼25 UT. Filtered lidar data shows continuous GW propagation from ∼21 to ∼25 UT, with phase structure and amplitude variations indicating tunneling through evanescent regions at various times throughout the event.

Nonlinear simulations of GW propagation through lidar background profiles identify the most likely explanations for the dynamics observed at each time. Simulations at ∼19 UT and ∼20 UT confirm that critical level filtering prevents the GW from reaching the AMTM. ∼21 UT simulations confirm that the GW tunnels through the evanescent layer to reach the AMTM, showing that lidar phase structure and amplitude variations are consistent with the behavior of the simulations. ∼22 UT and ∼23 UT simulations through hourly-averaged profiles indicate that GW propagation up to the AMTM should continue, though simulations through the 30 minute averaged profiles also confirm the potential for local instabilities. These behaviors support the lidar observations but do not reproduce the widespread turbulence seen in the AMTM, suggesting that the observed small-scale features must be advecting through the domain rather than being generated by the GW. Simulations at ∼24 UT and ∼25 UT confirm the continued propagation of the GW up to the domain where it is observed in both instruments.

Chapter 9

Gravity Wave-Fine Structure (GW-FS) Interactions Modeled with Resolution Constraints

This Chapter presents a simulation study evaluating the behavior of GW-FS interactions modeled with resolution constraints. Using Case 6 from Chapter 7 as a well-resolved baseline case, simulations of the same GW and background profiles are run with the resolution scaled back from a minimum grid spacing of 15 m in the baseline case to 45 m, 200 m, and 2000 m, roughly the highest horizontal grid resolution used in nested regions of current mesoscale models such as those used in support of the DEEPWAVE campaign. Two viscosity levels are employed at each reduced resolution to evaluate Re implications and facilitate comparisons with mesoscale models. The goal of this study is to evaluate which parameters are affected by reduced model fidelity and determine what, if any, relationships exist between parameter evolution and both resolution and Re. The study also demonstrates the extent to which poorly resolved models cannot characterize GW-FS interactions, making a strong case for the use of better-resolved models and the inclusion of GW-FS parameterizations in regions where such events are likely to occur.

Unlike most mesoscale models, the anelastic model used for these simulations is energy-conserving and contains no artificial dissipation. As a consequence, under-resolved simulations with the anelastic code can produce artificial responses near the Nyquist frequency that would be damped out by numerical dissipation in other models. Once the flow is turbulent, numerical artifacts are addressed by the LES implementation, but at earlier transitional

stages, artifacts can lead to inconsistencies with mesoscale model runs at comparable resolutions that limit the utility of a comparison. The raised viscosity simulations at each resolution seek to address this potential discrepancy - the viscosity is raised for each under-resolved simulation to an empirically-determined level that curtails the development of numerical artifacts, making a rough approximation of the dynamics that would be observed in mesoscale models that employ numerical dissipation at comparable resolutions. Raised viscosity is a somewhat primitive approximation for a numerical dissipation scheme, as modern implementations of essentially non-oscillatory (ENO) and weighted ENO (WENO) dissipation schemes target oscillatory artifacts with a high degree of precision (see e.g., Harten et al., 1987; Shu and Osher, 1988; Jiang and Shu, 1996). However, the methodology is adequate for the purposes of this analysis. Having higher viscosity also reduces Re, adding an additional constraint that can be evaluated for each resolution.

The Chapter is organized as follows: The physical parameters employed in this study are defined in Section 9.1. Section 9.2 examines the deterioration of the primary vortical and baroclinic source features in the initial instability evolution. Section 9.3 evaluates the behaviors of peak amplitudes for parameters defined by coherent GW propagation (9.3.1) and parameters defined by spatial gradients that characterize fine structures and instabilities (9.3.2). Section 9.4 presents the large-scale implications to the induced winds and the extrapolated parameter relationships with resolution. A summary of the findings and their implications is given in Section 9.5.

9.1 Parameter Definitions

As in Chapter 7, the model domain extends 20 km (one GW λ_x) in the streamwise (x) direction, 1 km in the spanwise (y) direction, and from 20 to 105 km in altitude (z). The domain employs periodic horizontal boundary conditions and a 15 km sponge layer at the top of the vertical domain, capping the useable domain at $z = 90\ km$. The code is executed on Department of Defense high performance supercomputers employing the grid

configurations described in Chapter 6.5, having constant streamwise and spanwise resolution in each case and the $\gamma = 0.001$ stretched vertical mesh of Chapter 7 surrounding a region of constant grid spacing at 80 km.

All simulations are initialized with the GW parameters described in Chapter 7.1 and background profiles for Case 6 as described in Table 7.1. The grid spacing, viscosity, and imposed Re characteristics for the simulations in this study are shown in Table 9.1, where $(\nu_{turb}, Re_{turb}) = (2.3, 5 \times 10^5)$ as in Chapter 7. 15 m grid resolution was selected for a baseline case in favor of the variable (x, y, z) grid spacing used in Chapter 7, matching the weakest grid spacing constraint in all 3 dimensions to facilitate easier comparison with under-resolved cases. The viscosity enhancements in Cases 3, 5, and 7 were determined through a series of trials as the lowest viscosity needed to suppress numerical artifacts introduced with each resolution decrease from the 15 m baseline case. With the simulations setup in this manner, comparing Cases 2, 4, and 6 with Case 1 identifies changes to the parameter evolution as a function of reduced resolution, while comparing Cases 3, 5, and 7 with Case 1 identifies changes to the parameter behaviors that would be observed by comparable mesoscale models with numerical dissipation. A comparison of cases at the same resolution (Cases 3, 5, and 7 relative to Cases 2, 4, and 6, respectively) identifies parameter behaviors that change as a function of reduced Re.

Table 9.1: Background Parameters for Each Case

Case	Δx_i $[m]$	ν $[m^2 s^{-1}]$	$\rightarrow Re$
1	15	ν_{turb}	Re_{turb}
2	45	ν_{turb}	Re_{turb}
3	45	$30\nu_{turb}$	$Re_{turb}/30$
4	200	ν_{turb}	Re_{turb}
5	200	$100\nu_{turb}$	$Re_{turb}/100$
6	2000	ν_{turb}	Re_{turb}
7	2000	$1000\nu_{turb}$	$Re_{turb}/1000$

9.2 Cases 1 to 5: Instability Evolution and Vortical Deterioration

The vortical evolution of the flow and the corresponding evolution of baroclinic sources and sinks reveal the consequences of reduced resolution and Re that develop for each FS case. Figure 9.1 shows the initial FS layer evolutions in the spanwise vorticity (ζ_y) fields for Cases 1 to 5, and Figure 9.2 shows the corresponding baroclinic vorticity source ($\frac{1}{\rho^2}\left(\nabla\rho \times \nabla P\right)_y$) fields at the same times. Both figures employ translating horizontal domains centered on the main vortical structures to facilitate visual comparison. Note that plots from Cases 6 and 7 are omitted from these figures as their 2 km resolution breaks down the GW and FS structures after only a few time iterations. Cases 6 and 7 do, however, exhibit meaningful parameter amplitude relationships that are discussed below. Case 1 shows identical ζ_y feature evolution to Case 6 from Chapter 7 (See Figure 7.13), while Cases 2 to 5 show several distinct behaviors. Comparing Case 1 with Cases 2 and 4 (reduced resolution with the same ν_{turb}), numerical artifacts in Cases 2 and 4 appear as oscillatory behaviors expanding out from the rotated regions of the FS structure. These features initially occur at scales several times larger than the grid resolution, generating preferentially from features in the flow that have rotated from the initial orientation. Given that the initial FS includes an N^2 layer, the rotated regions have large horizontal θ' gradients and corresponding baroclinic sheets in Figure 9.2, suggesting that under-resolved dynamics related to baroclinic tendencies may give rise to these oscillations. In spite of the numerical noise present in the FS evolution, peak vorticity and baroclinic amplitudes in the FS region of Cases 2 and 4 remain roughly the same as Case 1 until $5T_B$. The increased viscosity simulations in Cases 3 and 5 remove the numerical artifacts present in Cases 2 and 4, with the consequence of significant amplitude reduction of the dominant vortical features. That the vortical and baroclinic amplitudes are more reduced in Case 5 relative to Case 3 further suggests a dynamical relationship between parameter amplitudes and resolution.

The ζ_y fields accompanying the initial vortex formation are shown for Cases 1 to 5 in

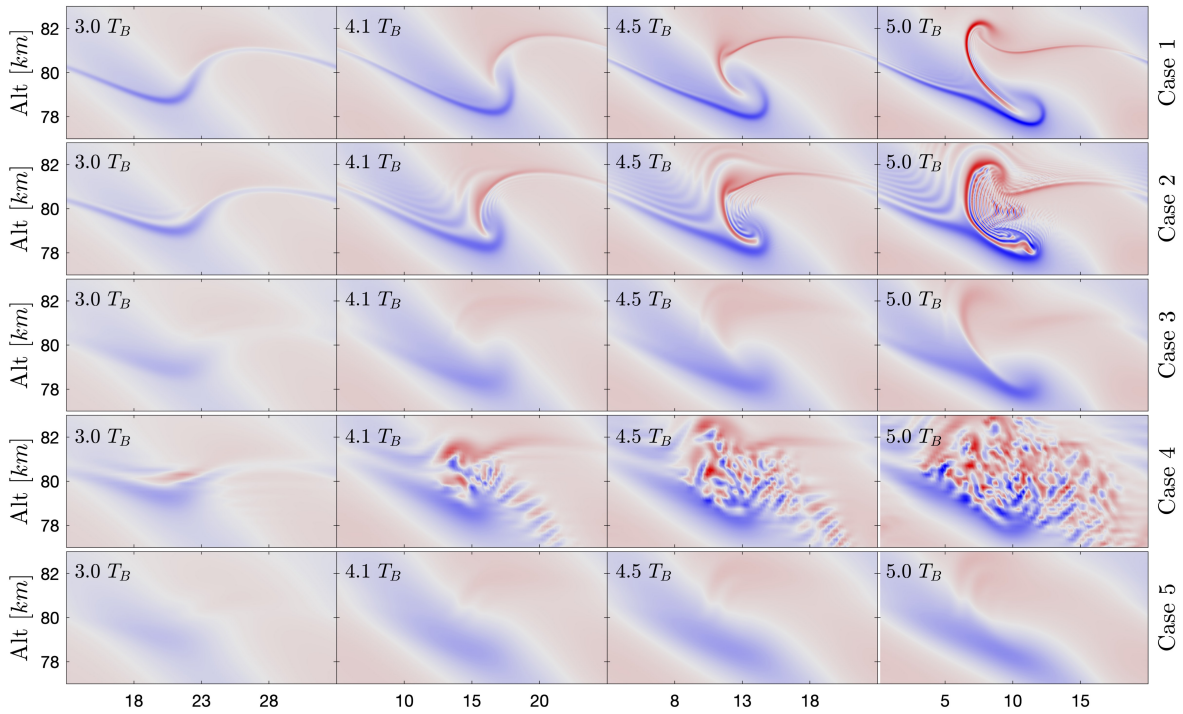

Figure 9.1: As in Figure 7.13 for Study 3 Cases 1 to 5. Under-resolved cases with baseline viscosity exhibit numerical artifacts, while under-resolved cases with enhanced viscosity suppress these artifacts with the added consequence of reduced ζ_y amplitudes.

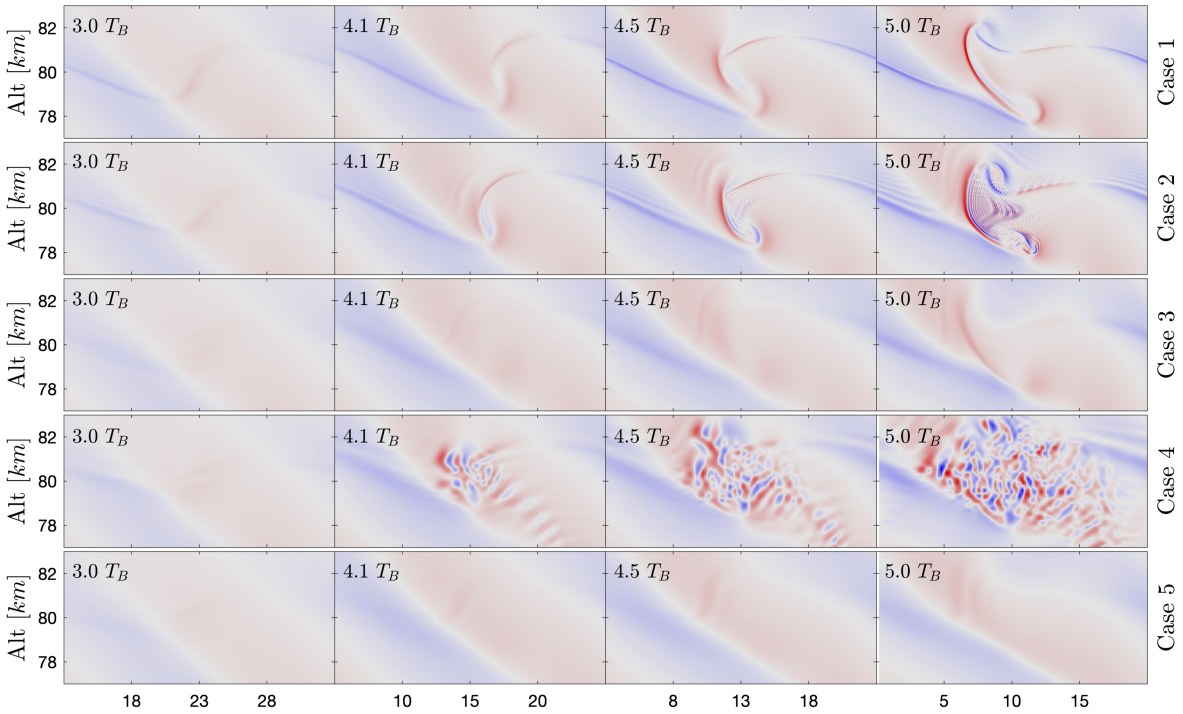

Figure 9.2: As in Figure 7.14 for Study 3 Cases 1 to 5.

Figure 9.3, at 1 minute increments. Case 2 reproduces both the larger vortex in the lower, negative ζ_y sheet, and the smaller vortices in the higher, positive ζ_y sheet exhibited in Case 1, but it also includes a significant degree of numerical noise that has increased in amplitude and decreased in scale from earlier times. Case 4 retains the shape of the large-scale vortical structure from the higher resolution simulations, but numerical artifacts preclude the coherent formation of either vortex structure present in the baseline case. Both Cases 2 and 4 exhibit reduced ζ_y amplitudes from those occurring in the smallest-scale vortical features of Case 1, suggesting that their reduced resolution is constraining ζ_y amplitudes and those of corresponding features in other affected fields.

Recalling from Chapter 7 that high vorticity amplitudes trigger the onset of instabilities, the reduced vorticity amplitudes in Cases 3 and 5 delay the formation of the initial vortices to later times than Cases 1, 2, and 4, producing altered instability dynamics as their large-scale vortical structures have evolved further in time when the initial instabilities form. Case 3 is able to reproduce the large, lower vortex but does not reproduce the smaller, positive ζ_y vortices forming at the same time in Case 1. With the delayed rollup of the initial negative ζ_y vortex, the large-scale vortical structure in Case 3 is wider and shallower than Case 1 when the initial vortex forms, altering the instability dynamics for the duration of the event. Case 5 delays the formation of the larger, negative ζ_y vortex out to $6.2T_B$, a full buoyancy period later than Case 1. By this time the main vortical structure has widened out and produced a shallower vortex than Cases 1 to 3, and the positive ζ_y sheet that forms smaller vortices in Cases 1 and 2 has dispersed and lost most of its coherence. Numerical artifacts also accompany the vortex formation in Case 5, even with viscosity increased over Case 1 by a factor of 100. The degradation of the vortical structures in Cases 2 to 5 indicates that at best, the primary instability evolution can be retained at a reduced resolution if numerical oscillations are allowed, but increasing the viscosity to approximate the behavior of numerical dissipation delays instability onsets and changes the environment in which the vortices form, rendering any resulting instability analysis unphysical.

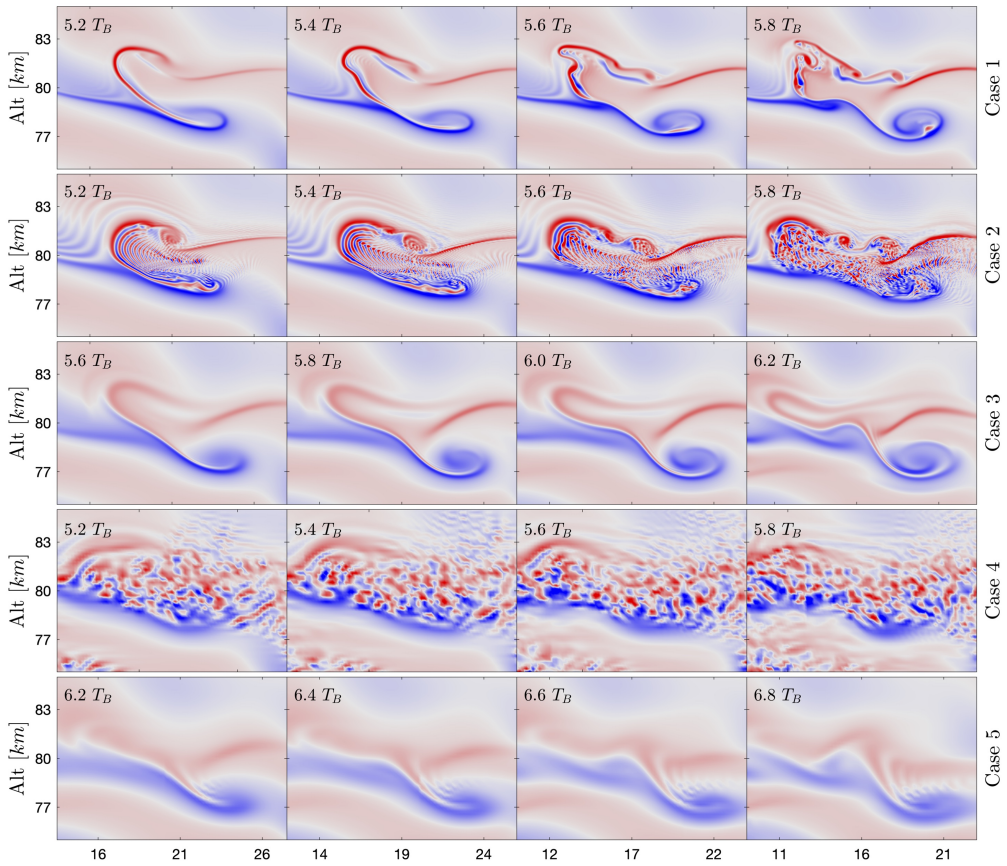

Figure 9.3: As in Figure 9.1 showing the initial instability evolution at 1 minute increments. Cases 2, 3, and 5 partially preserve the initial vortices of Case 1, while numerical artifacts in Case 4 preclude coherent vortex formation. Case 2 vortices evolve at the correct time but contain numerical artifacts, whereas Cases 3 and 5 have delayed vortex formation at times when the large-scale vortical structure has changed.

9.3 Parameter Amplitude Retention

The behavior of peak parameter amplitudes over the domain is presented to evaluate the dependency of physical parameters on resolution. The resolution and *Re* dependencies break down into two general classes of behavior: Parameters defined by coherent GW propagation, presented in Section 9.3.1, and gradient parameters related to FS and instabilities, presented in Section 9.3.2. Because Cases 6 and 7 are not able to fully resolve the GW, their analysis is omitted from Section 9.3.1.

9.3.1 GW-Determined Parameter Amplitudes

Physical parameters associated with coherent GW propagation exhibit distinctive Re and resolution dependent behaviors at time ranges corresponding with the dominant features of the flow. The evolution of peak amplitudes of u' and w' are shown in Figure 9.4, with the corresponding peak amplitudes of kinetic energy ($\frac{1}{2}[u'^2 + w'^2]$) and the vertical flux of horizontal momentum ($u'w'$) shown in Figure 9.5. The lower panels of each figure show the parameter amplitudes normalized by Case 1 values to indicate what percentage of Case 1 amplitudes are retained for each under-resolved case. From 0 to $3T_B$, the peak parameter amplitudes for Cases 1 to 5 are identical as the GW propagates up to the FS layer. As the initial instability evolution of the FS occurs, from ~ 3 to $7T_B$, the two under-resolved cases without increased viscosity (Cases 2 and 4) exhibit higher ($\sim 10\%$ to 100%) peak amplitudes than Case 1, as the amplitudes of the numerical artifacts overtake the amplitudes of the dominant physical features of the flow. Conversely, the two under-resolved cases with higher viscosity (Cases 3 and 5) exhibit lower ($\sim -10\%$ to -50%) peak amplitudes than Case 1, as the raised viscosity reduces the vortical consequences of the instability ramp up to the wind perturbations and corresponding fluxes and kinetic energy. The peak amplitudes of Cases 1 to 5 all reach their maximum value near ~ 7 to $8T_B$ when the dynamics become turbulent and progress to smaller spatial scales. From ~ 7 to $10T_B$, under-resolved cases have lower peak amplitudes than Case 1, but they converge on roughly the same amplitude at $10T_B$, indicating no conclusive Re or resolution dependent behavior of the final amplitudes of the GW-dependent parameters.

9.3.2 Gradient-Determined Parameter Amplitudes

The evolution of peak amplitudes of ζ_y and baroclinity are shown in Figure 9.6, with the corresponding peak amplitudes of local $\frac{\partial u}{\partial z}$ and N^2 shown in Figure 9.7. As in Figures 9.4 and 9.5, the lower panels are normalized by Case 1 values to indicate what percentage of

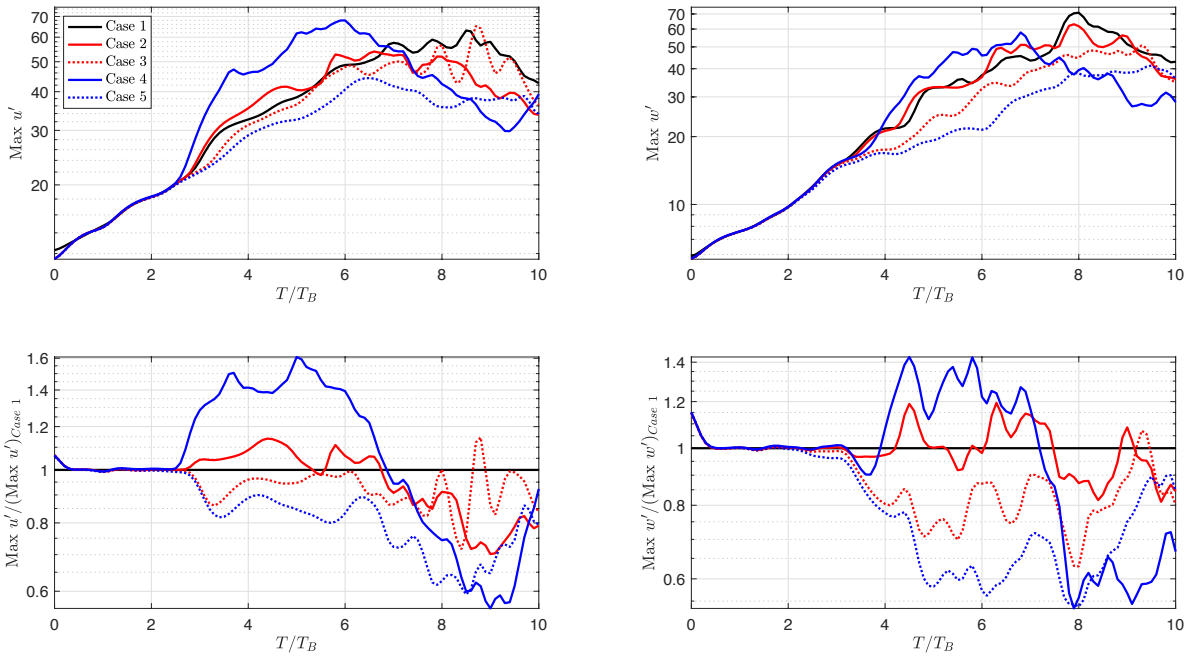

Figure 9.4: Time evolution of u' and w' peak amplitudes, presented as the original values in the top panels and normalized by Case 1 values in the bottom panels. Resolution and Re-dependent behaviors occur while the GW and FS remain coherent, with no significant variation in final peak parameter amplitudes.

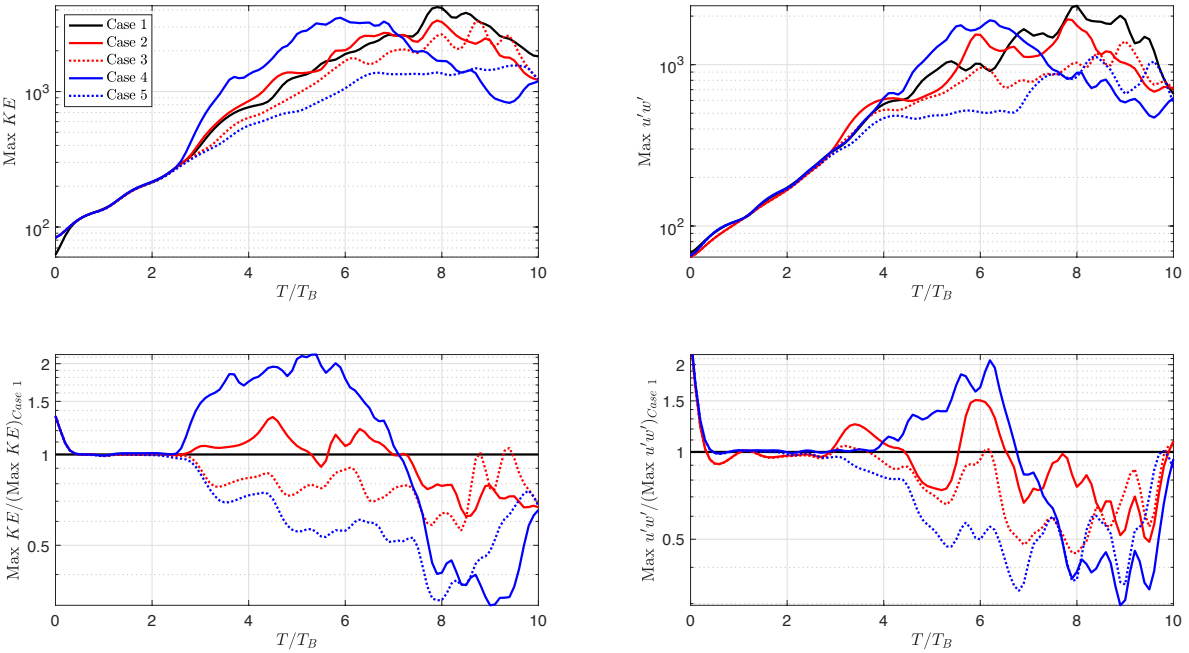

Figure 9.5: As in Figure 9.4 for kinetic energy ($\frac{1}{2}[u'^2 + w'^2]$) and the vertical flux of horizontal momentum ($u'w'$). Resolution and Re-dependent behaviors occur while the GW and FS remain coherent, with no significant variation in final peak parameter amplitudes.

Case 1 amplitudes are retained for each under-resolved case. Comparing Case 1 with all under-resolved cases, the peak amplitudes of all gradient-determined parameters markedly decrease as the resolution decreases, with amplitude reductions greater than two orders of magnitude in some cases. More under-resolved simulations reach their peak amplitudes at earlier times as the turbulent energy moves to the smallest scales resolved by the simulations. As each under-resolved case reaches its maximum parameter amplitude, parameter amplitudes in cases with higher resolution continue to increase with time until they plateau at their resolution-constrained peak value. Once the GW begins to influence the evolution of the FS (from $\sim 3T_B$ onward), cases with increased viscosity (Case 3 vs. Case 2, Case 5 vs. Case 4, Case 7 vs. Case 6) have lower peak amplitudes than the corresponding cases with baseline viscosity as their turbulent evolution is delayed. The increased viscosity cases do, however, reach the same peak parameter amplitudes as each baseline viscosity case with the same resolution, but they do so at later times, experiencing a delay corresponding to the delayed instability evolution seen in Figure 9.3. The peak amplitudes of gradient-determined parameters are thus determined by resolution, while the time required to reach those peak amplitudes at a given resolution increases as Re is decreased.

9.4 Induced Wind and Resolution Relationships

The peak induced wind (ΔU) amplitude at 80 km, the altitude of the FS imposed in the initial conditions, is shown in Figure 9.8 for Cases 1 to 5. As a feature generated by the divergence of the GW momentum flux, ΔU behavior largely matches the amplitude evolutions of the GW-induced characteristics discussed in Section 9.3.1, not showing significant decadal amplitude variations with resolution or viscosity-induced time delays. Data from Cases 6 and 7 are also excluded from this plot, as their behavior is unphysical since the GW is not properly resolved. From ~ 2 to $6T_B$, the induced wind at 80 km gradually increases with time, where under-resolved cases with baseline viscosity (Cases 2 and 4) have slightly higher ($\sim$ 5% and 10%) ΔU and cases with increased viscosity (Cases 3 and 5) exhibit

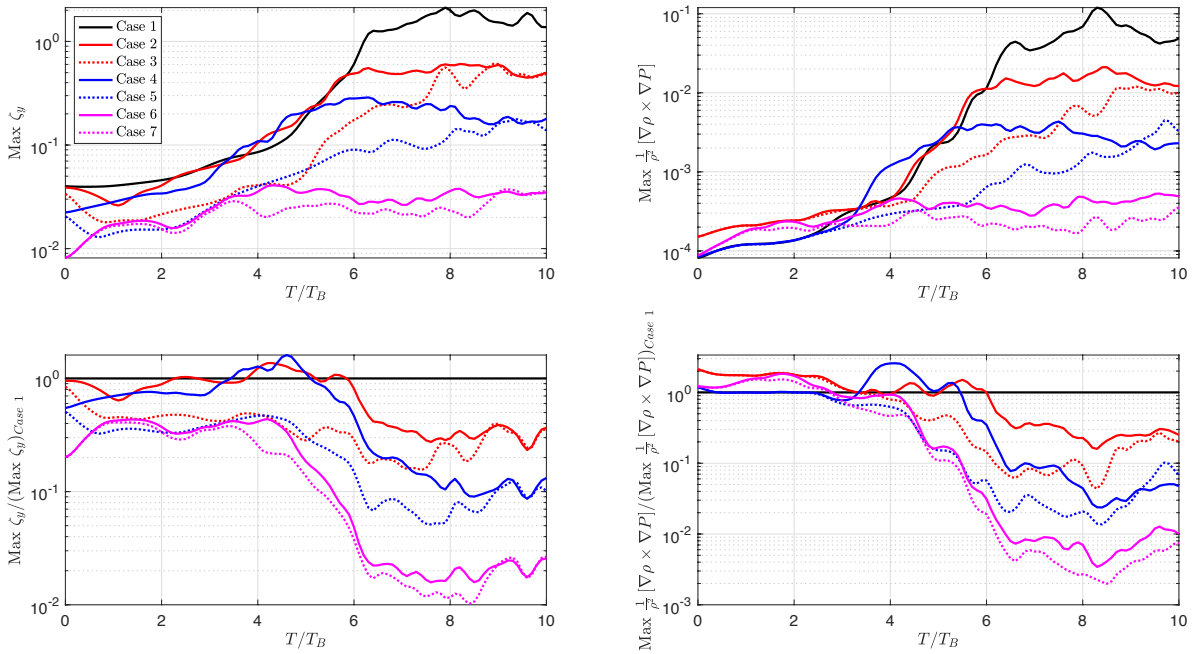

Figure 9.6: As in Figure 9.4 for ζ_y and $\frac{1}{\rho^2}\left(\nabla\rho\times\nabla P\right)_y$. Final peak amplitude values decrease with decreased resolution, while increased viscosity cases reach the same peak amplitude as the baseline viscosity cases for the their respective resolutions at later times.

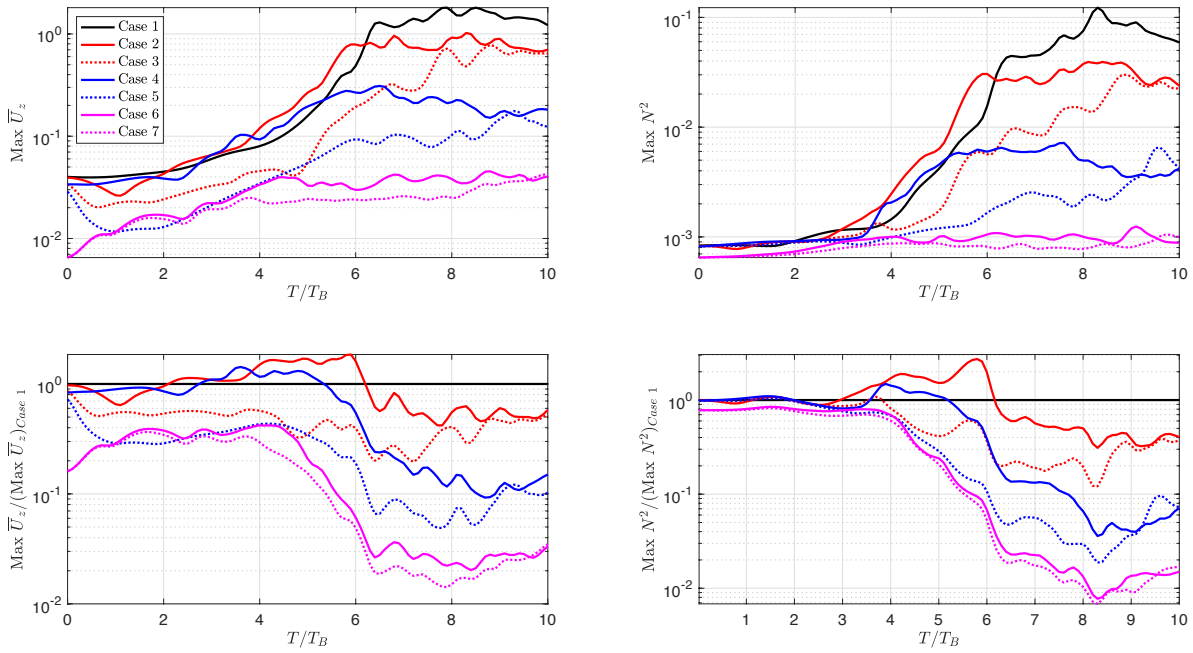

Figure 9.7: As in Figure 9.4 for $\overline{U}_z$ and N^2. Final peak amplitude values decrease with decreased resolution, while increased viscosity cases reach the same peak amplitude as the baseline viscosity cases for the their respective resolutions at later times.

slightly reduced ($\sim 5\%$ and 10%) ΔU relative to Case 1. Peak amplitude occurs at $\sim 6T_B$, roughly the same time as peak ζ_y, after which point the under-resolved cases do not vary significantly ($\pm 30\%$) from the induced wind amplitude in Case 1. The final induced wind profiles for all 7 cases are shown in Figures 9.9 at $10T_B$ as a waterfall plot in the left panel and overlaid together in the right panel. Cases 2 to 5 roughly capture the main ΔU feature at 80 km, while the 2 km grid resolution in Cases 6 and 7 does not show any distinguishable ΔU peak. Cases 2 and 4 both exhibit slightly increased ($\sim 5\%$ and 10%) ΔU amplitudes, while the increased viscosity cases at the same resolutions (Cases 3 and 5) show reduced amplitudes relative to Case 2 ($\sim -15\%$ for Case 3) and Case 4 ($\sim -9\%$ for Case 5). For the 200 m resolution cases, the viscosity-induced amplitude reduction yields the same peak ΔU as Case 1, while the enhanced viscosity case with 45 m resolution (Case 3) overcompensates and produces a lower peak ΔU than Case 1. While the depth of the induced wind feature in the 45 m resolution Cases (2 and 3) are roughly the same as Case 1, the 200 m resolution Cases (4 and 5) diminish the fidelity of the main induced wind feature, extending the depth by several kilometers and smoothing out the amplitude gradient.

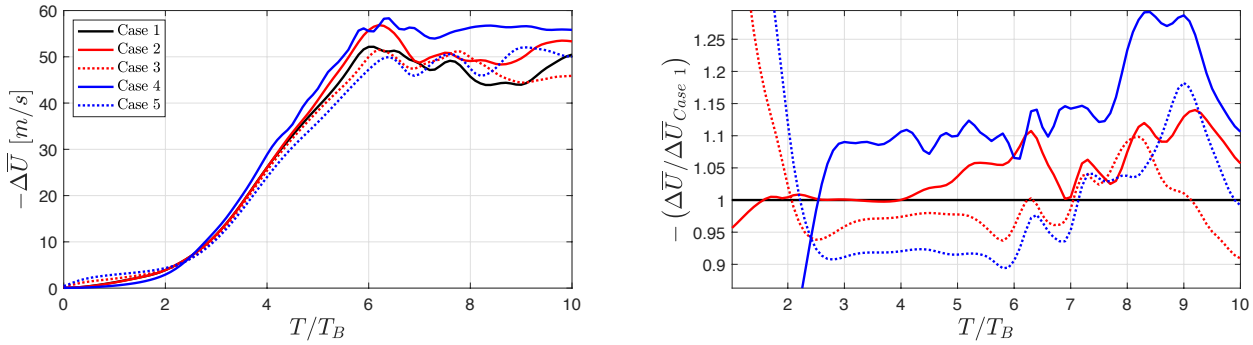

Figure 9.8: As in Figure 9.4 for $\Delta\overline{U}$. Resolution and Re-dependent behaviors occur while the GW and FS remain coherent, with no significant variation in final peak parameter amplitudes.

The resolution dependence of the gradient-determined parameter amplitudes is shown for under-resolved cases with baseline viscosity in Figure 9.10 and for under-resolved cases with enhanced viscosity in Figure 9.11, i.e. the expected observed relationship in models employing numerical viscosity. For each parameter, the final amplitude level is shown as a

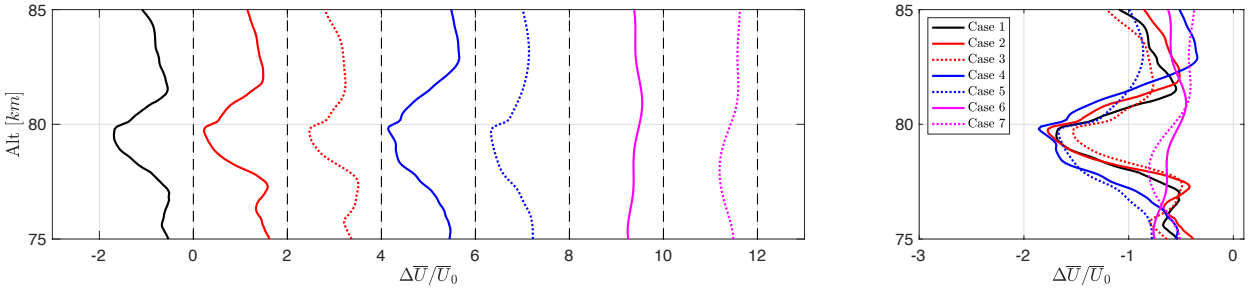

Figure 9.9: $\Delta\overline{U}$ Profiles from $10T_B$, shown as a waterfall plot in the left panel and overlaid in the right panel. Under-resolved Cases 2 to 5 roughly retain the shape and amplitude of the $\Delta\overline{U}$ peak, while Cases 6 and 7 are not able to resolve the $\Delta\overline{U}$ consequences of the GW-FS interaction.

percentage of the final level in Case 1, indicating the percent amplitude retention for each parameter for each case as a function of the resolution ratio ($\Delta x/\eta$, where η is the Kolmogorov length scale. See explanation in Section 7.1). The average percent amplitude retention of the four parameters is shown in red, with best-fit lines identified in the legend. The average amplitude retention in both comparisons has an approximate power-law dependence on the resolution ratio, taking the form $(4.4 \pm 2.5)(\Delta x/\eta)^{-.85\pm0.3}$ for the baseline viscosity comparison and $(5.3 \pm 2.7)(\Delta x/\eta)^{-.95\pm0.3}$ for the enhanced viscosity comparison. Given the general agreement of these parameter fits, it is likely that the observed power-law dependence of peak amplitudes of gradient-determined parameters on the imposed resolution ratio can be generalized to describe numerical simulations of GW-FS interactions undertaken by other models.

9.5 Summary

Results presented in this Chapter evaluate the dynamical consequences of modeling GW-FS interactions when the resolution is reduced below the grid spacing needed to fully characterize an event. Simulations representing the event conditions described in Chapter 7, Case 6 are carried out with minimum grid spacing of 15 m, 45 m, 200 m, and 2000 m to identify how the critical dynamics of the FS evolution and instability onset are altered by

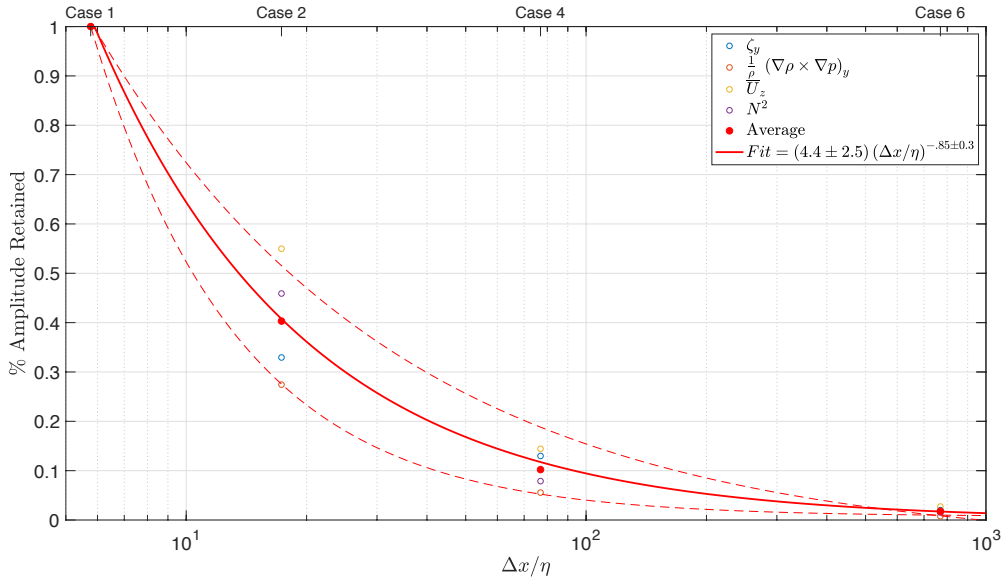

Figure 9.10: Percent retention of final parameter amplitude vs. resolution ratio ($\Delta x/\eta$) for Cases 2, 4, and 6 with baseline viscosity matching Case 1.

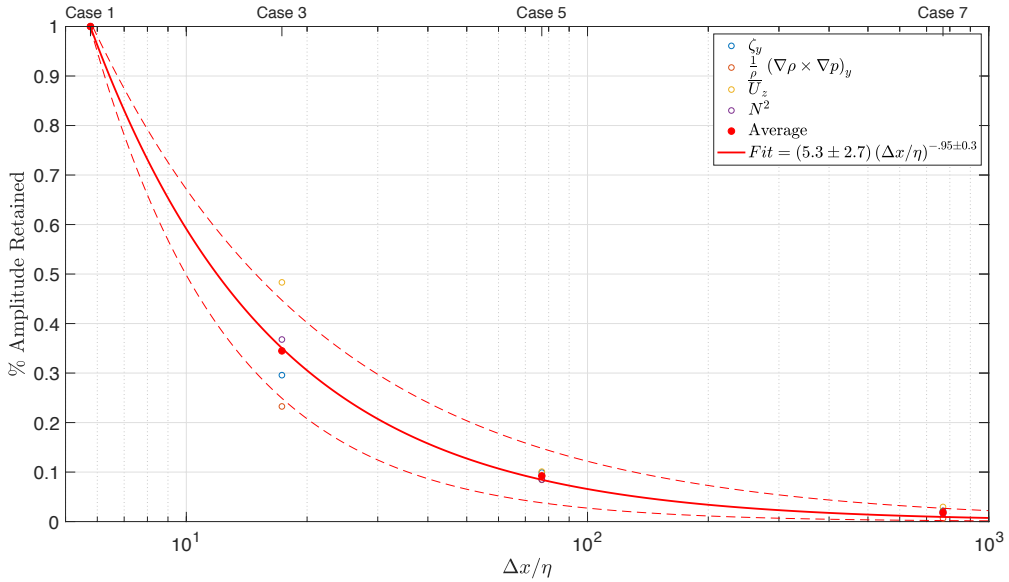

Figure 9.11: As in Figure 9.10 for Cases 3, 5, and 7, with heightened viscosity over Case 1, roughly approximating the behavior that would be observed by mesoscale models employing numerical dissipation.

reduced resolution. Raised viscosity simulations are also carried out at each under-resolved resolution to suppress the formation of numerical artifacts in a manner approximating the numerical dissipation implementations in mesoscale models.

The vorticity and solenoid fields depicting the initial instability evolution identify the breakdown of the dominant vortical characteristics as the resolution is constrained. Under-resolved simulations with baseline viscosity exhibit numerical *ringing* artifacts that develop from the prominent rotated region of the FS, indicating under-resolved baroclinic tendencies as the potential source of the oscillations. Reduced resolution simulations suppress the numerical artifacts seen at early times, but they also reduce vortical amplitudes of the FS that delay the onset of instability features seen in the baseline case. Case 2 is the only under-resolved case that retains both large and small initial vortices from Case 1, while numerical artifacts in Case 5 completely deteriorate the instability structures. Cases 3 and 5 are able to retain the larger of the two initial vortices, but the large scale has evolved to a different structure by the time the delayed instability onset occurs, rendering the results physically inconsistent with Case 1.

The peak amplitudes of GW-determined parameters exhibit resolution-dependent tendencies at times when the GW and FS evolution remain coherent, where decreased resolution simulations with baseline viscosity (Cases 2 and 4) proportionally increase peak amplitudes, and decreased resolution simulations with enhanced viscosity (Cases 3 and 5) proportionally decrease peak amplitudes. Gradient-determined peak parameter amplitudes decrease as a function of resolution, with Cases 2, 4, and 6 having peak amplitudes that increase at the same rate as Case 1 until they plateau at their resolution-determined maximum value. Peak amplitudes of gradient-determined parameters in Cases 3, 5, and 7 reach the same peak value as Cases 2, 4, and 6, respectively, but they do so at later times as their initial instability evolution is delayed by the viscous reduction of vortical amplitudes at early times.

Induced wind amplitudes behave in the same manner as GW-determined parameter amplitudes, having higher (lower) peak values for under-resolved simulations with baseline (increased) viscosity while the GW and FS remain coherent. The final peak induced wind is roughly the same for each case that can roughly resolve the FS, whereas Cases with 2 km grid spacing are unable to replicate the induced wind behavior. Cases 2 to 5 show only mild

deformation of the induced wind region, having a slight increase in depth and rounding out the sharp vertical gradient from Case 1.

The resolution retention of gradient-determined parameters obeys an approximate power-law relationship with the resolution ratio $\Delta x/\eta$ for both reduced resolution cases with baseline viscosity and cases with enhanced viscosity approximating mesoscale model behavior. This power-law relationship has the potential to inform other modeling efforts by providing an approximation of how the accuracy of peak gradient parameter amplitudes deteriorates in under-resolved simulations. Given the good agreement between both fits, the power-law dependence of these parameter amplitudes on resolution is likely generalizable to other GW-FS simulations, though more trials are needed to determine the broader conditions under which this relationship holds.

Chapter 10

Conclusions and Future Work

This dissertation presents a comprehensive overview and analysis of the complex dynamics of high frequency atmospheric gravity wave and fine structure (GW-FS) interactions. The work is motivated by a need to characterize influential GW dynamics in the MLT occurring at temporal and spatial scales that are difficult to quantify with observational data and too small to resolve with mesoscale models. The research is comprised of three focus areas: 1) Quantifying the fundamental dynamics of isolated GW-FS interactions in an idealized environment; 2) Evaluating the behavior of transient GW propagation through an evolving FS background observed in the MLT; and 3) Determining the extent to which the large-scale consequences of GW-FS interactions can be retained under the resolution and dynamical constraints imposed by current mesoscale models. These studies employ state-of-the-art numerical simulations (DNS and LES) and yield an improved fundamental understanding of GW-FS dynamics and their implications to the atmosphere.

10.1 Research Study 1

Research Study 1 produces a number of significant findings on the importance of GW-FS interactions in the MLT. Specific results include the following:

(1) Small-amplitude FS yield a diversity of impacts on GW propagation and instability evolution. GW propagation through FS layers accelerates the tendency for small-scale instabilities contributing to GW dissipation and turbulence. These dynamics

generate a range of complex vortical features that undergo similar, but distinct pathways to turbulence. The associated transports and deposition of energy and momentum generate diverse, lasting impacts on the background flow that depend on the locations and character of induced instabilities.

(2) Stability and shear peak effects superpose to produce distinctive vortical evolutions that determine how GWs and local instabilities impact the background environment. The vortical evolutions, initial instability character, and time evolution of the various flows trace back directly to the individual or combined effects of each FS component. When both stability and shear FS are present, shear characteristics dictate the GW contribution to the induced wind while the stability FS accelerates the progression of the instabilities.

(3) Local stability peaks accelerate instability evolution by increasing baroclinity at small scales. Baroclinic sources/sinks and advection thin and intensify the vortical features where strong horizontal temperature gradients and orthogonal divergent flows are present. Such cases rapidly evolve to smaller, more intense vorticity dynamics in 2D and 3D flows, and drive the generation of turbulence and dissipation at the smallest scales. The significant impacts of these small-scale dynamics, even for the weak FS influences considered, suggest additional benefits of further studies of GW-FS interactions to better characterize GW influences in the MLT.

With sufficient resolution, properly characterized GW-FS dynamics exhibit coherent and predictable dynamics that are based on known physical parameters whose evolutions can be traced to identify the exact source of the dominant characteristics of a given instability evolution. Having a fundamental understanding of the distinct effects of shear and stability FS, whether isolated or superposed, provides a foundation for the diagnosis of more complex features that share these basic constructs. Recent studies have come to emphasize the importance of accounting for transient effects of GWs on the background wind while

propagating in addition to the effects of GW breaking. Though the induced wind ($\Delta\overline{U}$) contributions of GW-FS interactions evolve with time, it is worth noting that the $\Delta\overline{U}$ produced by GW-FS interactions with shear FS matches the orientation of the initial FS. The evolution of the vortical features, which can be understood as an alternate representation of induced wind from the GW, preferentially aligns with the $\Delta\overline{U}$ direction imposed by the initial FS. This is valuable, as it suggests that the larger-scale implications of such layers, even at very small depths and amplitudes, can be estimated with simulations that do not fully resolve the underlying instability dynamics.

10.2 Research Study 2

Current mesoscale models are unable to characterize transient GW dynamics, wave-wave interactions, or correct GW transmission and reflection characteristics at thin, time-evolving evanescent layers and critical levels with current WKB and ray theory implementations. Research Study 2 expands the scope of GW-FS analysis from small, isolated FS to larger, continuous, and continuously varying FS formed by an IGW to evaluate another related class of GW-FS interactions where the dominant dynamical implications are not instabilities formed by the evolution of the FS itself or the induced wind, but rather the effect of the FS on the propagation characteristics of the GW passing through. Research Study 2 yields a number of significant findings on the behavior of transient GW-FS interactions in evolving flows in the MLT. Specific results include the following:

(1) For FS scales larger than the GW, the dominant characteristics of this class of GW-FS dynamics are the time-varying propagation characteristics imposed on the GW by the background stratification. Propagation characteristics cannot be determined from simply identifying the dominant parameters of the inertial GW and the propagating GW; rather, the local time evolution of the IGW determines the degree to which the propagating GW is reflected or transmitted and sets the resulting GW

intrinsic frequency that defines the phase structure at each altitude.

(2) Tunneling through evanescent regions can occur in an evanescent region produced by enhanced background shear in near-constant stratification. Ray theory, the application of WKB theory used in most mesoscale models, incorrectly predicts complete reflection of GWs at evanescent regions where $\omega > N$ and fails to capture the correct transmission behavior.

(3) Intermittent variations in evanescent and tunneling characteristics are a substantial source of transient variability for GW coupling dynamics in the MLT. These findings confirm the results of Cao et al. (2016) and make a strong case for the need to better understand the environments in which GWs can tunnel through evanescent regions. Such dynamics have valuable implications for the role of GW-FS interactions to coupling relationships between the mesosphere and lower thermosphere.

(4) Simulations of GW-FS interactions in the MLT are a valuable tool for resolving observational discrepancies that arise between instruments with different sampling characteristics. While the AMTM instability observations at 22 to 23 UT were initially diagnosed as GW-induced and thought to indicate a lack of GW activity at this altitude, both simulations and lidar observations indicate that the GW presence is continuous through when the GW signature is visible in the AMTM again at later times. They can similarly identify environments in which the assumptions of Ray Theory cannot produce the behavior of GW transmission through evanescent regions generated by different combinations of wind and stability profiles for an impinging GW.

As numerous studies have shown, the most productive way to expand our understanding of possible dynamical sources of transient GW variability is to examine case studies that deviate from our conventional understanding of the behaviors expected for a given environ-

ment. Research Study 2 illustrates the challenges and benefits posed by this line of inquiry, where it can be difficult to get guidance on new GW dynamics from disagreeing observations. The success of this analysis in both diagnosing the source of the intermittent GW propagation in the AMTM and resolving the observational discrepancies between the AMTM and the lidar makes a strong case for future studies employing a synergistic combination of simulations and observations to expand the parameter space of known GW dynamics.

10.3 Research Study 3

With a significant component of GW-FS influences at large scales accounted for by time evolution of GW momentum flux-induced mean wind, and with a significant potential for transient variability in GW coupling dynamics in the MLT, it is imperative that future mesoscale modeling efforts account for the time evolution of GW-FS interactions and flow conditions. Research Study 3 confirms the additional need to properly resolve GW-FS interactions in order to characterize their scale-dependent and time-dependent phenomena. Significant findings include the following:

(1) GW-induced FS evolution and instability characteristics break down and lose physicality when the FS dynamics are under-resolved. Energy-conserving schemes produce numerical oscillations that deteriorate the dominant vortical structures, while schemes using artificial dissipation smooth out instability structures and delay the onset of turbulence.

(2) GW-determined perturbation parameters and their associated fluxes exhibit resolution and Re-dependent distinctions prior to turbulence when the GW is coherent, but their final amplitudes do not vary significantly when resolution is reduced. So long as the minimum grid spacing roughly captures the depth of the initial FS and the phase structure of the GW, Coherent flux amplitudes and their associated induced winds will be retained by an under-resolved simulation.

(3) Gradient-defined parameters which are critical to assessing GW-FS interactions have peak amplitude dependence on resolution ratio and time dependence on Re. Amplitude retention for under-resolved simulations decays with a power-law dependence on the resolution ratio for both energy-conserving schemes and schemes which include artificial dissipation.

While the breakdown of GW-FS interactions at mesoscale model resolutions is known, the precise dynamical implications that contribute to their deterioration are now better understood. With observational guidance identifying the relevant dissipative scales in a given environment, the results of Research Study 3 provide a rough approximation of how well model parameter amplitudes are reproduced at a given resolution and enable a better understanding of the Re-imposed time delays on instability evolution. If mesoscale model resolutions could be increased to Δx on the order of FS depths, and if models could account for the effects of transient GW propagation on induced winds, final parameter amplitudes would be mostly reproduced. However, the instability and turbulence characteristics associated with these parameters would still be misdiagnosed because the Re reductions imposed by artificial dissipation alter the time evolution of the flow. Having a better understanding of these modeling limitations is essential to improving GW-FS characterization throughout the atmosphere.

10.4 Suggestions for Future Work

Studies described in this dissertation identify several valuable future studies to build on the findings presented in this dissertation and extend their applicability.

10.4.1 Research Focus 1 Additional Studies

With the baseline characteristics of GW-FS interactions defined for a single GW and FS environment, additional simulation studies can investigate how these effects are compounded

with the inclusion of more FS features and GW packets covering a range of scales, frequencies, and amplitudes representative of the atmosphere. Observed FS in the MLT often have larger amplitudes and depths than those simulated in Research Study 1, so a study of the effects of 1) the ratio of GW λ_z to FS depth and 2) the ratio of GW amplitude to FS amplitude would provide insight into how GW-FS dynamics play out in a broader range of environments that can extend the applicability of this study. Studies of GW propagation through multiple FS layers should also be investigated, and the structure of the background post-GW passage should also be examined in more detail.

10.4.2 Research Focus 2 Additional Studies

A broad range of observations exist showing complex, time-dependent GW evolutions in the MLT and elsewhere. As observational capabilities continue to increase in resolution and observe more remote environments, more observations will surface with the capacity to expand the current understanding of what causes variability in model predictions and discrepancies in instrument observations. Numerical studies of these observations, such as those acquired in the recent PMC-TURBO campaign, are essential to building a foundation of pathological dynamical behaviors currently on the periphery of what can be observed or modeled.

10.4.3 Research Focus 3 Additional Studies

While resolution is a basic constraint of every modeling effort, ascertaining the governing dimensionless parameter relationships of a flow environment is vital to the ability to generalize the findings of one case study to other environments. An expanded analysis of parameter dependencies on local Re, Ri, and Pr would ultimately yield physical relationships that benefit all forms of atmospheric modeling and contribute to the larger scientific community. The use of a more robust numerical dissipation scheme in place of enhanced viscosity could also benefit mesoscale model comparisons.

10.4.4 GW-FS Interactions in the Lower Atmosphere

Given the ubiquity of fine layered structures throughout the atmosphere, one can hypothesize that the dynamics of GW interactions with fine structures elsewhere in the atmosphere that are easier to observe, such as the troposphere, are governed by many of the same dominant interaction mechanisms as those in the MLT characterized in the aforementioned studies, where complex dynamics are easier to model but observations are more sparse. Having determined the morphology of the most influential dynamics of GW-FS interactions in the MLT, and having established the resolution requirements needed to characterize these dynamics relative to the expected spatial scales governing these interactions, one can then use this knowledge to approximate the influence of these phenomena at lower altitudes in support of field research programs sampling turbulence in the highly stratified environment above the planetary boundary layer.

The primary research objective would be to see if dominant dynamics found in Chapters 7-9, play an influential role in the lower troposphere. This will be accomplished by providing modeling support for the data collected in the upcoming Instabilities, Dynamics, and Energetics accompanying Atmospheric Layering (IDEAL) field campaign, which took place in October 2016 in Dugway, Utah. IDEAL explored the morphology of sheet and layer structures and energetics in the free troposphere, using airborne and ground-based observation platforms with the support of high resolution DNS. Observations were obtained with a DataHawk UAV with high resolution in-situ sensors, collecting data in tandem with a tethered balloon system, two ground-based wind profilers, and numerous soundings, to measure turbulent fine scale structures at and above the convective boundary layer. Resulting datasets provide ample opportunity to assimilate the approximate background conditions from measurements into a numerical model and discern what if any of the dominant mechanisms of the MLT are at play.

10.5 Summary

A case has been made for the inclusion of GW-FS interactions in mesoscale models seeking accurate characterization of short and long term evolution of the dominant wind and temperature characteristics in the MLT. GW-FS interactions follow predictable evolutions, with large-scale feature generation that traces to the vortical characteristics imposed by the dominant FS components of the flow. GW propagation characteristics imposed by FS evolving in space and time are a prominent source of transient variability in MLT coupling dynamics. With knowledge of the resolution constraints of a given environment, the accuracy of GW-FS characterization can be evaluated to determine the extent to which GW-FS dynamics account for variability in under-resolved models, providing a pathway to long-term forecasting improvements with societal benefits.

Bibliography

Alexander, M. J. and Barnet, C. (2007). Using Satellite Observations to Constrain Parameterizations of Gravity Wave Effects for Global Models. Journal of the Atmospheric Sciences, 64(5):1652–1665.

Andreassen, O., Hvidsten, P. O., Fritts, D. C., and Arendt, S. (1998). Vorticity dynamics in a breaking internal gravity wave. Part 1. Initial instability evolution. Journal of Fluid Mechanics, 367:27–46.

Andreassen, O., Wasberg, C., Fritts, D. C., and Isler, J. R. (1994). Gravity wave breaking in two and three dimensions 1 . Model description and comparison of two-dimensional evolutions. Journal of Geophysical Research, 99:8095–8108.

Baker, D. J. and Stair, A. T. (1988). Rocket measurements of the altitude distributions of the hydroxyl airglow. Physica Scripta, 37(4):611–622.

Balsley, B. B. and Garello, R. (1985). The kinetic energy density in the troposphere, stratosphere and mesosphere: A preliminary study using the Poker Flat MST radar in Alaska. Radio Science, 20(6):1355–1361.

Baumgarten, G. and Fritts, D. C. (2014). Quantifying Kelvin-Helmholtz instability dynamics observed in noctilucent clouds: 1. Methods and observations. Journal of Geophysical Research: Atmospheres, 119(15):9324–9337.

Benze, S. (2012). Analysis of Satellite-Based Polar Mesospheric Cloud Observations. PhD thesis, University of Colorado Boulder.

Bölöni, G., Achatz, U., Ribstein, B., Muraschko, J., and Sgoff, C. (2016). The relative importance of transient wave-mean-flow interactions and turbulent wave breaking in atmospheric gravity-wave parameterizations. In Proc. VIIIth Int. Symp. on Stratified Flows, San Diego, USA, pages 1–7.

Booker, J. R. and Bretherton, F. P. (1967). The critical layer for internal gravity waves in a shear flow. Journal of Fluid Mechanics, 27(03):513.

Bossert, K., Fritts, D. C., Pautet, P.-d., Taylor, M. J., Williams, B. P., and Pendelton, W. R. (2014). Investigation of a mesospheric gravity wave ducting event using coordinated sodium lidar and Mesospheric Temperature Mapper measurements at ALOMAR, Norway (69N). Journal of Geophysical Research: Atmospheres, 119(16):9765–9778.

Bossert, K., Fritts, D. C., Pautet, P.-d., Williams, B. P., Taylor, M. J., Kai, B., Dörnbrack, A., Reid, I. M., Murphy, D. J., Spargo, A. J., and Mackinnon, A. D. (2015). Momentum flux estimates accompanying multiscale gracity waves over Mount Cook, New Zealand, on 13 July 2014 during the DEEPWAVE campaign. Journal of Geophysical Research: Atmospheres, (120):9323–9337.

Bossert, K., Fritts, D. C., Yuan, T., Taylor, M. J., and Williams, B. P. (2016). Small-Scale Gravity Wave Propagation and Instability Dynamics in the Presence of Tides.

Bretherton, F. P. (1969). Waves and Turbulence in Stably Stratified Fluids. Radio Science, 4(12):1279–1287.

Broutman, D., Macaskill, C., McIntyre, M. E., and Rottman, J. W. (1997). On Doppler-spreading models of internal waves. Geophysical Research Letters, 24(22):2813–2816.

Broutman, D., Rottman, J. W., and Eckermann, S. D. (2004). Ray Methods for Internal Waves in the Atmosphere and Ocean. Annual Review of Fluid Mechanics, 36(1):233–253.

Brown, G. L., Bush, A. B., and Sutherland, B. R. (2008a). Beyond ray tracing for internal waves. I. Small-amplitude anelastic waves. Physics of Fluids, 20(10).

Brown, G. L., Bush, A. B., and Sutherland, B. R. (2008b). Beyond ray tracing for internal waves. II. Finite-amplitude effects. Physics of Fluids, 20(10).

Brown, G. L. and Roshko, A. (1974). On density effects and large structure in turbulent mixing layers. Journal of Fluid Mechanics, 64(04):775–816.

Cao, B., Heale, C. J., Guo, Y., Liu, A. Z., and Snively, J. B. (2016). Observation and modeling of gravity wave propagation through reflection and critical layers above Andes Lidar Observatory at Cerro Pachón, Chile. Journal of Geophysical Research: Atmospheres, 121(21):12,737–12,750.

Chanin, M.-l. and Hauchecorne, A. (1981). Lidar Observation of Gravity and Tidal Waves in the Stratosphere and Mesosphere. Journal of Geophysical Research, 86:9715–9721.

Chen, C., Chu, X., McDonald, A. J., Vadas, S. L., Yu, Z., Fong, W., and Lu, X. (2013). Inertia-gravity waves in Antarctica: A case study using simultaneous lidar and radar measurements at McMurdo/Scott Base (77.8${}ˆ{o}$S, 166.7${}ˆ{o}$E). Journal of Geophysical Research Atmospheres, 118(7):2794–2808.

Chu, X., Huang, W., and Smith, J. A. (2012). Lidar Measurements of Winds in the Upper Atmosphere Earth's Atmosphere and Space. In LWG Meeting, Boulder, CO.

Dong, W., Rahmani, M., and Lawrence, G. (2016). The effect of vortex pairing and Prandtl number on mixing in moderate Reynolds number stratified flows. In Proc. VIIIth Int. Symp. on Stratified Flows, San Diego, USA.

Dörnbrack, A., Gisinger, S., and Kaifler, B. (2017). On the Interpretation of Gravity Wave Measurements by Ground-Based Lidars. Atmosphere, 8(3):49.

Dosser, H. V. and Sutherland, B. R. (2011a). Anelastic Internal Wave Packet Evolution and Stability. Journal of the Atmospheric Sciences, 68(12):2844–2859.

Dosser, H. V. and Sutherland, B. R. (2011b). Weakly nonlinear non-Boussinesq internal gravity wavepackets. Physica D: Nonlinear Phenomena, 240(3):346–356.

Felten, F. N. and Lund, T. S. (2006). Kinetic energy conservation issues associated with the collocated mesh scheme for incompressible flow. Journal of Computational Physics, 215(2):465–484.

Fritts, D. C. and Alexander, M. J. (2003). Gravity Wave Dynamics and Effects in the Middle Atmosphere. Reviews of Geophysics, 41(1):1–64.

Fritts, D. C., Arendt, S., and Andreassen, O. (1998). Vorticity dynamics in a breaking internal gravity wave. Part 2. Vortex interactions and transition to turbulence. Journal of Fluid Mechanics, 367:47–65.

Fritts, D. C., Baumgarten, G., Wan, K., Werne, J., and Lund, T. S. (2014a). Quantifying Kelvin-Helmholtz instability dynamics observed in noctilucent clouds: 2. Modeling and interpretation of observations. Journal of Geophysical Research: Atmospheres, 119(15):9359–9375.

Fritts, D. C. and Chou, H.-G. (1987). An Investigation of the Vertical Wavenumber and Frequency Spectra of Gravity Wave Motions in the Lower Stratosphere.

Fritts, D. C. and Dunkerton, T. J. (1984). A Quasi-Linear Study of Gravity-Wave Saturation and Self-Acceleration.

Fritts, D. C., Isler, J. R., and Andreassen, O. (1994). Gravity wave breaking in two and three dimensions 2. Three-dimensional evolution and instability structure. Journal of Geophysical Research, 99:8109–8123.

Fritts, D. C., Laughman, B., Lund, T. S., and Snively, J. B. (2015). Self-acceleration and instability of gravity wave packets: 1. Effects of temporal localization. Journal of Geophysical Research: Atmospheres, (2):1–21.

Fritts, D. C., Laughman, B., Wang, L., Lund, T. S., and Collins, R. L. (2018a). Gravity Wave Dynamics in a Mesospheric Inversion Layer: 1. Reflection, Trapping, and Instability Dynamics. Journal of Geophysical Research: Atmospheres, 123(2):626–648.

Fritts, D. C., Pautet, P.-d., Bossert, K., Taylor, M. J., Williams, B. P., Iimura, H., Yuan, T., Mitchell, N. J., and Stober, G. (2014b). Quantifying gravity wave momentum fluxes with Mesosphere Temperature Mappers and correlative instrumentation. Journal of Geophysical Research: Atmospheres, pages 13583–13603.

Fritts, D. C., Smith, R. B., Taylor, M. J., Doyle, J. D., Eckermann, S. D., Dörnbrack, A., Rapp, M., Williams, B. P., Pautet, P.-d., Bossert, K., Criddle, N. R., Reynolds, C. A., Reinecke, P. A., Uddstrom, M., Revell, M. J., Turner, R., Kaifler, B., Wagner, J. S., Mixa, T., Kruse, C. G., Nugent, A. D., Watson, C. D., Gisinger, S., Smith, S. M., Lieberman, R. S., Laughman, B., Moore, J. J., Brown, W. O., Haggerty, J. A., Rockwell, A., Stossmeister, G. J., Williams, S. F., Hernandez, G., Murphy, D. J., Klekociuk, A. R., Reid, I. M., and Ma, J. (2016). The deep propagating gravity wave experiment (deepwave): An airborne and ground-based exploration of gravity wave propagation and effects from their sources throughout the lower and middle atmosphere. Bulletin of the American Meteorological Society, 97(3):425–453.

Fritts, D. C., Wan, K., Werne, J., Lund, T. S., and Hecht, J. H. (2014c). Modeling the implications of Kelvin-Helmholtz instability dynamics for airglow observations. Journal of Geophysical Research: Atmospheres, (119):8858–8871.

Fritts, D. C., Wang, L., Baumgarten, G., Miller, A. D., Geller, M. A., Jones, G., Limon, M., Chapman, D., Didier, J., Kjellstrand, C. B., Araujo, D., Hillbrand, S., Korotkov, A., Tucker, G., and Vinokurov, J. (2017). High-Resolution Observations and Modeling of Turbulence Sources, Structures, and Intensities in the Upper Mesosphere. Journal of Atmospheric and Solar-Terrestrial Physics, (November 2016):1–22.

Fritts, D. C., Wang, L., Laughman, B., Lund, T. S., and Collins, R. L. (2018b). Gravity Wave Dynamics in a Mesospheric Inversion Layer: 2. Instabilities, Turbulence, Fluxes, and Mixing. Journal of Geophysical Research: Atmospheres, 123(2):649–670.

Fritts, D. C., Wang, L., and Werne, J. (2009a). Gravity wave-fine structure interactions: A reservoir of small-scale and large-scale turbulence energy. Geophysical Research Letters, 36(19):6–11.

Fritts, D. C., Wang, L., Werne, J., Lund, T. S., and Wan, K. (2009b). Gravity Wave Instability Dynamics at High Reynolds Numbers. Part I: Wave Field Evolution at Large Amplitudes and High Frequencies. Journal of the Atmospheric Sciences, 66(5):1126–1148.

Fritts, D. C., Wang, L., Werne, J., Lund, T. S., and Wan, K. (2009c). Gravity Wave Instability Dynamics at High Reynolds Numbers. Part II: Turbulence Evolution, Structure, and Anisotropy. Journal of the Atmospheric Sciences, 66(5):1149–1171.

Geller, M. A., Alexander, M. J., Love, P. T., Bacmeister, J., Ern, M., Hertzog, A., Manzini, E., Preusse, P., Sato, K., Scaife, A. A., and Zhou, T. (2013). A comparison between gravity wave momentum fluxes in observations and climate models. Journal of Climate, 26(17):6383–6405.

Germano, M., Piomelli, U., Moin, P., and Cabot, W. H. (1991). A dynamic subgrid-scale eddy viscosity model. Phys. Fluids A Fluid Dyn., 3(7):1760.

Grimshaw, R. (1977). The Modulation of an Internal Gravity-Wave Packet, and the Resonance with the Mean Motion. Studies in Applied Mathematics, 56(3):241–266.

Harten, A., Engquist, B., Osher, S., and Chakravarthy, S. (1987). Uniformly High Order Accurate Essentially Non-oscillatory Schemes, III. Journal of Computational Physics, 71:231–303.

Heale, C. J. (2014). Long-Range Propagation, Interaction, and Dissipation of Small-Scale Gravity Waves in the MLT. PhD thesis, Embry-Riddle Aeronautical University - Daytona Beach.

Heale, C. J., Bossert, K., Snively, J. B., Fritts, D. C., Pautet, P.-d., and Taylor, M. J. (2017). Numerical modeling of a multiscale gravity wave event and its airglow signatures over Mount Cook, New Zealand, during the DEEPWAVE campaign. Journal of Geophysical Research: Atmospheres, pages 846–860.

Heale, C. J. and Snively, J. B. (2015). Gravity wave propagation through a vertically and horizontally inhomogeneous background wind. Journal of Geophysical Research: Atmospheres, pages 5931–5950.

Hecht, J. H., Fritts, D. C., Wang, L., Gelinas, L. J., Rudy, R. J., Walterscheid, R. L., Taylor, M. J., Pautet, P.-d., Smith, S. M., and Franke, S. J. (2018). Observations of the Breakdown of Mountain Waves Over the Andes Lidar Observatory at Cerro Pachon on 8/9 July 2012. Journal of Geophysical Research: Atmospheres, 123(1):276–299.

Hecht, J. H., Liu, A. Z., Walterscheid, R. L., and Rudy, R. J. (2005). Maui Mesosphere and Lower Thermosphere (Maui MALT) observations of the evolution of Kelvin-Helmholtz billows formed near 86 km altitude. Journal of Geophysical Research D: Atmospheres, 110(9):1–19.

Hecht, J. H., Wan, K., Gelinas, L. J., Fritts, D. C., Walterscheid, R. L., Rudy, R. J., Liu, A. Z., Franke, S. J., Vargas, F. A., Pautet, P.-d., Taylor, M. J., and Swenson, G. R. (2014). The life cycle of instability features measured from the Andes Lidar Observatory over Cerro Pachon on 24 March 2012. Journal of Geophysical Research: Atmospheres, 119(14):8872–8898.

Heisenberg, W. (1948). On the Theory of Statistical and Isotropic Turbulence. Proceedings of the Royal Society A: Mathematical, Physical and Engineering Sciences, 195(1042):402–406.

Henyey, F. S. and Pomphrey, N. (1983). Eikonal description of internal wave interactions: A non-diffusive picture of "induced diffusion". Dynamics of Atmospheres and Oceans, 7(4):189–219.

Henyey, F. S., Wright, J., and Flatte, S. M. (1986). Energy and Action Flow Through an Internal Wave Field: an Eikonal Approach. 91:8487–8495.

Hill, R. J. and Clifford, S. F. (1978). Modified spectrum of atmospheric temperature fluctuations and its application to optical propagation. Journal of the Optical Society of America, 68(7):892.

Hocking, W. K. (1985). Measurement of turbulent energy dissipation rates in the middle atmosphere by radar techniques: A review. Radio Science, 20(6):1403–1422.

Hodges, R. R. (1967). Generation of turbulence in the upper atmosphere by internal gravity waves. Journal of Geophysical Research, 72(13):3455–3458.

Jiang, G.-S. and Shu, C.-W. (1996). Efficient Implementation of Weighted ENO Schemes. Journal of Computational Physics, 228(126):202–228.

Kaifler, B., Kaifler, N., Ehard, B., Dörnbrack, A., Rapp, M., and Fritts, D. C. (2015). Influences of source conditions on mountain wave penetration into the stratosphere and mesosphere. Geophysical Research Letters, 42(21):9488–9494.

Klostermeyer, J. (1991). Two- and three-dimensional parametric instabilities in finite-amplitude internal gravity waves. Geophysical & Astrophysical Fluid Dynamics, 61(1-4):1–25.

Koshyk, J. N., Boville, B. a., Hamilton, K., Manzini, E., and Shibata, K. (1999). Kinetic energy spectrum of horizontal motions in middle-atmosphere models. Journal of Geophysical Research, 104(D22):27177.

Lawrence, D. A. and Balsley, B. B. (2013). High-resolution atmospheric sensing of multiple atmospheric variables using the DataHawk small airborne measurement system. Journal of Atmospheric and Oceanic Technology, 30(10):2352–2366.

Lehmacher, G. A., Guo, L., Kudeki, E., Reyes, P. M., Akgiray, A., and Chau, J. L. (2007). High-resolution observations of mesospheric layers with the Jicamarca VHF radar. Advances in Space Research, 40(6):734–743.

Lelong, M.-P. and Dunkerton, T. J. (1998a). Inertia-Gravity Wave Breaking in Three Dimensions. Part I: Convectively Stable Waves. Journal of the Atmospheric Sciences, 55(1997):2473–2488.

Lelong, M.-P. and Dunkerton, T. J. (1998b). Inertia–Gravity Wave Breaking in Three Dimensions. Part II: Convectively Unstable Waves. Journal of the Atmospheric Sciences, 55(15):2489–2501.

Lighthill, M. J. (1978). Waves in Fluids. Cambridge Mathematical Library. Cambridge University Press.

Lindzen, R. S. (1981). Turbulence and Stress Owing to Gravity Wave and Tidal Breakdown. Journal of Geophysical Research, 86(C10):9707–9714.

Lipps, F. B. and Hemler, R. S. (1982). A Scale Analysis of Deep Moist Convection and Some Related Numerical Calculations.

Lipps, F. B. and Hemler, R. S. (1990). On the anelastic approximation for deep convection.

Liu, H. L. (2016). Variability and predictability of the space environment as related to lower atmosphere forcing. Space Weather, 14(9):634–658.

Liu, H. L., Mcinerney, J. M., Santos, S., Lauritzen, P. H., Taylor, M. a., and Pedatella, N. M. (2014). Gravity waves simulated by high-resolution Whole. Journal of Geophysical Research: Atmospheres, 41:9106–9112.

Lund, T. S. and Fritts, D. C. (2012). Numerical simulation of gravity wave breaking in the lower thermosphere. Journal of Geophysical Research: Atmospheres, 117(21):1–18.

Makhlouf, U. B., Picard, R. H., and Winick, J. R. (1995). Photochemical-dynamical modeling of the measured response of airglow to gravity waves: 1. Basic model for OH airglow. Journal of Geophysical Research, 100(D6):11289.

Miyoshi, Y., Fujiwara, H., Jin, H., and Shinagawa, H. (2014). A global view of gravity waves in the thermosphere simulated by a general circulation model. Journal of Geophysical Research: Space Physics, 119(7):5807–5820.

Moin, P. and Mahesh, K. (1998). DIRECT NUMERICAL SIMULATION: A Tool in Turbulence Research. Annual Review of Fluid Mechanics, 30(1):539–578.

Nappo, C. J. (2012). Ch 10. Gravity Wave Analyses. In An Introduction to Atmospheric Gravity Waves, volume 102, pages 279–307.

Nault, J. T. and Sutherland, B. R. (2007). Internal wave transmission in nonuniform flows. Physics of Fluids, 19(1).

Ngan, K. and Eperon, G. E. (2012). Middle atmosphere predictability in a numerical weather prediction model: Revisiting the inverse error cascade. Quarterly Journal of the Royal Meteorological Society, 138(666):1366–1378.

Patnaik, P. C., Sherman, F. S., and Corcos, G. M. (1976). A numerical simulation of Kelvin-Helmholtz waves of finite amplitude. Journal of Fluid Mechanics, 73(2):215–240.

Pautet, P.-d., Taylor, M. J., Pendelton, W. R., Zhao, Y., Yuan, T., Esplin, R., and McLain, D. (2014). Advanced mesospheric temperature mapper for high-latitude airglow studies. Applied Optics, 53(26):5934–5943.

Pedatella, N. M., Fuller-Rowell, T., Wang, H., Jin, H., Miyoshi, Y., Fujiwara, H., Shinagawa, H., Liu, H. L., Sassi, F., Schmidt, H., Matthias, V., and Goncharenko, L. (2014). The Neutral dynamics during the 2009 sudden stratosphere warming simulated by different whole atmosphere models. Journal of Geophysical Research A: Space Physics, 119(2):1306–1324.

Pope, S. B. (2000). Turbulent Flows. Cambridge University Press, Cambridge.

Rahmani, M., Seymour, B., and Lawrence, G. (2016). Prandtl number effects on mixing in Kelvin-Helmholtz billows. In Proc. VIIIth Int. Symp. on Stratified Flows, San Diego, USA.

Reid, I. M. (1990). Radar observtions of stratified layers in the mesosphere and lower thermosphere (50-100 km). Advances in Space Research, 10(10):7–19.

Sato, K., Kumakura, T., and Takahashi, M. (1999). Gravity Waves Appearing in a High-Resolution GCM Simulation. Journal of the Atmospheric Sciences, 56(8):1005–1018.

Sato, T. and Woodman, R. F. (1982). Fine Altitude Resolution Observations of Stratospheric Turbulent Layers by the Arecibo 430 MHz Radar.

She, C. Y. and Lowe, R. P. (1998). Seasonal temperature variations in the mesopause region at mid-latitude: Comparison of lidar and hydroxyl rotational temperatures using windiiuars oh Height profiles. Journal of Atmospheric and Solar-Terrestrial Physics, 60(16):1573–1583.

She, C. Y., Vance, J. D., Williams, B. P., Krueger, D. A., Moosmüller, H., Gibson-Wilde, D., and Fritts, D. C. (2002). Lidar studies of atmospheric dynamics near polar mesopause. Eos, 83(27):292–293.

Shu, C.-W. and Osher, S. (1988). Efficient Implementation of Essentially Non-oscillatory Shock-Capturing Schemes, II. Journal of Computational Physics, 77(88):439–471.

Siskind, D. E. (2014). Simulations of the winter stratopause and summer mesopause at varying spatial resolutions. Journal of Geophysical Research Atmospheres, 119(2):461–470.

Smith, S. M., Friedman, J., Raizada, S., Tepley, C., Baumgardner, J., and Mendillo, M. (2005). Evidence of mesospheric bore formation from a breaking gravity wave event: Simultaneous imaging and lidar measurements. Journal of Atmospheric and Solar-Terrestrial Physics, 67(4):345–356.

Snively, J. B. (2017). Nonlinear Gravity Wave Forcing as a Source of Acoustic Waves in the Mesosphere, Thermosphere, and Ionosphere. Geophysical Research Letters, 44(23):12,020–12,027.

Snively, J. B. and Pasko, V. P. (2008). Excitation of ducted gravity waves in the lower thermosphere by tropospheric sources. Journal of Geophysical Research: Space Physics, 113(6):1–21.

Snively, J. B., Pasko, V. P., and Taylor, M. J. (2010). OH and OI airglow layer modulation by ducted short-period gravity waves: Effects of trapping altitude. Journal of Geophysical Research: Space Physics, 115(11):1–13.

Sonmor, L. J. and Klaassen, G. P. (1997). Toward a Unified Theory of Gravity Wave Stability. Journal of the Atmospheric Sciences, 54(22):2655–2680.

Sutherland, B. R. (2001). Finite-amplitude internal wave packet dispersion and breaking. J. Fluid Mech., 429:343–380.

Sutherland, B. R. (2006). Weakly nonlinear internal gravity wavepackets. Journal of Fluid Mechanics, 569:249–258.

Sutherland, B. R. and Yewchuk, K. (2004). Internal wave tunnelling. Journal of Fluid Mechanics, 511:125–134.

Tatarski, V. I. (1961). Wave Propagation in a Turbulent Medium. New York.

Thorpe, S. A. (1987). Transitional phenomena and the development of turbulence in stratified fluids: A review. Journal of Geophysical Research: Oceans, 92:5231–5248.

Thurairajah, B., Bailey, S. M., Nielsen, K., Randall, C. E., Lumpe, J. D., Taylor, M. J., and Russell, J. M. (2013). Morphology of polar mesospheric clouds as seen from space. Journal of Atmospheric and Solar-Terrestrial Physics, 104:234–243.

Tsuda, T. (2014). Characteristics of atmospheric gravity waves observed using the MU (Middle and Upper atmosphere) radar and GPS (Global Positioning System) radio occultation. Proceedings of the Japan Academy. Series B, Physical and biological sciences, 90(1):12–27.

Tsuda, T., Nishida, M., Rocken, C., and Ware, R. H. (2000). A Global Morphology of Gravity Wave Activity in the Stratosphere Revealed by the GPS Occultation Data (GPS/MET). Journal of Geophysical Research, 105(D6):7257.

Vanneste, J. (1995). The instability of internal gravity waves to localised disturbances. Annales Geophysicae, 13(2):196–210.

Walterscheid, R. L., Schubert, G., and Brinkman, D. G. (2001). Small-scale gravity waves in the upper mesosphere and lower thermosphere generated by deep tropical convection. Journal of Geophysical Research Atmospheres, 106(D23):31825–31832.

Watanabe, S., Sato, K., Kawatani, Y., and Takahashi, M. (2015). Vertical resolution dependence of gravity wave momentum flux simulated by an atmospheric general circulation model. Geoscientific Model Development, 8(6):1637–1644.

Werne, J. (2016). Instability , Evolution , and Mixing in Stratified Shear Flow as a Function of Richardson Number. In Proc. VIIIth Int. Symp. on Stratified Flows, San Diego, USA, number 1, pages 1–7.

Whiteway, J. A., Duck, T. J., Donovan, D. P., Bird, L. C., Pal, S. R., and Carswell, A. I. (1997). Measurement of gravity wave activity within and around the Arctic stratosphere vortex. Geophys. Res. Lett., 24(11):1387–1390.

Woodman, R. F. and Rastogi, P. K. (1984). Evaluation of effective eddy diffusivity coefficients using radar observations of turbulence in the stratosphere. Geophys. Res. Lett., 211(3):243–246.

Yamashita, C., Chu, X., Liu, H. L., Espy, P. J., Nott, G. J., and Huang, W. (2009). Stratospheric gravity wave characteristics and seasonal variations observed by lidar at the South Pole and Rothera, Antarctica. Journal of Geophysical Research Atmospheres, 114(12):1–11.

Yeh, K. C. and Liu, C. H. (1981). The instability of atmospheric gravity waves through wave-wave interactions. Journal of geophysical research, 86(1):9722–9728.

List of Terms

ALOMAR Arctic Lidar Observatory for Middle Atmosphere Research

AMTM advanced mesospheric temperature mapper

DNS direct numerical simulation

FS fine structure

FWHM full width at half maximum

GW gravity wave

HFGW high frequency gravity wave

IGW inertial gravity wave

KE kinetic energy

KHI Kelvin-Helmholtz instability

LES large eddy simulation

MLT mesosphere and lower thermosphere

NLC noctilucent cloud

PMC polar mesospheric cloud

UT Universal Time

List of Symbols and Notation

c phase speed

c_{gz} vertical group velocity

c_p specific heat

d layer depth in background profile

δ Kronecker delta

f inertial frequency

g gravity

H density scale height

k, l, m streamwise-horizontal, spanwise-horizontal, and vertical wavenumbers

κ thermal conductivity

λ wavelength

μ molecular viscosity

N Brunt-Vaisala frequency

ν kinematic viscosity

ω gravity wave intrinsic frequency

Ω Earth's rotation rate

p pressure

ϕ latitude

Pr Prandtl number

Re Reynolds number

ρ density

Ri Richardson number

t time

T temperature

T_B buoyancy period

θ potential temperature

u, v, w streamwise-horizontal, spanwise-horizontal, and vertical wind components

U background horizontal wind (streamwise)

x, y, z streamwise-horizontal, spanwise-horizontal, and vertical coordinate directions

Appendix A

Chapter 8 Supporting Study

An additional study of the effects of GW amplitude on GW-FS interactions was completed in support of the material presented in Chapter 8. Though the findings do not ultimately contribute to the broader narrative of the dissertation, the write-up is included in this appendix for future reference.

A.1 Wave Amplitude Influences on GW and Background Flow Evolution

Again using the $\overline{U}_z$ and N^2 layers described in Figure 7.1, Case 4 from Chapter 7 is compared with GW amplitude reductions of 75%, 50%, and 25%, where amplitude is defined by Equation 2.21. All other simulation parameters are otherwise identical to the original case.

Reducing GW amplitude delays and diminishes the extent of SA-induced stalled propagation at the top of the packet and compressed λ_z at the bottom, with almost no visible impact on the 25% amplitude case (see Figure A.1). The oscillatory reductions in momentum flux (Figure A.2), wave action, and background wind deceleration (Figure A.3) are similarly reduced in the 75% and 50% amplitude cases to the point of not being present in the 25% amplitude case. This suggests that the phase separation of w' is an amplitude-driven phenomenon, unique to the MLT where the wave-induced mean flow reductions are large enough to promote nonlinearity and energize the subharmonic horizontal wavenumber.

Initial GW breaking and the associated background flow reductions (Figure A.3) are

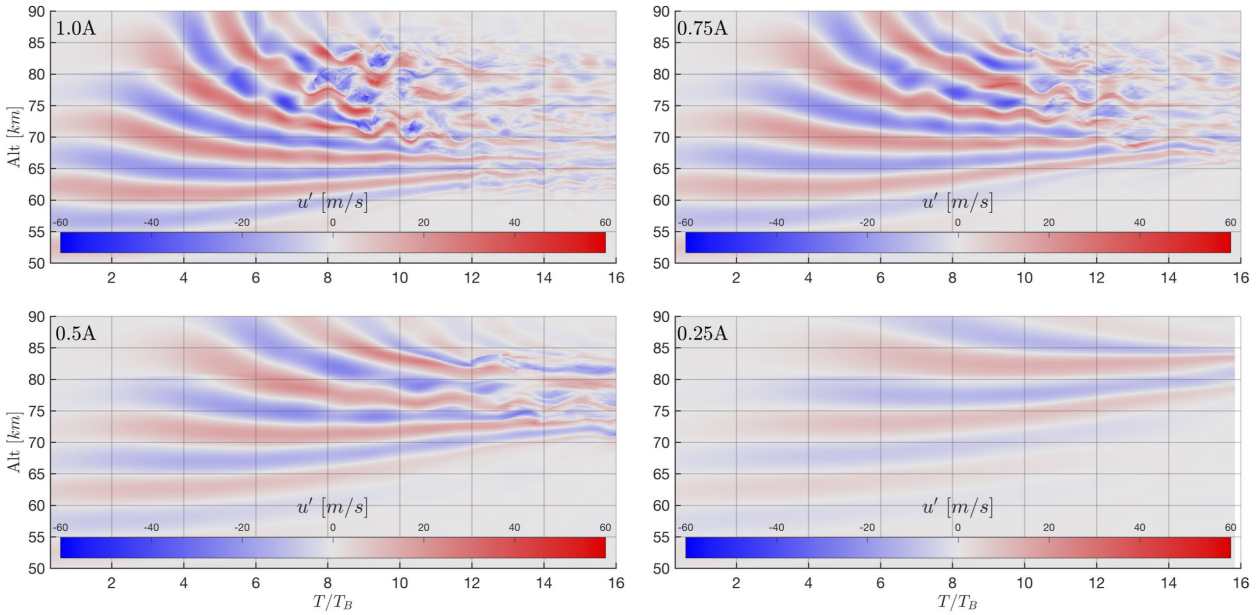

Figure A.1: Time evolution of wind perturbation profiles (u') taken from the center of the domain. Each amplitude reduction pushes the SA effects back in time, and the additional kinking caused by shear layer advection is diminished to the point of not occurring in the 0.25A case.

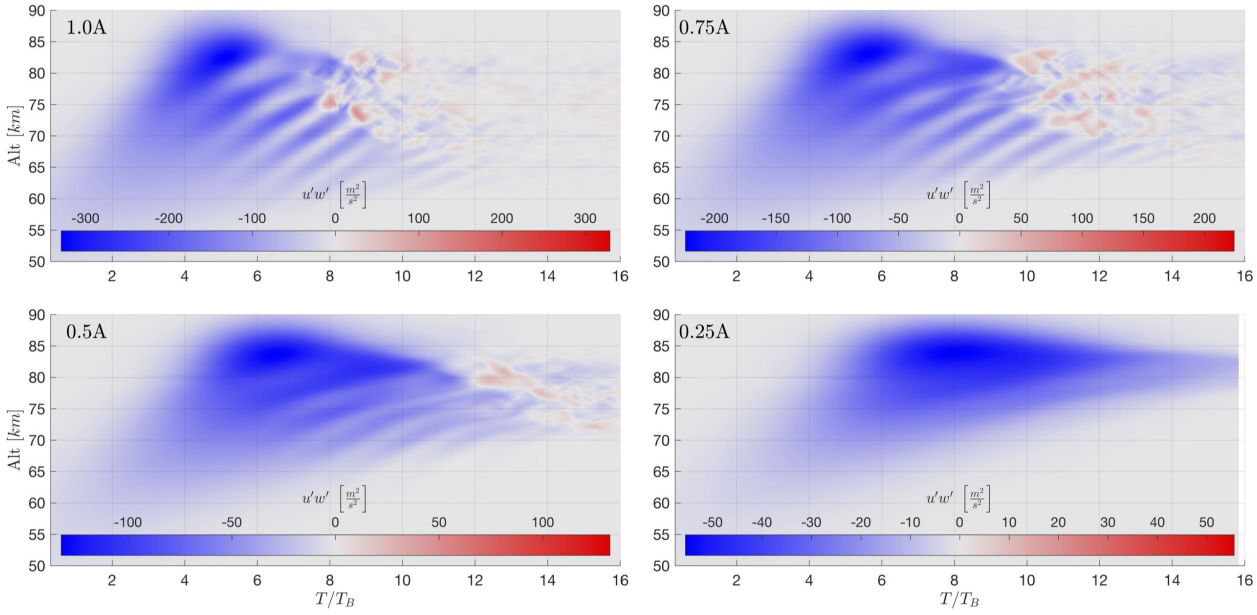

Figure A.2: Time evolution of the momentum flux ($u'w'$), averaged at each altitude. Sign changes clearly show the instability onset time delay with amplitude reduction, as well as reduced out-of-phase sinusoidal variations as the SA effects are reduced to the point of not being present in the 0.25A case. The angle of the sinusoidal variations also indicates a decrease in vertical group velocity with GW amplitude.

delayed by $\sim$1 T_B per 25% amplitude reduction. The downward extent of flow deceleration, shown in the T_∞ state of flow deceleration for each amplitude (Figure A.4), decreases by $\sim 0.5\lambda_z$ per 25% amplitude reduction. The altitudes at which the decelerations occur, while diminished, appear to be the same for all four cases, suggesting that both GW amplitude and layer type play unique roles in determining the final flow state. With reduced flow deceleration at the 85 km breaking altitude, the extent to which the evanescent GW residuals are advected through the domain is diminished in each case, reducing the illusion of residual GW activity a ground based instrument would observe above the layer.

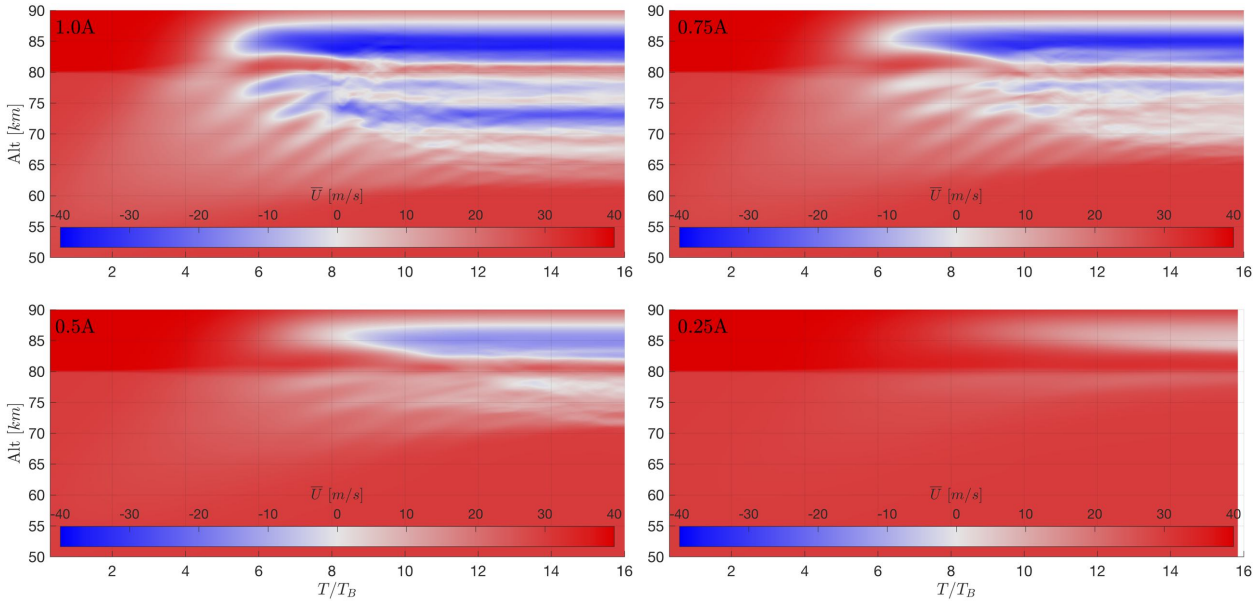

Figure A.3: Evolution of the background wind profiles for $A = [1.0, 0.75, 0.5, 0.25]$. All four simulations share the same discrete layering structures as the original amplitude case, withe the degree of flow deceleration and downward propagation diminished with each reduction in altitude.

The total domain KE density (Figure A.5) shows time delays to the GW reaching its peak energy before breaking, its subsequent falloff, and the onset of turbulence with the rise in 3D KE. The 0.25A case never has sufficient GW amplitude to drive the layer to instability and cause turbulence. In the absence of both turbulence and periodic energy gaps, more of the wave action is able to move upward with time, enabling the most energy transmission through the layer with the lowest amplitude GW (Figure A.6).

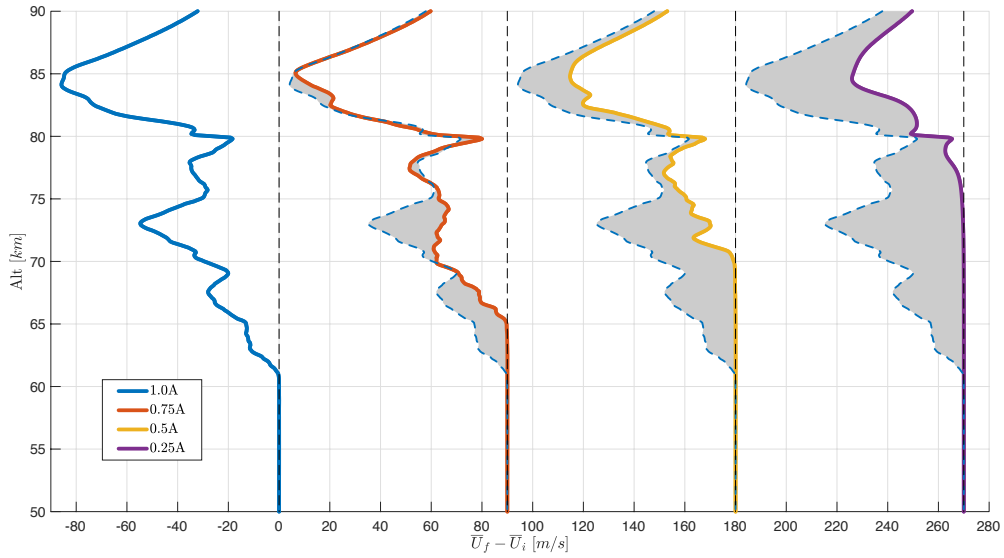

Figure A.4: Background wind deceleration from the initial wind profile $\overline{U}_f - \overline{U}_i$ for $A = [1.0, 0.75, 0.5, 0.25]$. The downward extent of decelerated flow from the initial breaking altitude decreases proportionally with GW amplitude, yet features within each profile's downward extent match those of the 1.0A case at those altitudes. Periodic features also diminish with reduced amplitude.

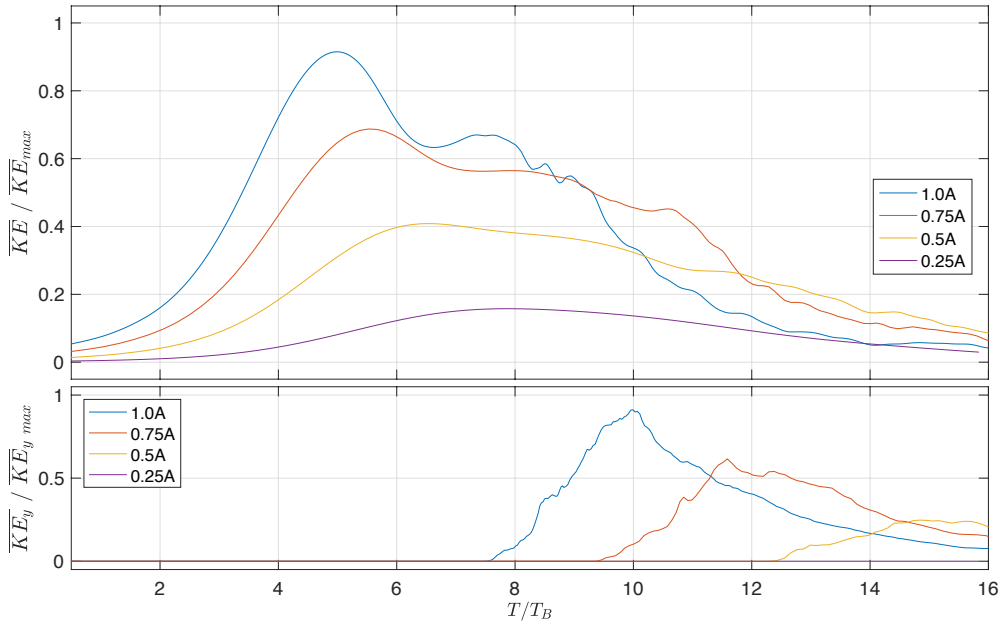

Figure A.5: Domain averaged KE density for all wind components (a) and for the spanwise wind component (b). Decreased GW amplitude results in near-linear time delays for GW propagation, initial energetic maxima at breaking, and instability onset times, all corresponding to the reduced vertical group velocity visible in Figure A.2. The lower energy of the reduced amplitude GWs produces less vigorous turbulence, with the lowest amplitude simulation never developing spanwise KE and reaching a turbulent state.

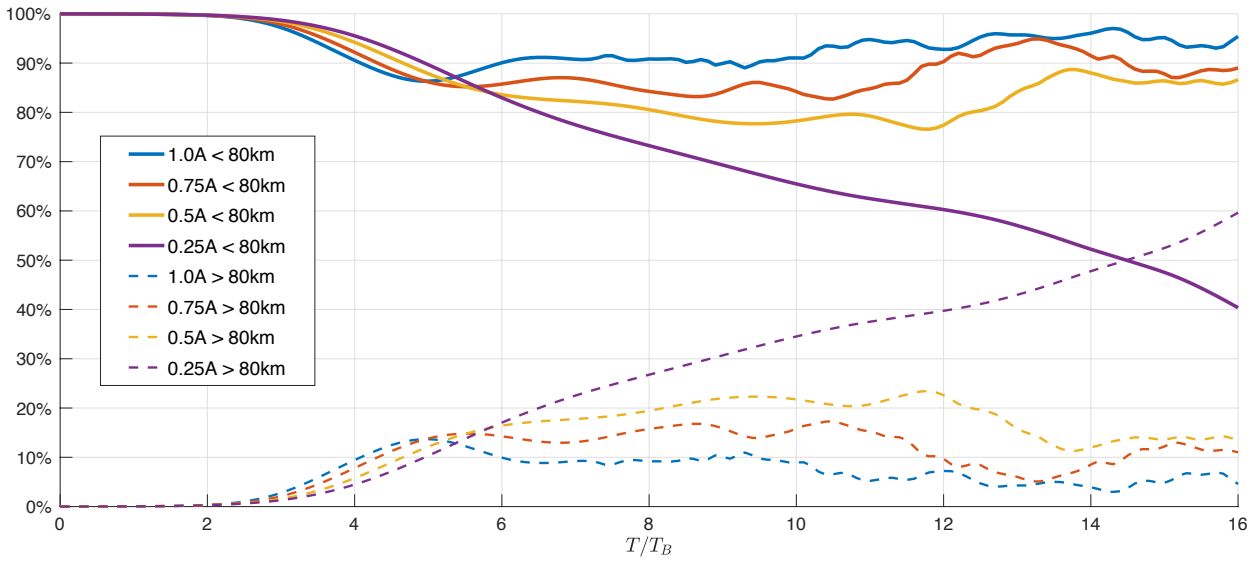

Figure A.6: KE % below 80 km for $A = [1.0, 0.75, 0.5, 0.25]$, with dashed lines indicating the corresponding KE % above 80 km.